

DISSERTATION

FROM COLLOIDAL SOLUTION TO SINGLE PARTICLES: INVESTIGATING ENERGY
FLOW FROM SEMICONDUCTOR NANORCRYSTALS TO MOLECULES

Submitted by

Zach N. Nilsson

Department of Chemistry

In partial fulfillment of the requirements

For the Degree of Doctor of Philosophy

Colorado State University

Fort Collins, Colorado

Summer 2021

Doctoral Committee:

Advisor: Justin B. Sambur

B. George Barisas

Matthew P. Shores

Jesse W. Wilson

Copyright by Zach N. Nilsson 2021

All Rights Reserved

ABSTRACT

FROM COLLOIDAL SOLUTION TO SINGLE PARTICLES: INVESTIGATING ENERGY FLOW FROM SEMICONDUCTOR NANORCRYSTALS TO MOLECULES

The interaction of nanomaterials and molecules is at the heart of many modern processes (catalysis, chemical synthesis, lighting, etc.). The presence of crystallographic defects in the nanomaterials can strongly influence this interaction or open up pathways for unintended interactions. The location of the defect sites plays a large role in determining how a defect sites will interact with the environment around it. Determining the location of defect sites in nanomaterials is a challenge. Transmission electron microscopy (TEM) is the obvious choice to observe atomic scale defects however, in situ TEM measurements are difficult and expensive. Forster resonance energy transfer (FRET) spectroscopy has the power to reveal nanoscale distances from optical data. FRET has been applied to nanomaterial defects in the past but never to reveal the location of defect sites. The following work describes the application of FRET spectroscopy to an ensemble of zinc oxide nanoparticles. It was found that for large nanoparticles (6 nm diameter) FRET could distinguish between surface and interior defect sites. However, the ensemble level approach has limitations. To overcome these, the system was observed on the single particle level using optical microscopy. Single particle studies revealed that energy transfer events appear to be very rare in this system. No conclusive evidence of energy transfer was observed on the single particle level.

ACKNOWLEDGEMENTS

I would like to thank Justin Sambur and all current and past members of the Sambur group for their constant support and assistance. I couldn't have done this without you.

DEDICATION

For my partents. You always believed in me.

3.3.2	Energy Transfer Measurements	29
3.3.3	Stochastic Binding Model Analysis	32
3.3.4	Restricted Geometry Model Analysis	34
3.3.5	Langmuir adsorption fitting	36
3.3.6	Comparison of surface concentration of dye molecules: C_s vs. λ_s	37
3.4	Discussion	38
3.4.1	Comparison of donor-acceptor distances	38
3.4.2	Size independent energy transfer efficiency	41
3.4.3	Limitations of ensemble-level defect-mediated energy transfer studies	41
3.5	Conclusions	43
Chapter 4	Molecular Reaction Imaging of Single-entity Photoelectrodes ²	44
4.1	Introduction	44
4.2	Imaging Photoelectrochemical Reactions via SMFM	46
4.2.1	Reaction intermediate imaging	46
4.2.2	Surface Recombination Imaging	50
4.2.3	Charge Transport Imaging	53
4.3	Imaging Non-Fluorescent Photoelectrochemical Reactions	55
4.3.1	SMFM of non-fluorescent reactions	55
4.3.2	Bright Field Optical Microscopy	57
4.4	Summary and Outlook	63
Chapter 5	Defect Mediated Energy Transfer Microscopy ³	66
5.1	Intro	66
5.2	Experimental Methods	66
5.2.1	Filtering	66
5.2.1.1	Separating single particles from clusters of particles	66
5.2.1.2	Is A555 present inside the ROI?	69
5.3	Data Analysis	72
5.3.1	Background subtraction	72
5.3.2	Trajectory Analysis	73
5.3.3	Ratio Analysis	78
Chapter 6	Summary/Outlook	82
6.1	Summary	82
6.2	Outlook	83
Bibliography	85
Appendix A	Complete TRPL of ZnO NCs	112

²This chapter was published previously as: Nilsson, Z.; Van Erdeyik, M.; Wang, L.; Sambur, J. B. Molecular Reaction Imaging of Single-Entity Photoelectrodes. ACS Energy Lett. 2020, 5 (5), 1474–1486. <https://doi.org/10.1021/acsenerylett.0c00284>.

³In preparation for submission

Appendix B	Division of Work	113
B.1	Chapter 2	113
B.2	Chapter 3	113
B.3	Chapter 4	113
B.4	Chapter 5	113
LIST OF ABBREVIATIONS		114

Chapter 1

Introduction & Background

1.1 Introduction

Interactions of semiconducting nanomaterials and molecules are key to a number of important processes including catalysis,¹⁻⁴ chemical synthesis,^{5,6} and lighting.^{7,8} At the heart of these processes is the movement of energy between the nanomaterials and the molecules around them. Understanding how materials can interact with molecules can help guide the creation of more efficient devices. One major factor that can influence the interaction between a nanomaterials and a molecule is the presence of defect sites⁹⁻¹¹ (crystallographic point defects like vacancies, interstitial atoms, anti-sites, etc.). Defect sites can introduce energy levels inside the bandgap of the material (sometimes called mid-gap states), opening new avenues for interactions otherwise not possible.¹²⁻¹⁴ These mid-gap states can also open new recombination pathways, both radiative and non-radiative.^{15,16} The relative position of the defect sites within the material strongly influences the types of interactions that can be possible.^{17,18} Defect sites on the surface of the material can directly interact with molecules while defects that are buried within the material may promote a different type of reaction. However, determining the location of these defect sites, which often are on the single-atom scale, is difficult. Transmission electron microscopy (TEM) is the obvious choice for observing single-atom-scale defects however, in situ TEM measurements are difficult and expensive. Optical methods would be preferable due to their lower cost and simpler set up.

Förster resonance energy transfer (FRET) spectroscopy can reveal nanoscale distance information in heterogeneous and dynamic systems without having to observe the sample with a microscope. The FRET technique is based on energy transfer between donor and acceptor molecules, where the photo-excited donor transfers energy non-radiatively to a nearby acceptor molecule via a dipole-dipole coupling mechanism.¹⁹⁻²¹ This method is commonly used as a “spectroscopic ruler”²²⁻²⁵ because small changes in donor-acceptor distance (r) cause large changes in fluores-

cence intensities of the donor and acceptor. The large intensity changes occur because the FRET rate scales with r^{-6} .¹⁹⁻²¹ Steady-state and/or time-resolved photoluminescence (TRPL) spectroscopy methods can quantify r , provided that photophysical properties (e.g., spectral overlap of the donor and acceptor, donor fluorescence lifetime, and quantum yield) as well as relative orientation of the donor and acceptor molecules are known. FRET spectroscopy measurements have revealed critical dynamic distance measurements in complex systems such as membrane fusion²⁶ and conformational changes of peptides, DNA, and RNA. See the following section for a more detailed background on FRET.²⁷⁻²⁹

Defect-mediated energy transfer³⁰ has the possibility to provide a non-destructive, non-permanent method for locating defect sites in nanomaterials. In this scheme defect sites within the nanomaterial act as the donors for a FRET-like energy transfer system. Because FRET is the spectroscopic ruler it should be possible to use FRET to determine the locations of defect sites in nanomaterials, provided the defect sites are able to participate in energy transfer. This method has been applied to both colloidal solutions of nanomaterials (see Chapter 3) and single particles (see Chapter 5) in this work.

1.2 Background: Förster Resonance Energy Transfer (FRET)

The first observations of long-range energy transfer were by Cario and Franck in 1922^{31,32} who excited a gaseous mixture of mercury and thallium atoms with light that would only excite the mercury, yet they observed emission from the thallium as well. They also determined that there must be interactions between the atoms occurring at distances larger than the calculated encounter radius, making this the first recorded observation of long-range energy transfer.³³ While T. Förster was not the first person to observe long-range non-radiative energy transfer, he is credited with developing an easy to understand and apply model for describing non-radiative energy transfer between molecules in close proximity. Förster's theory describes the interaction between a donor molecule in the excited state (D^*) and an acceptor molecule in the ground state (A) leading to energy that was stored in the donor molecule transferring to the acceptor molecule. This returns

the donor molecule to the ground state (D) and, simultaneously, the acceptor molecule transitions to the excited state (A^*). This process is shown in Equation (1.1). This is called non-radiative energy transfer because the excited state donor does not emit a photon to excite the ground state acceptor.



Instead, the acceptor gains energy by siphoning energy that was stored in an electric field around the donor. Upon exciting a molecule an oscillating dipole is created. This oscillating dipole creates an electric field which stores energy in the near field (distances less than the wavelength of light that would be emitted).³⁴ This near-field energy can be transferred away from the excited dipole to an acceptor dipole if it is close enough and in the correct relative orientation. This field effect was first observed by Heinrich Hertz in the late 19th century in oscillating electrical circuits and was critical to the understanding of non-radiative energy transfer.^{33,35}

Building on the earlier work of Cario and Franck and the Perrins (first Jean and then Francis, who came very close to a quantitative description of long-range energy transfer in molecules)³³ Förster was the first to put together all the parts needed to fully describe the non-radiative energy transfer process.^{20,21,36} Förster determined that the spectral dispersion present in molecular emission and absorption spectra (i.e. molecules do not produce line spectra) needed to be accounted for. He derived the overlap integral (J , Equation (1.2)) to handle this. The overlap integral describes the probability that transitions in the donor and acceptor will have the same frequency (i.e. be in resonance).³³

$$J = \int_0^{\infty} F_D(\lambda)\epsilon_A(\lambda)\lambda^4 d\lambda \quad (1.2)$$

Where $F_D(\lambda)$ is the normalized emission spectrum of the donor on a nanometer axis, normalized so that the area under the curve is equal to 1. $\epsilon_A(\lambda)$ is the extinction coefficient spectrum for the acceptor with units of $M^{-1}cm^{-1}$.

Once the spectral dispersion of the donor and acceptor had been accounted for Förster determined that the distance dependent rate of energy transfer from a single donor to a single acceptor (k_T) would follow:³⁶

$$k_T(r) = \frac{Q_D \kappa^2}{\tau_D r^6} \left(\frac{9000 \ln(10)}{128 \pi^5 N_A n^4} \right) J \quad (1.3)$$

Where Q_D is the emission quantum yield of the donor with no acceptor molecules present, κ^2 is the orientation factor which accounts for the relative orientation of the donor and acceptor dipoles. For dipoles which have rotational and translational freedom (i.e. freely diffusing molecules) $\kappa^2 = \frac{2}{3}$. τ_D is the lifetime of the donor molecule when no acceptor is present. r is the distance between the donor and acceptor; for all calculations in this work r has units of nanometers. N_A is Avogadro's constant. n is the refractive index of the medium (solvent) and J is the overlap integral from Equation (1.2). This equation indicates that the rate of energy transfer scales with the amount of spectral overlap between the donor and acceptor. Additionally, the rate is very distance dependent, as indicated by the r^{-6} term. It is this distance dependence that gives FRET its usefulness as an analytical tool. Equation (1.3) Also indicates that the rate of energy transfer scales with the orientation factor κ^2 . For all calculations conducted later in this work it was assumed that $\kappa^2 = \frac{2}{3}$. Possible pitfalls of this assumption are discussed in Section §3.4.3.

Equation (1.3) can be rearranged by assuming that $k_T = \tau_D$.³⁶ This assumes that the rate of energy transfer is the same as the rate of intrinsic decay in the donor, meaning that there is a 50% chance for each excitation of the donor to result in energy transfer or intrinsic decay. In this form, Equation (1.4) reports the distance between the donor and acceptor needed to satisfy the $k_T(r) = \tau_D$ assumption. This distance is referred as the Förster distance.

$$R_0^6 = \left(\frac{9000 \ln(10) Q_D \kappa^2}{128 \pi^5 N_A n^4} \right) J \quad (1.4)$$

A slight variation of Equation (1.4) can be found in Section §2.3.1 where it is used to determine the Förster distance for a given donor-acceptor system.

Förster's theories are still being applied to energy transfer systems over 60 years after they were developed. FRET theory has been applied to NC-molecule donor-acceptor systems.³⁷⁻⁴⁴ Chowdhury et al. analyzed the PL decay dynamics of 3.0 nm CdS NCs in the presence of rhodamine 6G acceptors and concluded that the energy transfer efficiency was 43%.⁴⁵ Sadhu et al.⁴⁶ later extended a kinetic model, originally developed by Tachiya,⁴⁷ to model CdS NC donor quenching in the presence of multiple Nile Red acceptor molecules.⁴⁶ The aforementioned studies use the point-dipole approximation, placing the donor dipole at the center of the NC with acceptor molecules randomly oriented in around the NC. This dipole approximation is valid when the molecule is in contact with the NC surface.^{48,49} Additionally, Banin and coworkers have shown that the shape of the nanomaterial donor has a profound impact on how the FRET process proceeds but at the core it is still based on Förster's theories.⁵⁰⁻⁵²

1.3 Zinc oxide as a model system

To use defect-mediated energy transfer as a tool to determine the location of defect sites in nanomaterials, the first step is to select a nanomaterial whose defect sites exhibit a fluorescence signal that is attributable to the localized defect sites. Zinc oxide (ZnO) nanocrystals (NCs) are the ideal material to test the feasibility of defect-mediated energy transfer as an analytical tool due to the high intensity (relative to the band-edge emission), broadband, visible emission associated with point defects.⁵³⁻⁵⁷ Figure 1.1 shows a fluorescence spectrum of ZnO NCs excited at 330 nm. The small peak below 400 nm is emission from band-edge states in the ZnO and the high intensity, broad peak is the emission of defects in the ZnO. The identity of the defect responsible for this emission has been a topic of much debate in the literature. Classically, oxygen vacancies (V_O) have been cited as the source of this emission however, recent computational studies combined with optically-detected electron paramagnetic resonance data have shown that V_O 's may not be the source.^{58,59} An even more recent computational study has shown that isolated dangling bonds from zinc atoms are more likely to be the source of the visible emission.⁵⁴ These dangling bonds are similar to an oxygen vacancy except that the true vacancy state is formed by four zinc dangling

bonds mixing together. An isolated zinc dangling bond is just that, isolated and not able to mix with other zinc orbitals.

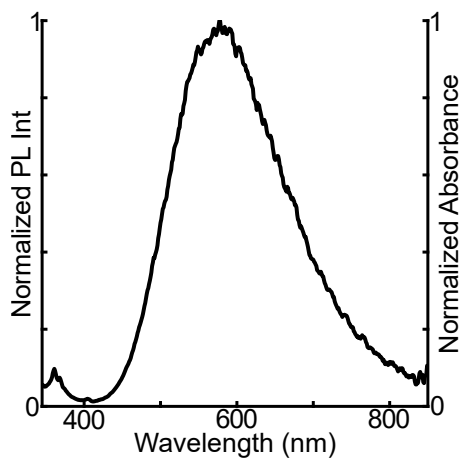


Figure 1.1: Emission spectrum of a solution of 4 nm ZnO NCs excited at 330 nm.

The exact identity of the defect responsible for the visible emission in ZnO is not of prime importance to using defect-mediated energy transfer as an analytical tool to determine the location of the emission source within a nanocrystal. All that matters is that the emission is associated with localized sites in the larger material.

Chapter 2

Experimental Techniques

2.1 Zinc oxide nanocrystal growth and characterization

2.1.1 ZnO synthesis

ZnO nanocrystals (NCs) were synthesized using a base hydrolysis of zinc acetate dihydrate in ethanol following the approach of Wood et al.⁶⁰ In a typical reaction, 1.0 g $\text{Zn}(\text{OAc})_2 \cdot 2\text{H}_2\text{O}$ (Sigma Aldrich) was added to 100 mL of 200 proof ethanol (Pharmco-Aaper) in a 250-mL round bottom flask. The solution was stirred and heated to 68 °C to dissolve the zinc acetate. Then, 2 mL of a 20% methanolic solution of tetramethylammonium hydroxide (TMAOH, Sigma Aldrich) were added to the flask as quickly as possible. We define the TMAOH injection step as $t = 0$. Subsequently, 10 mL aliquots of the growth solution were extracted from the flask at growth times ranging from $t = 2$ to $t = 2400$ min. All aliquots were extracted from the same reaction flask as the reaction proceeded. Each aliquot was injected into 30 mL of hexanes, causing the NCs to precipitate. The mixture was centrifuged to separate the NCs from the unreacted Zn^{2+} and TMAOH. This washing procedure was repeated 5 times with hexanes. The washed NCs were suspended in spectrophotometric grade ethanol and stored at -4 °C when not in use. All reagents were used as received and without further purification.

2.1.2 Nanocrystal Characterization

The optical properties of ZnO NCs were characterized with UV-Vis absorption spectroscopy (HP 8452A Diode Array Spectrophotometer) and steady-state photoluminescence spectroscopy (Edinburgh Instruments FS5). All spectra were measured at room temperature in spectrophotometric grade ethanol in 1 cm quartz cuvettes. The NC diameters were determined using transmission electron microscopy (TEM, JEOL JEM-2100F, 200 keV). The absolute quantum yield (QY) measurement method^{61,62} was used to determine the PL QY of the NC defect emission (Edinburgh

Instruments FS5 spectrophotometer equipped with an integrating sphere). Figure 2.1a-e show distribution of measured diameters for each size of NC along with a representative TEM image of each size. Each diameter distribution is fit to a Gaussian function to determine the average and standard deviation.

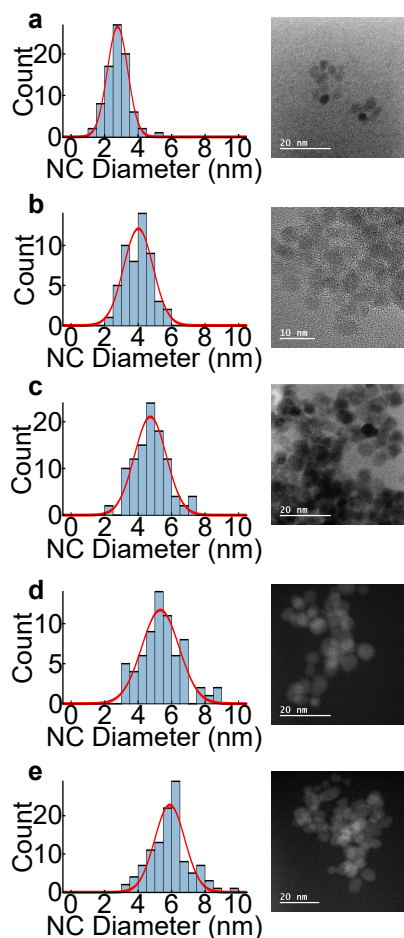


Figure 2.1: NC diameter determination. **a-e)** Histogram of measured diameters fit to a Gaussian distribution and a representative TEM image of each NC size.

Following the approach of Yu et al.,⁶³ we determined the molarity of the ZnO NC samples using TEM and elemental analysis. 3 mL of washed ZnO NCs were dissolved in 5% nitric acid for inductively coupled plasma-atomic emission spectroscopy (ICP-OES) analysis. The ICP-AES analysis quantified the concentration of Zn^{2+} in the sample. To calculate the concentration of NCs in each aliquot, we determined the total number of NCs that could be formed from the total

number of Zn atoms in the solution. We assumed that the ZnO NCs were spheres and calculated the particle volume from the TEM data. We also assumed that the ZnO lattice parameters do not change with NC size.

It was found that high [NC] would lead to particle aggregation and that lower [NC] caused slower aggregation at room temperature. Figure 2.2 shows photographs of ethanolic solutions of ZnO NCs at two concentrations, the higher [NC] solutions show a blue tinge caused by particle aggregates scattering visible light. [NC] = 70 nM was chosen because this concentration reduced NC aggregation and still had measurable photoluminescence. Table 3.1 contains the photophysical properties for all sizes of NCs.



Figure 2.2: Photographs of NC samples at (left) [ZnO] = 1.4 μ M and (right) [ZnO] = 70 nM. The size of the NCs in each vial increases from left to right.

2.2 Ensemble-level energy transfer

All energy transfer measurements were performed with [ZnO NC] = 70 nM unless otherwise noted. This concentration was chosen because particle aggregation was not observed and all samples exhibited measurable defect PL in steady-state and time-resolved PL spectroscopy. In a typical energy transfer experiment, microliter volumes of a stock 7 μ M ethanolic Alexa Fluor[®] 555 carboxylic acid dye (A555; Thermo Fisher) were injected into 3 mL of the ZnO NC sample. Steady-state emission spectra of ZnO-dye mixtures were measured at an excitation wavelength of 330 nm unless otherwise noted. Time-resolved photoluminescence (TRPL) measurements were performed concurrently with the steady-state measurements. The PL lifetime measurements were performed on an Edinburgh Instruments FS5 equipped with a 300 nm pulsed LED (EPLD, 500 kHz). TRPL data was acquired at the defect emission of the ZnO NCs (515 ± 10 nm). This wave-

length range was chosen because there was no contribution from the acceptor emission. TRPL data was deconvoluted from the instrument response function (IRF) following the procedure described in Section §2.2.1. The TRPL fits presented herein have been reconvoluted with the IRF to match the data. Application of this procedure can be found in Chapter 3.

2.2.1 Instrument Response Function Deconvolution

TRPL data was deconvoluted from the IRF using equations (2.1) and (2.2) as model functions in an iterative reconvolution process which minimizes the difference between the data and the model function after the model function has been convoluted with the IRF. By convoluting the model functions with the IRF the true response of the sample can be separated from the instrument response.⁶⁴ Figure 2.3 shows two examples of the IRF deconvolution procedure. The deconvoluted model functions are shown in blue and the reconvoluted fit is shown in red.

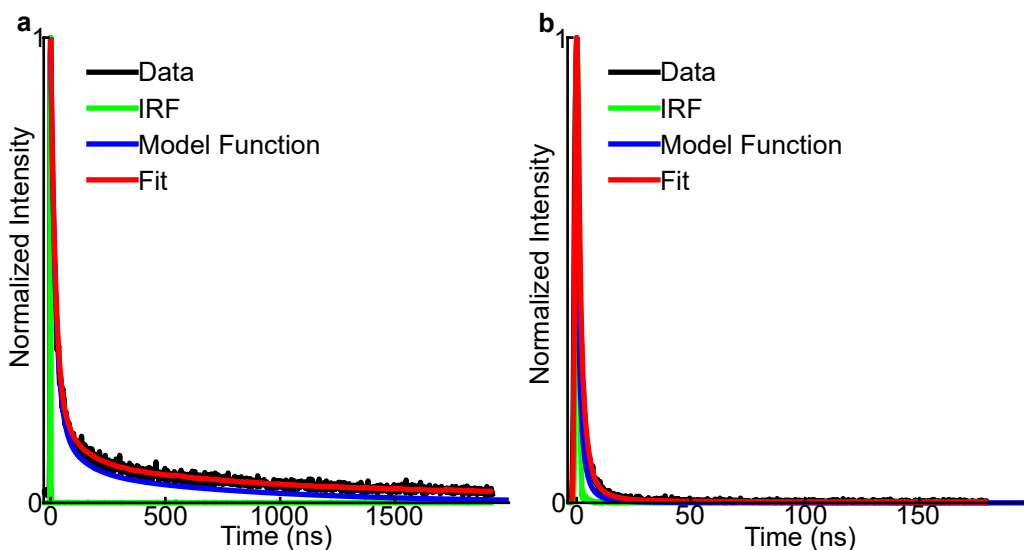


Figure 2.3: IRF deconvolution. **a)** TRPL decay of 4 nm ZnO NCs (black), the IRF (green), the deconvoluted model function (blue) and the reconvoluted fit (red). **b)** The same as (a), but for [A555]:[NC] =1000:1.

2.2.2 Non-fluorescent control

To ensure that the observed quenching of the ZnO defect emission was not due to the binding of the carboxylic acid functionalized acceptor molecules ZnO NCs were exposed to a 100 nM solution of sodium formate (Figure 2.4). Sodium formate was chosen because the carboxylic acid derivative of A555 is sold as an acid salt and it will not become protonated in ethanol. The sodium formate has no effect on the emission of the ZnO NCs, thus the quenching observed when A555 is present cannot be due to the binding of the carboxylic acid to the NCs.

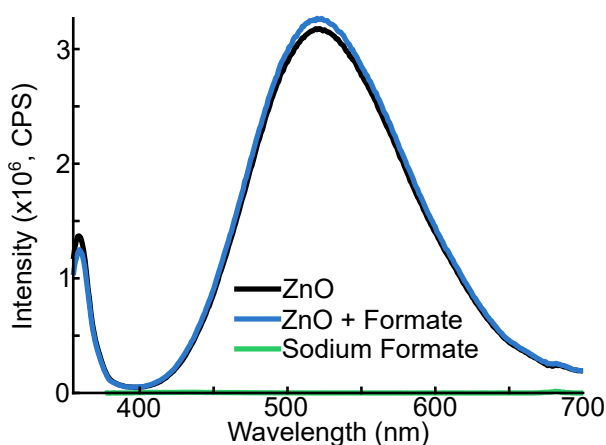


Figure 2.4: PL spectra of ZnO NCs in ethanol (black line), the same ZnO NCs mixed with 100 nM sodium formate (blue line), and 100 nM sodium formate dissolved in ethanol without ZnO NCs (green line).

2.3 Energy Transfer Modeling

TRPL decay data for ZnO NC donors (similar to what is shown in Figure 2.3) were analyzed as a function of NC size and acceptor concentration using two different energy transfer models. The goal was to determine the average donor-acceptor distance, which reflects the distance between the acceptor dyes and the defects responsible for the defect-mediated energy transfer process. Application of the models described below can be found in Chapter 3.

2.3.1 Stochastic Binding Model (SB)

Sadhu et al. developed the stochastic binding model for energy transfer between semiconductor quantum dot donors and molecular dye acceptors⁴⁶ based on earlier work by Tachiya.⁴⁷ Beane et al. applied the stochastic model to study defect-mediated energy transfer between ZnO NC donors and Alexa Fluor[®] dye acceptors.³⁰ The stochastic model assumes: (1) energy transfer between the NC donor and dye acceptor occurs in competition with radiative decay of the NC donor, (2) the distribution of the number of dye molecules attached to one NC follows a Poisson distribution, (3) all attached dye molecules quench the donor emission equally, (4) the intrinsic decay processes of the NCs are unaffected by the attachment of the dye molecules, (5) any acceptor molecule can participate in energy transfer (i.e. both adsorbed or near-surface solution-phase molecules can participate in energy transfer). The model also accounts for the fact that the PL decay of the ZnO NC donors do not follow single exponential kinetics. The TRPL intensity of the ZnO NC donor in the absence of dye acceptors is given by equation (2.1)

$$\frac{I(t)}{I_0} = e^{-k_0 t - \lambda_t [1 - e^{-k_{qt} t}]} \quad (2.1)$$

where I_0 is the intensity of the decay curve at time $t = 0s$, k_0 is the radiative decay rate of photo-excited NCs in the absence of the acceptor molecule, t is the average number of non-radiative trap states per NC and the distribution of traps follow a Poisson distribution, and k_{qt} is the quenching rate due to the presence of the non-radiative traps. The non-radiative trap term is necessary to describe the non-single exponential defect PL decay of the ZnO NCs. These traps do not participate in the energy transfer process.⁴⁶

The TRPL decay curves of the NC donors in the presence of the acceptor are given by equation (2.2)

$$\frac{I(t)}{I_0} = e^{-k_0 t - \lambda_t [1 - e^{-k_{qt} t}] - \lambda_s [1 - e^{-k_q t}]} \quad (2.2)$$

where λ_s is the mean number of dye molecules per NC according to Poisson statistics^{46,47,65} and k_q is the rate of energy transfer to a single dye molecule. Hence, when a NC with n dye molecules is excited, the rate of the excited-state decay for that NC is given by $k_0 + nk_q$, and the total energy transfer rate is nk_q .⁴⁶

Fitting TRPL decay data with Equations (2.1) and (2.2) yields λ_s , λ_t , k_q , k_{qt} , and k_0 , which can be used to calculate the quenching efficiency (ϕ_{EnT}) according to Equation (2.3)⁴⁶

$$\phi_{EnT} = \frac{\sum_{n=0}^{\infty} \sum_{n'=0}^{\infty} \frac{(\frac{\lambda_s^n e^{-\lambda_s}}{n!})(\frac{\lambda_t^{n'} e^{-\lambda_t}}{n'!})}{[1 + \frac{nk_q}{k_0} + \frac{n'k_{qt}}{k_0}]}{\sum_{n'=0}^{\infty} \frac{(\frac{\lambda_t^{n'} e^{-\lambda_t}}{n'!})}{[1 + \frac{n'k_{qt}}{k_0}]}} \quad (2.3)$$

where n and n' are the integer number of attached dye molecules per NC and the integer number of non-radiative traps, respectively. We deconvoluted the IRF from the sample response to fit all TRPL data.

The energy transfer efficiency is related to the number of attached dye molecules per NC and the donor-acceptor distance, r , according to Equation (2.4)^{65,66}

$$\phi_{EnT}(\lambda_s, r) = \sum_{n=0}^{\infty} \frac{\lambda_s^n e^{-\lambda_s}}{n!} \left[\frac{nR_0^6}{r^6 + nR_0^6} \right] \quad (2.4)$$

where R_0 is the Forster radius, or the distance at which the energy transfer efficiency between a single donor-acceptor pair is equal 50%.^{36,65,67} We calculate R_0 according to Equation (2.5)

$$R_0 = \sqrt[6]{\frac{9000 \ln(10) \kappa^2 Q_D J}{128 \pi^5 N_A n^4}} \quad (2.5)$$

where κ is the orientation factor which accounts for the relative orientation of the donor and acceptor dipoles. Q_D is the emission quantum yield of the donor in the absence of the acceptor. J is the overlap integral of the donor emission and acceptor absorbance and N_A is Avogadro's constant. We fit the TRPL-derived energy transfer values using Equation (2.4) to determine the ensemble-average r for each NC diameter and as a function of acceptor concentration.

2.3.2 Restricted Geometry Model (RG)

Sitt et al. developed a restricted geometries model to analyze energy transfer from zero-dimensional (0D) NC and one-dimensional (1D) nanorod donors to molecular acceptors.⁵² For 0D NCs, the model restricts the acceptor molecule locations to a spherical shell at the NC surface, as shown in Figure 2.5. r_1 and r_2 are the minimum and maximum distance in nanometers from the donor to the acceptor molecules, corresponding to the inner and outer radii of the spherical shell. The restricted geometry model assumes that molecules within the shell contribute to energy transfer. The donor dipole is assumed to be a point dipole at the center of the spherical NC. This geometry may not be the case for the emissive defect sites in these ZnONCs where the donor dipole of the defect may not be at the center of the NC. A complete treatment beyond the Förster point dipole approximation could be employed,^{51,68–71} but is not included in the restricted geometries model.

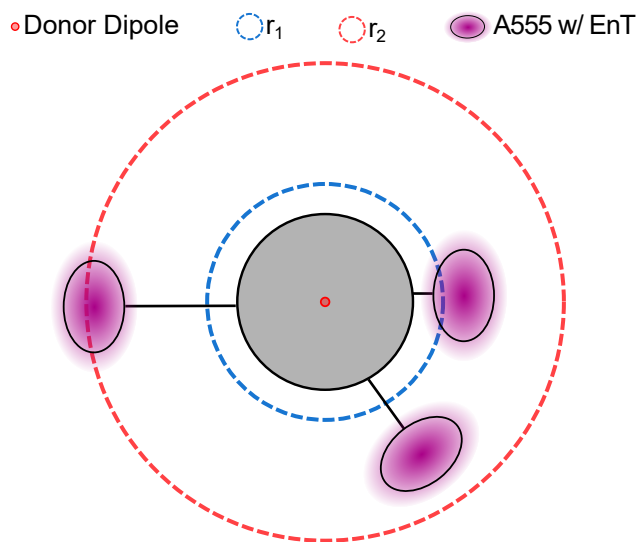


Figure 2.5: Cartoon illustration of energy transfer between NC donors and dye molecules using a restricted geometry model. The donor dipole (red dot) is at the center of the NC (large gray circle). Molecules located within the inner and outer limits of a spherical shell, indicated by circles with radii r_1 and r_2 respectively, can participate in energy transfer (see text for discussion).

The minimum donor-acceptor distance, r_1 , was quantified using Equation (2.6):

$$\phi_{ret}(t) = e^{-\frac{4}{3}\pi C_s \sqrt{t\chi} [\Gamma(1-\frac{3}{S}, t\chi r_1^{-S}) - \Gamma(1-\frac{3}{S}, t\chi r_2^{-S})] + r_2^3 [1 - e^{-t\chi r_2^{-S}}] - r_1^3 [1 - e^{-t\chi r_1^{-S}}]} \quad (2.6)$$

where C_s is the concentration of acceptor molecules within the spherical shell (in units of molecules per cubic nanometer), $\chi = \tau_D^{-1} R_0^S$, where τ_D is the radiative lifetime of the donor in the absence of acceptor molecules in units of nanoseconds ($\tau_D^{-1} = k_0$ in Table 3.1), S is the multipolar exponent ($S = 6$ for dipole-dipole interactions), and $\Gamma(x, y)$ is the incomplete gamma function. $\phi_{ret}(t)$ curves are obtained by dividing the TRPL decay of the NC-acceptor mixtures by the TRPL decay of the NCs in the absence of the acceptors. To reduce the number of fitting parameters in equation (2.6), we assumed that $r_2 = r_1 + 1$ nm, corresponding to the length of the A555 molecule. Hence, we fit $\phi_{ret}(t)$ curves with equation (2.6) to determine C_s and r_1 . The full derivation of equation (2.6) can be found in ref [52].

2.4 Single Particle Energy Transfer Microscopy

2.4.1 Sample Preparation

Single particle samples were prepared by spin coating a solution of ZnO NCs onto a cleaned quartz slide ($[ZnONCs] = 70-150$ nM; 1000-3000 RPM). ZnO NCs were synthesized following the procedure in section §2.1.1 with the only modification being that a single aliquot was taken after 6 hours of reaction time rather than multiple aliquot as set intervals. This yielded particles assumed to be ~4.5 nm, based on the size series depicted in Section §3.3. Quartz slides were cleaned following the procedure outlined in section §2.4.1.1. Quartz slides were used in favor of normal glass slides to reduce background fluorescence induced by UV excitation.

After deposition of the ZnO NCs the slide was used as-is for ZnO control experiments. For experiments with a mixture of ZnO NCs and dye molecules a solution of A555 dye was drop cast on top of the NCs. The droplet of dye was allowed to stand on the slide for about one minute before being removed by brisk nitrogen flow. Slides used for A555 control experiments were prepared in the same way just without the deposition of NCs.

Immediately prior to placing the sample on the microscope, a #1 glass coverslip was placed onto the sample side of the slide, sandwiching a drop of Immersol W 2010 immersion oil (Zeiss) between the slide and coverslip. This configuration is depicted in Figure 2.6. Here, the ZnO NCs are shown as gray circles and the A555 molecules as smaller red circles. The sample is shown with the NCs and molecules facing down to match with the configuration of the sample when it is mounted on the inverted microscope. Having solvent present over the NCs and molecules was necessary because the NC emission was not stable in air. Immersol oil was chosen because neither the NCs nor A555 molecules were soluble in it, allowing them to remain on the quartz surface after being immersed in immersol.

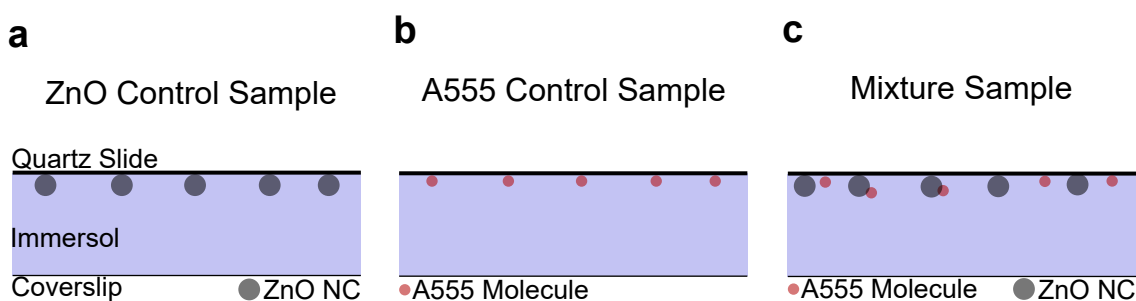


Figure 2.6: Cartoon illustration of single particle samples.

2.4.1.1 Slide Cleaning

Quartz slides were cleaned by immersing them in a 3:1 solution of sulfuric acid and hydrogen peroxide (Piranha solution) for at least 12 hours. Slides were then rinsed with milipour water and stored in spectrophotometric grade ethanol until use. After use, the Immersol oil was removed from the slides by a five minute ultra sonic bath in 2 M NaOH followed by thorough rinsing with milipour water. Oil-free slides were then subjected to the same Piranha cleaning described above before being used again.

2.4.2 Imaging Setup and Data Acquisition

Fluorescence images were acquired using the total internal reflection fluorescence setup pictured in Figure 2.7. The sample described in section §2.4.1 was placed onto an Olympus IX73 inverted microscope with the coverslip side facing down and brought into optical focus using transmitted white light. Next, a small drop of index matching oil was placed onto the top surface of the slide and a quartz prism was placed on top of the oil (not shown) and held in place so that the sample slide could move freely under the prism while maintaining good contact. Laser light was then be directed into the prism at such an angle that it underwent total internal reflection within the quartz slide at the interface with the immersol. The total internal reflection process produces an evanescent field on the immersol side of the slide. The intensity of the field decays exponentially with distance from the reflection surface, enabling excitation of particles and molecules on the slide surface while limiting the penetration of the field into the solution, reducing background signal.

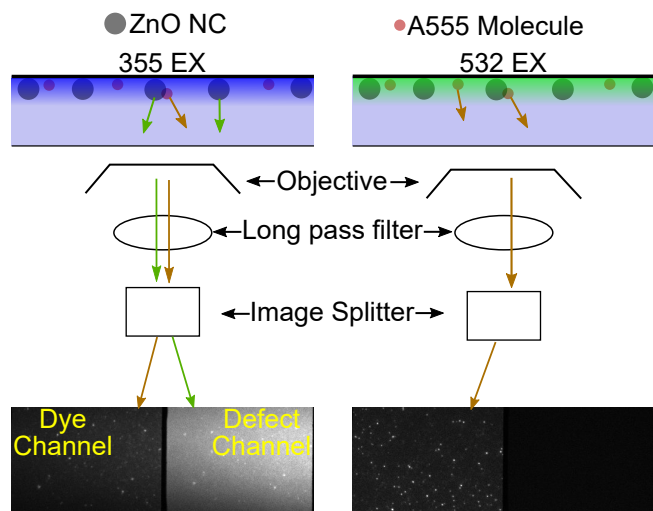


Figure 2.7: Cartoon depiction of the prism-type total internal reflection fluorescence microscopy setup.

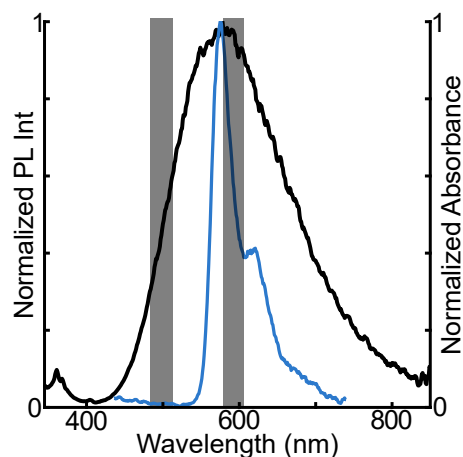


Figure 2.8: Emission spectra of 4 nm ZnO NCs (black line) and A555 (blue line). Dark shaded regions denote the wavelengths covered by the bandpass filters within the image splitter.

Illumination was provided by two laser sources, 355 nm and 532 nm. The 355 nm laser (Coherent Genesis CX) selectively excites the ZnO NCs while the 532 nm laser (Coherent Obis) selectively excites the A555 molecules. This excitation scheme allows for either simultaneous excitation of both ZnO and A555 or for one to be excited alone. Photons emitted from the sample were collected through a 60x microscope objective (NA = 1.2, Olympus) before passing through a longpass filter (cutoff wavelength: 440 nm). Then the photons enter the image splitter (Hamamatsu Gemini W-view) which uses a dichroic mirror (cutoff wavelength: 550 nm) to split the image in two based on wavelength. Each image then goes through a bandpass filter to further select the wavelengths of light that appear in the image. One of the bandpass filters was chosen so that photons emitted by A555 molecules will pass (585/40 bandpass). This forms the “dye channel”. The second bandpass was chosen to exclude any photons from A555 while still allowing photons from ZnO defect emission to pass (490/60 bandpass). This forms the “defect channel”. The two channels are finally projected onto an EMCCD camera (Andor iXon 897) to produce a single image, split vertically. Examples of these images are shown in figure 2.7 (bottom). Figure 2.8 shows the emission of ZnO NCs (black) and the emission of A555 (blue) with dark shaded rectangles denoting the wavelengths covered by the bandpass filters in the image splitter. The split images allow for the behavior of the NCs to be observed without interference from A555 by using the defect channel while also allowing for observations of the A555 in the dye channel. Data was acquired as a stream of fluorescence images from the camera, forming a “movie”. Movies were analyzed to determine the behavior of the ZnO and A555 separately after they had been mixed following the procedure outlined in section §2.4.3. Because the ZnO Defect emission is so broad the NC emission should appear in both channels, making the NCs easy to distinguish from non-NC objects.

In a typical experiment both laser sources are used to observe the locations of A555 molecules using 532 nm excitation and the behavior of ZnO NCs with 355 nm excitation. The sample is exposed to each laser in one second pulses with half a second of dark time between each pulse. This sequence is shown graphically in Figure 2.9. Alternating the excitation wavelength allows for A555 molecules to be observed independently of the NCs throughout the entire movie. The

movies can then be split up and each imaging condition (355 or 532 nm excitation) can be examined separately. Splitting up the movies and further analysis is discussed in the following sections.

2.4.3 Energy Transfer Microscopy Data Preparation

2.4.3.1 Laser switch point determination

Fluorescence movies acquired with the procedure described in Section §2.4.2 were analyzed using a custom MATLAB code. The first step was to load the movies into the MATLAB environment and then calculate the average intensity of the entire image at every frame of the movie, creating the average pixel intensity versus time plot shown in Figure 2.9a. Figure 2.9b shows a zoom-in of the first minute of Figure 2.9a. Here, the average pixel intensity (black line) shows distinct square-wave-like features due to the alternating excitation source. The blue and green triangles mark the frame where a laser turns on or off. The two lasers create two distinct intensity levels visible in Figure 2.9b. The higher intensity peaks are created by the 355 nm laser excitation, the lower intensity peaks by the 532 nm excitation. The 355 nm excitation creates larger background counts, causing those portions of the full-frame trajectory to be higher intensity. The peaks corresponding to the periods of 532 nm excitation show a gradual decrease as A555 molecules photobleach. The first derivative of the black line is used to determine when the individual laser on and off points are.

2.4.3.2 Region of interest selection

To analyze individual NC emission spots the movies were divided into regions of interest (ROIs) chosen by selecting bright objects in the defect channel during 355 nm excitation. During 355 nm excitation, this channel should only contain photon information resulting from NC defect fluorescence. After the locations were selected, the ROIs were created as 4×4 pixel boxes centered at the selected locations. Figure 2.10a-b shows the same fluorescence image created by averaging all the frames recorded during 355 nm excitation. Bright objects in the defect channel of Figure 2.10a were chosen and ROIs were drawn around them, shown in Figure 2.10b. These

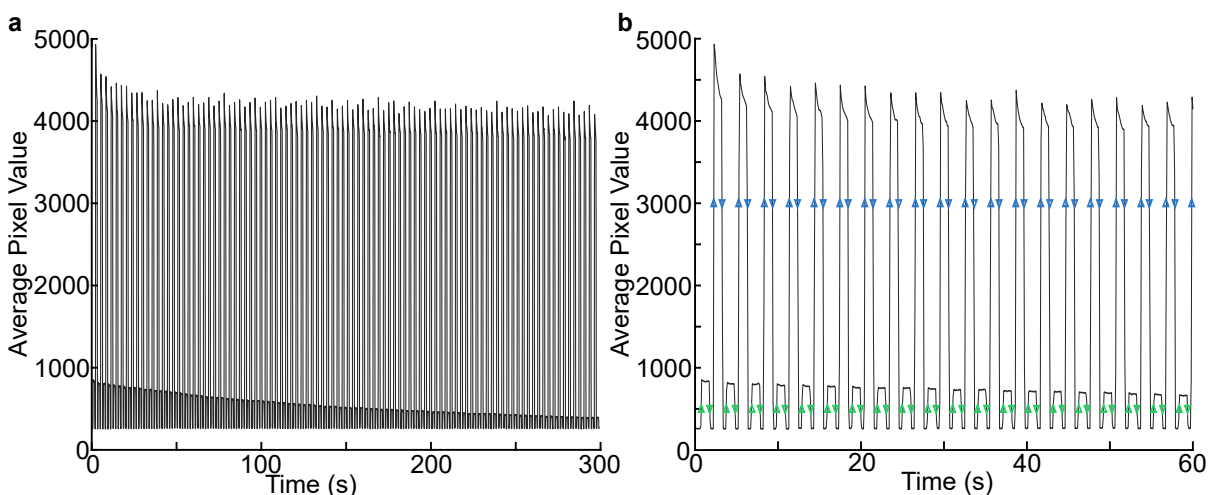


Figure 2.9: Representative average pixel value versus time trajectories from a movie recorded during alternating excitation. Average pixel values are averaged over the entire image for each frame of the movie. **a)** Full movie trajectory from a movie with 1 nM A555 deposited onto ZnO NCs. **b)** The same trajectory as shown in a) but with a shortened x-axis to better show the data. Blue triangles in b) mark the frames where the 355 nm laser turned on and off, the green triangles mark the frames where the 532 nm laser turned on and off.

ROIs will be referred to as the NC ROIs to distinguish them from ROIs created to quantify the background or ROIs covering A555 molecules (both discussed below).

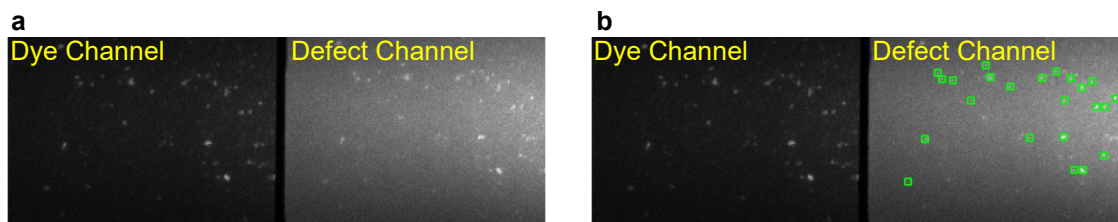


Figure 2.10: **a)** Fluorescence image of ZnO NCs under 6mW 355 nm excitation projected through the image splitter. The image is the average of all frames during 355 nm excitation (1078 frames). **b)** The same fluorescence image with ROIs plotted as green boxes.

Once NC ROIs were placed over emissive objects, matching background ROIs were created. These are identical square ROIs which were placed relatively close to each object but in an open area of the sample. This created a pair of ROIs, one over the emissive object and the other over an area with no emissive objects. Figure 2.11 is a representative fluorescence image of ZnO NCs. The

blue squares outline the NC ROI while the cyan squares outline the background ROI. This is done for all NC ROIs.

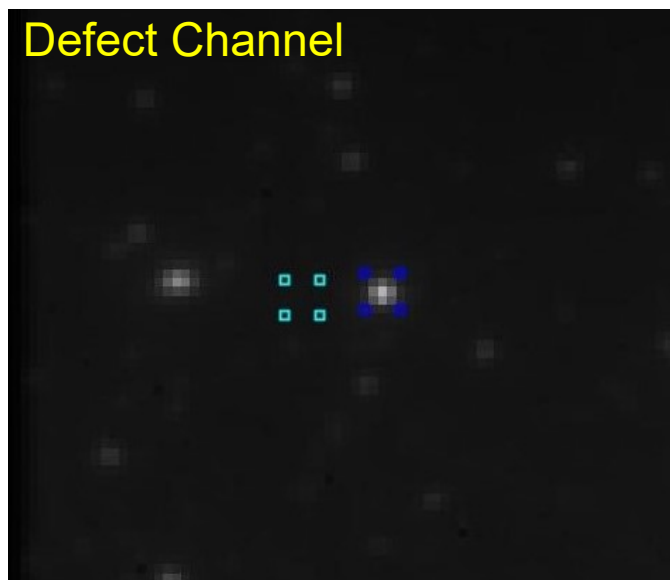


Figure 2.11: Cropped fluorescence image of ZnO NCs. The blue squares define the corners of the ROI placed over a NC, the cyan squares define the corners of the background ROI.

After creating the ROIs in the defect channel they were copied to the dye channel (including background ROIs). ROIs in the dye channel cover the same objects that they were drawn onto from the defect channel. To copy the ROIs, a geometric transformation matrix was created by selecting two sets of matching points, one in the defect channel and one in the dye channel (Figure 2.12a). These sets of points were then passed to the MATLAB function `fitgeotrans` which outputs a geometric transformation matrix. The transformation matrix is then applied to the vertices of the ROIs created in the defect channel, creating a new set of vertices which have been translated onto the dye channel. This transformation is applied to both the NC ROIs and the background ROIs. The result of this process are shown in Figure 2.12b. Here the ROIs which were originally drawn in the defect channel (green boxes) have been translated to the dye channel (yellow boxes). ROIs in the dye channel will capture any photons emitted by A555 acceptors during energy transfer events. Additionally, the ROIs in the dye channel were used in conjunction with the 532 nm excitation to

determine if any A555 molecules share an ROI with any NC donors. Background masks have been omitted from Figure 2.12b for clarity.

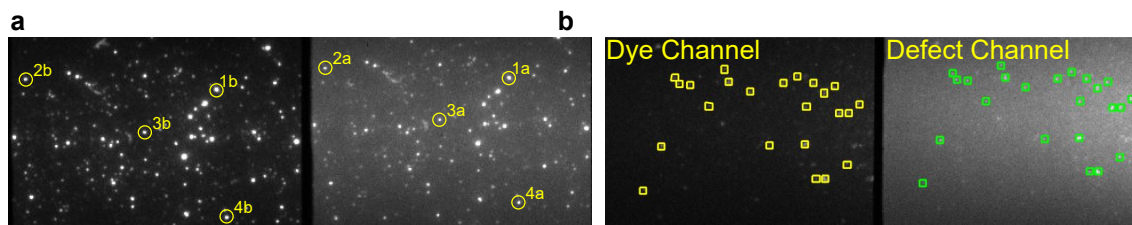


Figure 2.12: Fluorescence images of ZnO NCs under 6mW 355 nm excitation projected through the image splitter. The yellow circles in a) denote the spots that were used to calculate the transformation matrix. ROIs (green boxes) which were created in the defect channel have been transformed onto the dye channel (yellow boxes). Background ROIs are omitted from this image for clarity.

2.4.3.3 Trajectory calculation

After selecting the ROIs, the average pixel intensity in each was calculated at every frame of the movie, in both channels. This forms two intensity versus time trajectories for each object. An example of this can be seen in Figure 2.13a. Here, the intensity of a single object in both the defect and dye channels is shown as a black or blue line, respectively. Due to the intermittent nature of the excitation the trajectory is difficult to interpret without further processing. Using the laser on and off frame indexes determined earlier, the trajectories can be simplified by disregarding the intensity data during time periods when the laser is not on. Figure 2.13b and c show the result of this simplification. Figure 2.13b depicts the intensity trajectory during 355 nm excitation while Figure 2.13c depicts the trajectory of the same object just during 532 nm excitation. All the information present in Figure 2.13b and c is also present in a, however the laser pulse sequence makes it difficult to interpret in this form. Further analysis of these trajectories can be found in Chapter 5.

2.4.3.4 Dye Channel ROIs

ROIs were also drawn in the dye channel over objects that are emissive during 532 nm excitation. This was done in the same method described above however these ROIs were chosen using

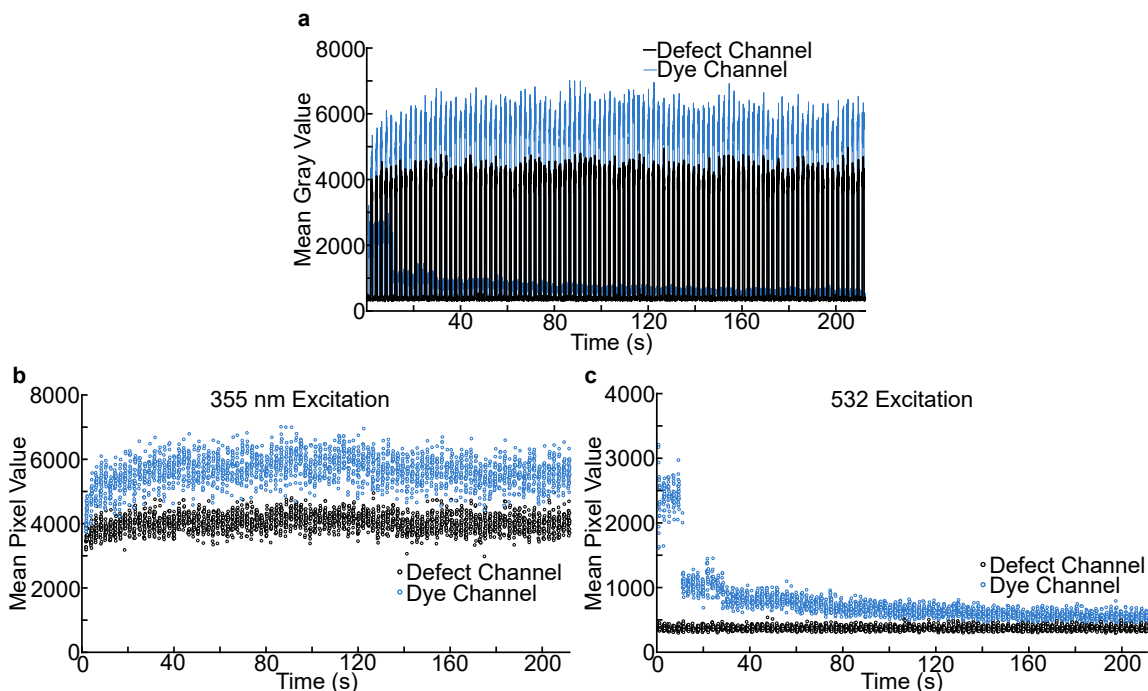


Figure 2.13: **a)** As-recorded intensity trajectory from a single particle. Black line depicts the intensity within the ROI in the defect channel and the blue line shows the intensity inside the ROI in the dye channel. **b)** Intensity trajectory for the same object in a) but only the intensity information during 355 nm excitation is shown. Each point represents the average intensity inside the ROI during one frame of the movie. **c)** The same as b) but only intensity information during 532 nm excitation is shown.

an image created by averaging frames during 532 nm excitation rather than 355 nm. This image should only show information about A555 molecules present on the sample surface because the 532 nm excitation should not affect the NCs. This can be seen in Figure 2.14 where the defect channel is dark. These ROIs were used as a way of counting the A555 molecules present in each movie. Additionally, these ROIs allowed for the observation of all of the A555 molecules present on the sample surface regardless of their distance from a NC donor.

2.4.3.5 Dye Trajectories

Similar to the trajectories for nanocrystal objects (Section §2.4.3.3) the ROIs created in the dye channel can be used to generate trajectories for individual objects. Because the ROIs were created using an image taken during 532 nm excitation the only emissive things on the sample should be A555 molecules. Figure 2.15a shows a full trajectory taken from an ROI in the dye channel.

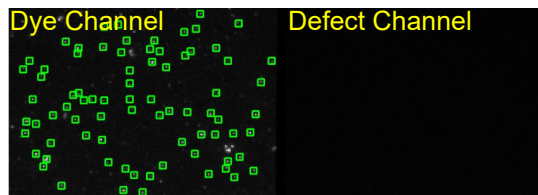


Figure 2.14: Fluorescence image of A555 molecules under 6mW 532 nm excitation. Green boxes connect the vertices of the ROIs associated with A555 molecules.

Similar to the trajectories NC ROIs, the dye trajectory shows square-wave behavior resulting from the alternating excitation wavelength except here the periods of higher intensity are periods of 532 nm excitation. Also similar to the nanocrystal trajectories, the dye channel trajectories can also be simplified using the laser on and off times determined previously. This simplified trajectory is shown in Figure 2.15b. Only the intensity values recorded during 532 nm excitation are shown. Here two sharp drops in intensity can be seen, one at very early times and another around 125 seconds. These are created by single A555 molecules photobleaching.

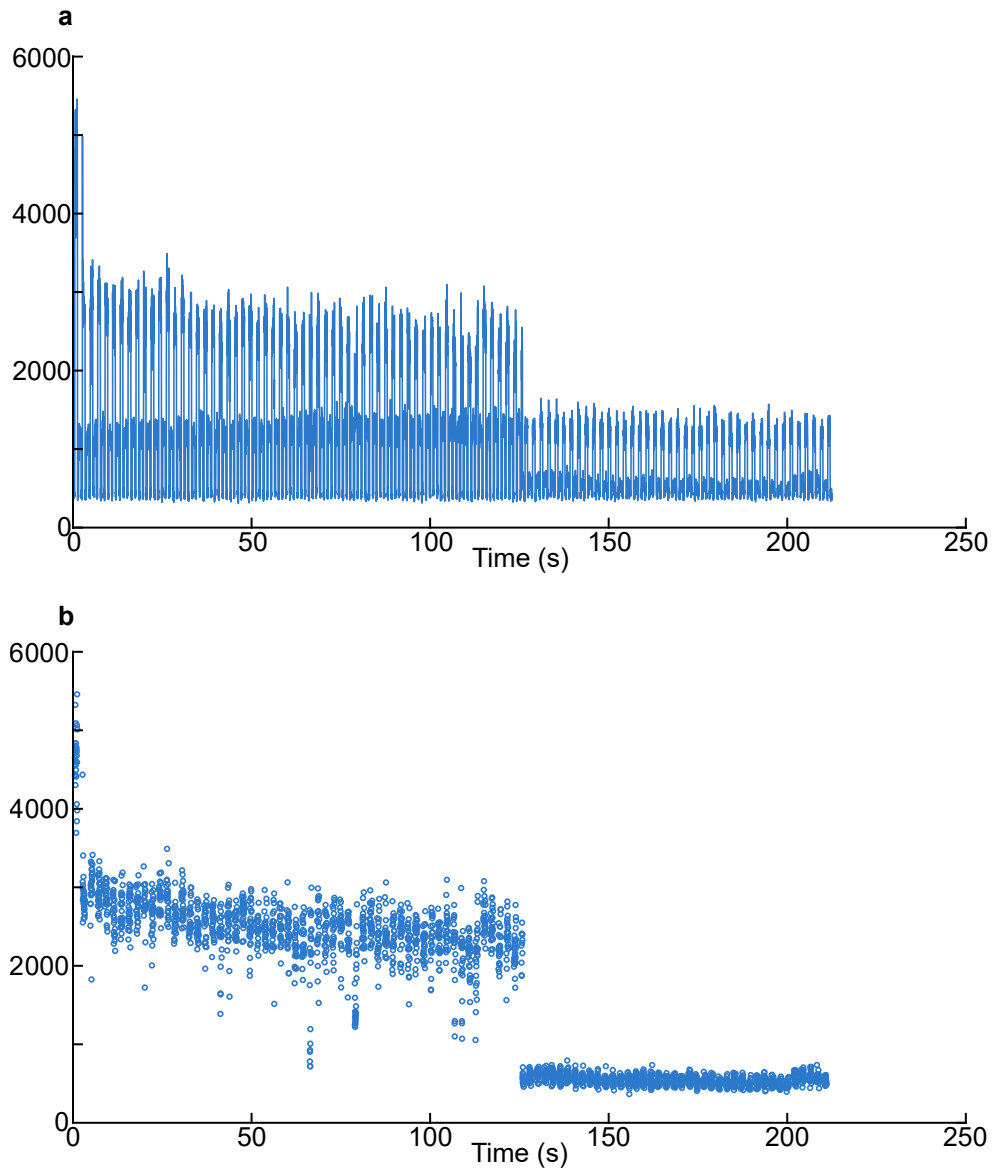


Figure 2.15: Dye channel trajectories. **a)** as-recorded intensity trajectory from a ROI created in the dye channel. Each blue point represents the average intensity inside the ROI during one frame of the movie. **b)** Intensity trajectory from the same object as a) but only information during 532 nm excitation is shown.

Chapter 3

Ensemble-level Energy Transfer Measurements Can Reveal the Spatial Distribution of Defect Sites in Semiconductor Nanocrystals⁴

3.1 Introduction

Applying defect-mediated energy transfer to a colloidal solution of ZnO NCs (described in Section §1.3) has the potential to reveal the average location of defect sites within an ensemble of NCs. This chapter describes the steps taken to use defect-mediated energy transfer as an analytical tool to locate defect sites in an ensemble of NCs.

3.2 Experimental Methods

See Section §2.2 for experimental methods.

3.3 Results

3.3.1 Size-dependent optical properties of ZnO NCs

Figure 3.1a shows normalized absorbance and photoluminescence (PL) spectra for three representative aliquots obtained at 2, 480, and 2400 min growth times. Those times correspond to initial, intermediate, and final NC growth stages respectively. Figure 3.1b shows the particle diameter as a function of growth time, as measured by TEM (see Section §2.1.2 for particle population analyses). The exciton absorbance peak at 330 nm for the 2 min sample shifts to longer wavelengths

⁴This chapter was published previously as: Zach N. Nilsson, Lacey M. Beck, and Justin B. Sambur, "Ensemble-level energy transfer measurements can reveal the spatial distribution of defect sites in semiconductor nanocrystals", *The Journal of Chemical Physics* 154, 054704 (2021) <https://doi.org/10.1063/5.0034775>. The manuscript has been reformatted here to fit the layout of this thesis. The experimental section has been incorporated into Chapter 2 and the majority of the SI figures are now included in the main text.

with increasing reaction time. The red shift indicates that the ZnO NC bandgap energy decreases as the NC size increases,⁷² in agreement with TEM data in Figure 3.1b. The 480 and 2400 min ZnO NC absorbance spectra exhibit a broad tail for > 400 nm. This spectral feature is due to NC aggregation and can be minimized if the NC concentration is < 100 nM (Section §2.1.2).

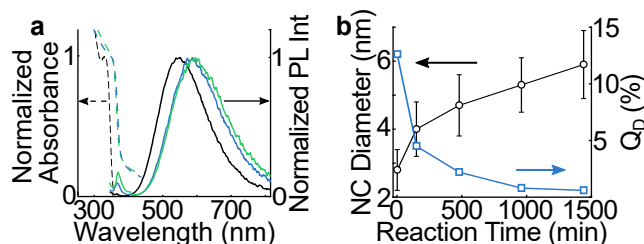


Figure 3.1: **a)** Absorbance spectra normalized to the exciton peak (dashed lines) and PL spectra (solid lines) normalized to the defect emission peak wavelength for three ZnO NC samples. Black, blue, and green lines represent spectra from 2, 480, and 2400 min growth times. **b)** Average NC particle diameter (black circles) and defect PL QY (blue squares) versus reaction time. The error bars represent the standard deviation from $N = 50$ particles. All spectra were measured in spectrophotometric grade ethanol and $[NC] = 70$ nM.

The normalized PL spectra in Figure 3.1a exhibit size-dependent features. The PL peak at 360 nm for the 2 min sample can be assigned to near-band-edge recombination. The position of this PL peak shows minimal red shift as the NCs grow, likely due to the near-band-edge state energy remaining the same as the NCs increase in size. The second PL feature is an intense and broad PL peak at 550 nm in the 2 min sample which shifts to longer wavelength with increasing reaction time. This broad PL peak has been assigned to defect emission, or radiative transitions between electrons in the conduction band and holes trapped at defect states in the NC band gap.⁵⁵ The defect states have been attributed to crystallographic defects such as O vacancies (V_O),^{55,58,73,74} and Zn vacancies (V_{Zn})^{53,75-77} or metal dopant atoms such as Cu^{78,79} and Mg.⁸⁰ Since ICP-AES analysis did not reveal Cu or Mg in these ZnO NCs, the defect PL peak is attributed to intrinsic defects, most likely V_O , in agreement with ZnO NC samples prepared under similar reaction conditions.^{30,55,56} van Dijken et al. also attributed the PL peak to V_O and observed a similar red shift in the defect PL peak with increasing NC size.⁵⁵ Those Authors attributed the red shift to a continuous decrease in band edge energy levels relative to a fixed defect energy level. In this

scenario, the defect PL peak red shifts because the energy difference between the band edges and the defect level decreases with increasing particle size. The fixed defect energy level suggests that the nature of the defect responsible for the sub-bandgap emission does not change with particle size.

Another size-dependent PL spectral feature is the decrease of the defect emission intensity with increasing NC size. Figure 3.1b shows that the defect PL QY decreases by a factor of 4 as the particle diameter and volume increase by 3- and 4-times, respectively. The decrease in defect PL QY and increase in band gap PL suggests that the number of emissive defect states decreases. Note, the measured radiative recombination rate k_0 is independent of NC size (Table 3.1). Hence, based on these size-dependent PL features, it can be inferred that the number and locations of defects within the NCs changes with reaction time but the nature of the defect sites responsible for emission do not change with reaction time.

Table 3.1: Photophysical properties of ZnO NCs. Uncertainties are 95% confidence intervals from TRPL fits. All confidence intervals were calculated using datasets containing 2000 data points.

NC Diameter (nm)	Defect PL QY (Q_D , %)	Radiative Decay Rate (k_0 , ns ⁻¹)	Trapping Rate (k_{qt} , ns ⁻¹)	Number of Traps (λ_t)
2.8	12.6	$1.7 \times 10^{-3} \pm$ 3.3×10^{-5}	$0.028 \pm 3.9 \times 10^{-4}$	2.2 ± 0.016
4.0	4.5	$1.4 \times 10^{-3} \pm$ 1.4×10^{-5}	$0.017 \pm 9.6 \times 10^{-5}$	2.5 ± 0.0085
4.7	2.2	$1.7 \times 10^{-3} \pm$ 2.2×10^{-5}	$0.022 \pm 2.0 \times 10^{-4}$	2.2 ± 0.011
5.3	0.8	$2.2 \times 10^{-3} \pm$ 5.2×10^{-5}	$0.030 \pm 5.0 \times 10^{-4}$	2.2 ± 0.020
5.9	0.6	$2.2 \times 10^{-3} \pm$ 5.2×10^{-5}	$0.027 \pm 4.3 \times 10^{-4}$	2.2 ± 0.020

3.3.2 Energy Transfer Measurements

Having characterized the emission profiles and defect PL QYs of these ZnO NCs, we studied the size- and concentration-dependent energy transfer behavior of the NC donors in the presence of A555 acceptors. To establish that energy transfer occurs between defect levels in the ZnO NCs and A555 the spectral overlap of the donor and acceptor was determined. Figure 3.2a shows the normalized emission of an ethanolic solution of 4.0 nm-diameter ZnO NCs compared to the absorption and emission spectra of A555. The defect emission peak overlaps with the A555 absorbance feature, which suggests that energy transfer will proceed via ZnO defect states rather than the band-edge states. The spectral overlap persisted for all ZnO NC sizes. J and R_0 were calculated for all NC donor-acceptor pairs using Equation (2.5) and assuming $\kappa^2 = \frac{2}{3}$ (Table 3.1),

following literature.³⁰ The assumption of randomly oriented dipoles may not be valid, as will be discussed below. The R_0 values decrease with increasing particle size because both J and Q_D decrease with increasing particle size. Interestingly, R_0 is larger than the particle radius for NCs with diameters < 5.3 nm, which has important consequences for interpretation of the donor-acceptor distances determined from TRPL data.

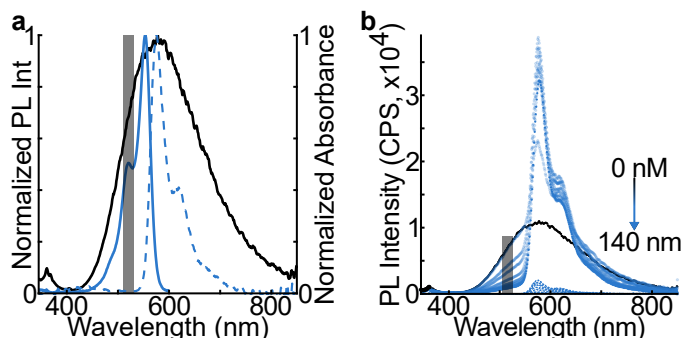


Figure 3.2: **a)** Normalized PL emission for 4.0 nm-diameter ZnO NCs (black curve) and normalized absorbance and PL emission of the A555 dye (solid blue and dashed blue respectively). **b)** Steady state emission spectra of the ZnO alone (black points) and of mixtures of the ZnO donors and A555 acceptors (blue points) with increasing [A555]. The mixture with the highest [A555] is indicated by the solid blue points. Dashed blue lines are emission spectra of A555 alone at the same concentrations and excited at the same wavelength used for the mixture experiments. The dark shaded rectangle in both panels represents the wavelength region investigated for TRPL experiments.

Steady state PL measurements indicate that photo-excited ZnO NCs induce A555 fluorescence via a defect-mediated energy transfer process. Figure 3.2b shows representative steady state PL spectra of 70 nM 4.0 nm-diameter ZnO NCs as a function of increasing A555 concentration. Upon exciting the bandgap of the ZnO NCs with 330 nm light, the defect emission intensity decreases over the wavelength range of 400 to 560 nm and the A555 fluorescence peak intensity at 585 nm increases with increasing bulk concentration of A555. The A555 fluorescence peak maximum did not shift with increasing bulk concentration, suggesting that dye aggregation does not occur under these conditions. Control experiments of A555 alone excited at the same wavelength and at the same concentrations used for the mixture experiments show weak fluorescence intensity (low intensity dashed red lines in Figure 3.2b). Additional control experiments show that sodium acetate does not quench the defect PL of these ZnO NCs (Section §2.2.2), indicated that the carboxylic

acid binding moiety alone does not induce the PL quenching behavior in the presence of A555. We observed no change in the bandgap PL intensity in the presence of the acceptor, indicating that energy transfer stems from defect energy levels rather than the bandgap energy levels. These results agree with Beane et al. who studied energy transfer between 3.2 nm-diameter ZnO NCs and Alexa Fluor[®] 594 dye.³⁰

TRPL measurements show that the ZnO NC defect PL decays faster in the presence of A555 acceptors. Figure 3.3a shows representative TRPL data of 4.0 nm ZnO NCs as a function of A555 acceptor concentration. Appendix A shows the TRPL data for all NC diameters and A555 concentrations. TRPL decays were measured over the spectral region indicated by the dark shaded rectangles in Figure 3.2 to ensure that A555 emission does not contribute to the TRPL decay measurement. The black data points represent the TRPL data of ZnO NCs alone in ethanol. In the absence of A555, the ZnO defect PL decay exhibited non-single-exponential decay kinetics, in agreement with literature.^{30,56} For all NC sizes and donor-acceptor ratios, the A555 acceptor accelerates the PL decay of the NC donors.

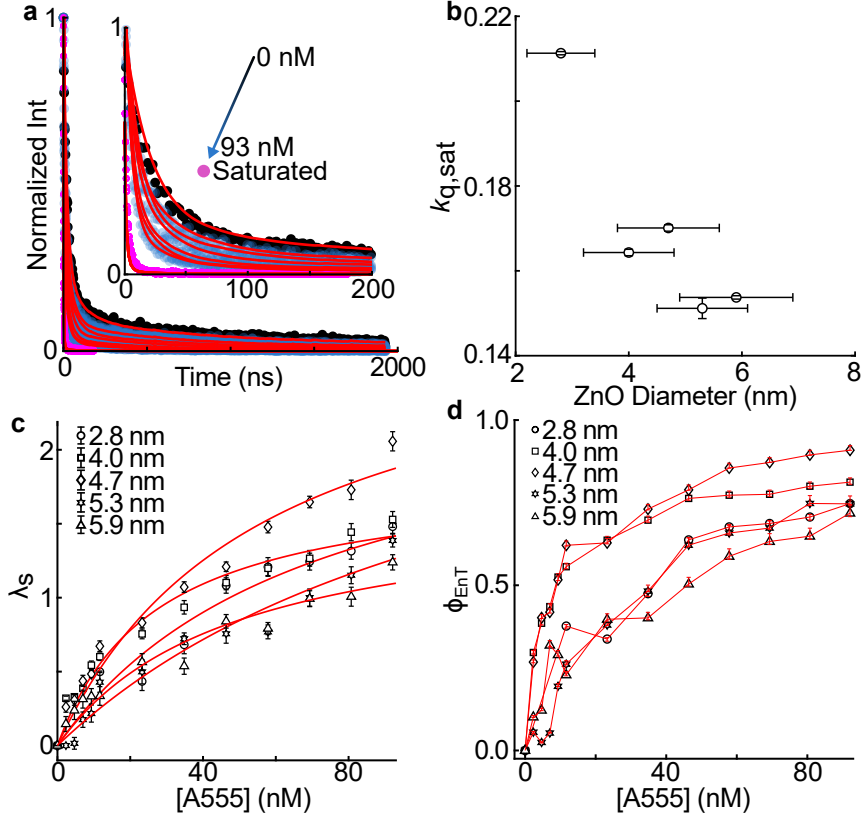


Figure 3.3: Stochastic binding model analysis of TRPL data. **a)** Normalized time-resolved PL decay traces for 4.0 nm ZnO NCs alone (black dots) and in the presence of increasing concentrations of A555 (blue dots). The violet dots represent $[A555]:[NC] = 1000:1$. Red lines represent fits to the first 100 ns of the data using Equations (2.1) and (2.2) for the NCs alone and mixtures, respectively. Half of the $[A555]:[NC]$ ratios have been omitted for clarity. **b)** k_q measured at saturated dye conditions ($k_{q,sat}$), $[A555]:[NC] = 1000:1$, as a function of NC size. Vertical error bars represent 95% confidence intervals on the fitted values of $k_{q,sat}$. Horizontal error bars represent the standard deviation from a Gaussian fit to the nanocrystal diameter distribution from Section §2.1.2. **c)** λ_s as a function of bulk $[A555]$ for different NC sizes. Error bars represent 95% confidence intervals. The red solid lines are fits to a Langmuir adsorption isotherm, Equation (3.1). **d)** ϕ_{EnT} versus bulk $[A555]$ for different NC sizes, red lines are fits to Equation (2.3).

3.3.3 Stochastic Binding Model Analysis

The donor-acceptor distance (r) for these ZnO NC-A555 donor-acceptor pairs was determined by analyzing the TRPL data using the stochastic binding model.⁴⁶ r represents the ensemble average donor-acceptor distance, or the average distance between defects in the ZnO NCs and the molecular acceptors. To do so, the TRPL decay curve of the donor in the absence of the acceptor was fit with Equation (2.1). The black data points and solid red lines in the Figure 3.3a show

representative fit results for 4.0 nm NCs in ethanol, yielding $k_0 = 1.4 \times 10^{-3} \text{ ns}^{-1} \pm 1.4 \times 10^{-5} \text{ ns}^{-1}$, $k_{qt} = 0.017 \text{ ns}^{-1} \pm 9.6 \times 10^{-5} \text{ ns}^{-1}$, and $t = 2.5 \pm 0.0085$, in agreement with Beane et al. for similar size ZnO NCs.³⁰ The photophysical parameters are independent of NC size (Table 3.1), suggesting that the PL QY decreases with NC size because the number of emissive defect states decreases with increasing reaction time.

Having analyzed the TRPL decay data of the NC donors alone, the PL decay curves of the donors in the presence of A555 were fit using Equation (2.2). λ_s and k_q were fit using experimentally determined values for k_0 , k_{qt} , and λ_t that were obtained from TRPL experiments of the donor alone (i.e., Equation (2.1)). However, the error in λ_s and k_q were large. To minimize the error in λ_s and k_q , experiments were performed at large [A555]:[NC] ratios (e.g., saturated condition in figure 3.3a) where the TRPL decay curves were independent of bulk [A555], likely because λ_s saturates and k_q is fixed. Hence, for all NCs studied herein, the energy transfer rate was determined at a saturated bulk acceptor concentration (denoted $k_{q,sat}$). To do so, TRPL decay curves at [A555]:[NC] = 1000:1 were fit using Equation (2.2), yielding λ_s and $k_{q,sat}$ values with the 95% confidence intervals shown Figure 3.3b-c. Figure 3.3b shows that $k_{q,sat}$ decreases with increasing NC diameter. The $k_{q,sat}$ trend could be due to a change in r because Förster theory predicts that k_q scales with $\tau_D^{-1} \left(\frac{R_0}{r}\right)^6$ for a single donor-acceptor pair.¹⁹ To test this hypothesis, r was determined using the SB model, which takes into account the NC size-dependent τ_D and R_0 and importantly, that multiple acceptors may quench the PL of a single NC donor.

To quantify R , TRPL data in the low acceptor concentration regime was fit using Equation (2.3) and only one adjustable parameter, λ_s . The blue data points and solid red lines in Figure 3.3a-inset show PL decay data and fit results from 4.0 nm NCs as a function of bulk [A555]. As expected, Figure 3.3c shows that λ_s increases with bulk [A555] for all NC sizes studied. Note the small 95% confidence intervals in Figure 3.3c that result from the aforementioned fitting procedure. These data were fit with a Langmuir adsorption isotherm (Section §3.3.5, Equation (3.1), red lines) to obtain the equilibrium binding constant, K . Figure 3.6 shows that K is independent of NC size, indicating that the binding affinity of A555 to NC surfaces does not change with size. This result

also suggests that changes in energy transfer efficiency among the different NC sizes are not due to changes in NC surface chemistry or the nature of the NC-A555 interaction.

Having determined k_q and λ_s , ϕ_{EnT} was calculated as a function of bulk [A555] using Equation (2.3). Figure 3.3d shows that ϕ_{EnT} increases with [A555] because acceptor molecules are more likely to be located within a distance R_0 from the NC surface. Finally, r was determined from these energy transfer versus bulk [A555] data using Equation (2.4). How and why R changes with NC size will be discussed in Section §3.4.

3.3.4 Restricted Geometry Model Analysis

The TRPL data sets in Figure 3.3a and Appendix A were analyzed using the restricted geometry model to obtain r_1 , which represents the average distance between defects and the nearest A555 acceptor. Figure 3.4 shows ϕ_{ret} decay curves for 4.0 nm ZnO NCs at three representative bulk A555 concentrations. ϕ_{ret} represents the donor decay curve in the presence of A555 divided by the donor decay curve in the absence of A555. Fitting the TRPL data using Equation (2.6) yields C_s and, importantly, r_1 . C_s was converted into units of dye molecules per NC and compared those values to λ_s in Section §3.3.6. There is good agreement between λ_s and C_s even though the restricted geometry model does not assume that the distribution of dyes around the NCs follows Poisson statistics.

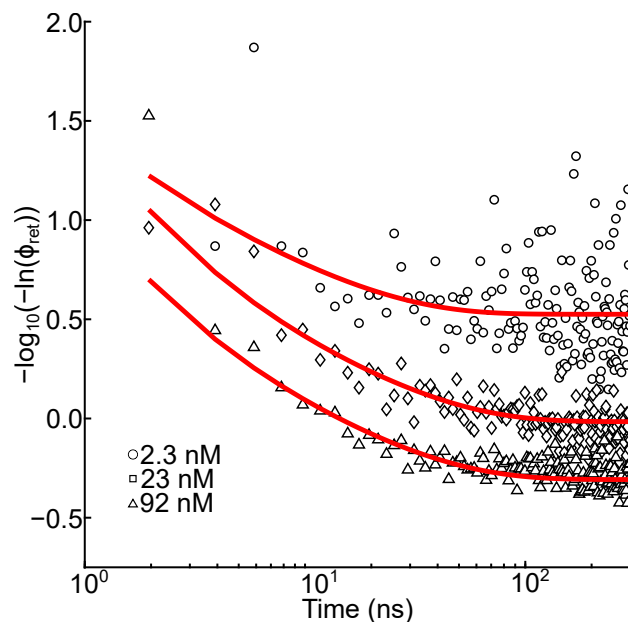


Figure 3.4: Restricted geometry model analysis of TRPL data. ϕ_{ret} decay curves of 70 nM 4.0 nm ZnO NCs for three different bulk A555 concentrations. Red lines represent fits to Equation (2.6).

Figure 3.5 compares r and r_1 versus NC diameter at $\lambda_s \approx 1$ molecule per NC. Both values decrease with increasing NC diameter, indicating that the distance between the emissive defect sites and surface adsorbed A555 molecules decreases as the NC size increases. Since the molecules cannot penetrate into the NC core, this trend suggests that the defects move closer to the NC/liquid interface as the NC grows. R is significantly larger than r_1 and closely follows the size-dependent R_0 values. In the Discussion section, we compare the donor-acceptor distances obtained from each model and consider whether the optical measurements and associated analyses can reveal the spatial distribution of emissive defect sites in the ZnO NCs.

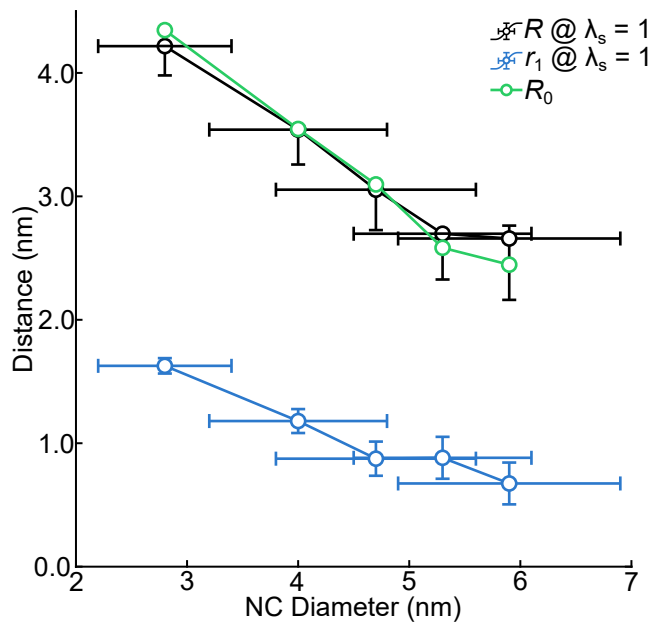


Figure 3.5: Comparison of NC donor-A555 acceptor distances R and r_1 obtained from the SB and RG models, respectively.

3.3.5 Langmuir adsorption fitting

λ_s vs [A555] data (Figure 3.3c) were fit with Equation (3.1):

$$[A_{ad}] = \frac{K[A]}{1 + K[A]} S_0 \quad (3.1)$$

Where $[A_{ad}]$ is the concentration of adsorbed dye molecules, K is the Langmuir equilibrium constant, $[A]$ is the concentration of dye added to the solution in nM, and S_0 is the number of available binding sites. Here, $\lambda_s = [A_{ad}]$. Values of K obtained from the fits are shown in Figure 3.6.

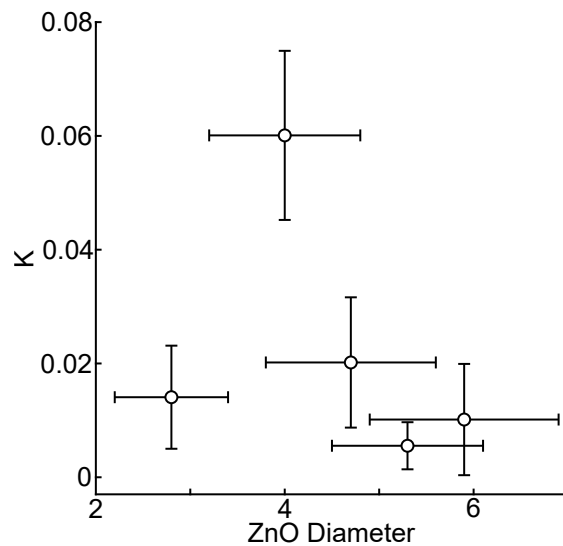


Figure 3.6: Equilibrium binding constant, K , calculated with Equation (3.1) vs NC diameter. Error bars on K are the 95% confidence intervals of the fit. The error on the NC diameter is the standard deviation of the population.

3.3.6 Comparison of surface concentration of dye molecules: C_s vs. λ_s

The restricted geometry model allows for the independent determination of the number of acceptor molecules participating in energy transfer. The model reports on the volume-corrected concentration of acceptors in the spherical shell surrounding the NC. We converted this value (C_s) to the number of attached acceptors per NC by multiplying C_s by the volume of the shell. Results of this procedure are compared to values of λ_s obtained for the same NC:A555 ratios in Figure 3.7 for each NC size.

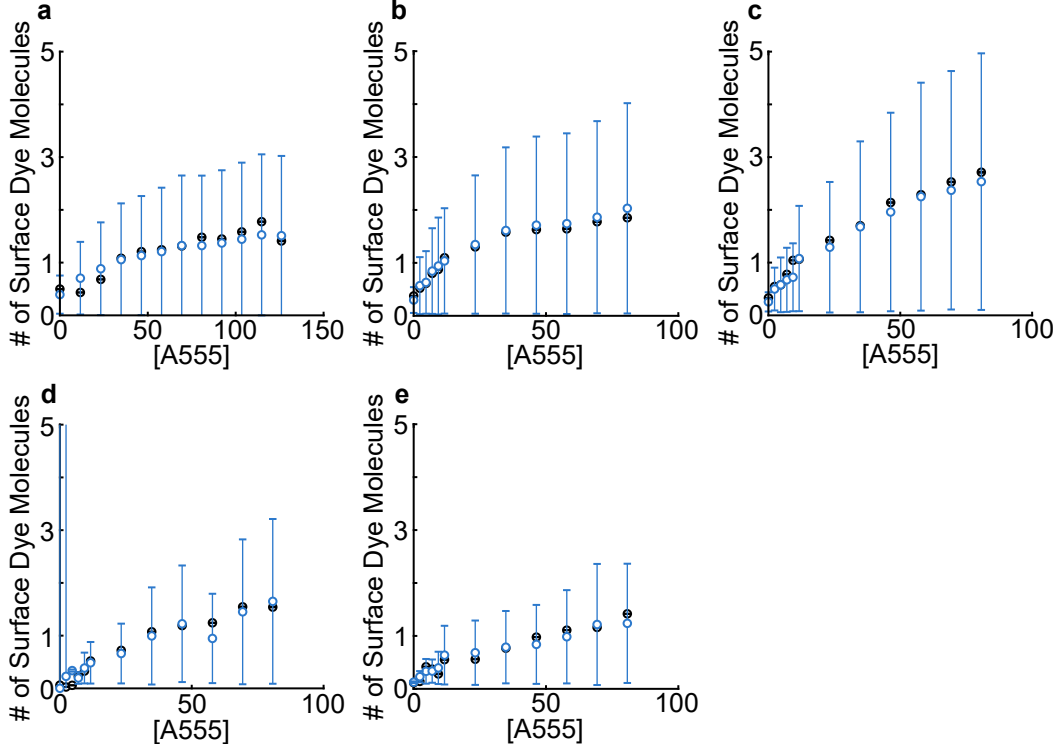


Figure 3.7: Comparison of the number of attached acceptor molecules per NC as determined by the stochastic binding model (λ_s , black lines) and by the restricted geometry model (C_s , red lines). a) 2.8 nm diameter NCs, b) 4.0 nm diameter, c) 4.7 nm diameter, d) 5.3 nm diameter, and e) 5.9 nm diameter. Error bars are 95% confidence intervals from the respective fits.

3.4 Discussion

3.4.1 Comparison of donor-acceptor distances

Can ensemble-level energy transfer measurements reveal the locations of emissive defects in semiconductor NCs? Here we compare the D-A distances obtained from each model to the geometry of the NC-dye system and discuss the capability of each model to reveal the location of defect sites in the NCs.

Figure 3.8 compares the average D-A distance obtained from the SB model (i.e., R) for small and large ZnO NCs when the defect site responsible for energy transfer is located either at the surface or the center of the NC. The scheme considers extreme NC-dye configurations that correspond to the minimum and maximum possible D-A values in the system. We illustrate r and R_0 in

Figure 3.8 as circles with center positions located at the defect site and with NC size-dependent r and R_0 radii as shown in Figure 3.5. For the small 2.8 nm NCs, r or R_0 are much larger than the particle radius (Figure 3.8a,b). In this situation, the SB model considers that all defect-dye configurations contribute to energy transfer, regardless of the position of the defect site, because all surface adsorbed dye molecules are located within R_0 ($\phi_{EnT} > 0.5$, indicated by purple highlight ovals in Figure 3.8). Hence, the SB model cannot reveal the locations of emissive defect sites in the small ZnO NCs or, in general, when R_0 is larger than the NC radius.

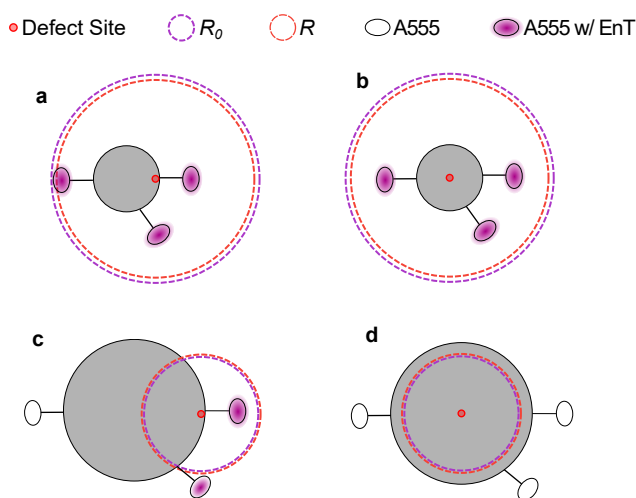


Figure 3.8: **a – b)** Two-dimensional representations of defect mediated energy transfer from 2.8 nm-diameter NCs (large gray circles) to A555 acceptor molecules when the defect site is located a) at the surface or b) at the center of the NC. The small and large dashed lines are circles with radii R and R_0 and are centered at the defect site responsible for radiative emission. **c – d)** Same as (a-b), but for 6.0 nm-diameter ZnO NCs. The 1 nm-long A555 molecules, NC radii, r , and R_0 are drawn to scale.

On the other hand, r and R_0 are smaller than the NC radius for the large 6.0 nm ZnO NCs (Figure 3.8c-d). If the defect site is located at the NC surface as in Figure 3.8c, then dye molecules located on the opposite side of the NC exhibit $\phi_{EnT} \ll 0.5$ (indicated by white oval in Scheme 2c) because R for that particular NC-dye configuration is much larger than R_0 . If the defect site is located at the center of the NC as in Scheme 2d, then the r values for any dye are slightly greater than R_0 , yielding $\phi_{EnT} < 0.5$. Since $\phi_{EnT} > 0.5$ for the large NCs when $\lambda_s = 1$ (Figure 3.3d), the

defect sites are likely not located in the center of the NCs. Hence, ensemble-level measurement and the SB model analysis can rule out the extreme case that the emissive defect sites are located at the center of large NCs. However, the SB model does not reveal further real space information regarding the location of the defects because R_0 is comparable to the NC radius and there are a wide range of possible defect-dye configurations that could contribute to energy transfer.

The situation changes for the RG model (Figure 3.9). For the small ZnO NCs, the average D-A distance obtained from the RG model (i.e., r_1) is approximately equal to the NC radius even though R_0 is still much larger than the NC (Figure 3.9a-b). Hence, the RG model identified a physically meaningful D-A distance that matches the geometry of the system even though the model assumes nothing about the shape and size of the NC. While the RG model does not reveal where the defect sites are located in the small NCs for the same reasons as discussed above, the RG model apparently provides more physically meaningful results than the SB model for situations where R_0 is much larger than the NC radius.

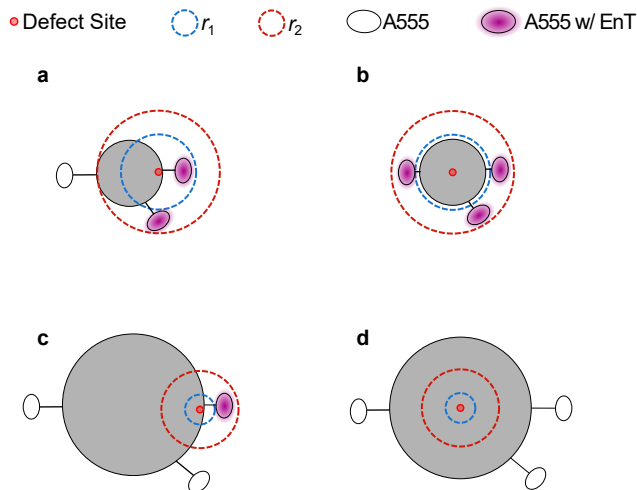


Figure 3.9: a – b) Two-dimensional representations of defect mediated energy transfer from 2.8 nm-diameter NCs (large gray circles) to A555 acceptor molecules when the defect site is located a) at the surface or b) at the center of the NC. The small blue circles represent r_1 and are centered at the defect site responsible for radiative emission. c – d) Same as (a-b), but for 6.0 nm-diameter ZnO NCs. The 1 nm-long A555 molecules, NC radii, r_1 , and r_2 are drawn to scale.

For the large NCs, the RG model predicts that the nearest possible acceptor molecule is located, on average, 0.5 nm from the defect (Figure 5). The small separation distance strongly suggests that emissive defect sites responsible for energy transfer are located at the NC surface (Figure 3.9c) instead of the core (Figure 3.9d). If the defects were located at the core, then we would not expect to observe energy transfer in TRPL measurements because core defects would be too far away from the acceptor molecules. While both models indicate that the emissive defects in the large ZnO NCs are likely located at the surface, the RG model pinpoints the location of defects to surface or near-surface locations. Hence, we conclude that the RG model has the potential to yield meaningful information regarding the real space distribution of emissive defects sites in semiconductor NCs, especially when R_0 is less than the NC radius.

3.4.2 Size independent energy transfer efficiency

We expected energy transfer to increase with decreasing NC size because there is a higher probability that an acceptor molecule is located within a distance R_0 from the defect site for the small NCs (Figure 3.8a-b vs. c-d). However, $\phi_{EnT} = 0.5$ at $\lambda_s = 1$ for all NC sizes (Figure 3.10). One explanation for the size-independent energy transfer behavior is that the assumption of random orientation between donors and acceptors is not valid in these systems (i.e., $\kappa^2 \neq \frac{2}{3}$ in Equation (2.5)). One possibility is that the small NCs have a higher concentration of defect dipoles that cannot participate in defect-mediated energy transfer. The small NCs likely have a higher concentration of emissive defects, but those defects may be distributed throughout the crystallites such that the orientation of the defect dipoles do not align with surface adsorbed molecules. The variable arrangement of defects in the small NCs could stem from poor crystallinity at early growth stages. It is possible that the orientation factor for the small NCs is $< \frac{2}{3}$ and, therefore, the R_0 values in Figure 3.8 may be overestimated.

3.4.3 Limitations of ensemble-level defect-mediated energy transfer studies

Unfortunately, the ensemble-level measurement approach prevents us from directly observing the spatial distribution of emissive defects and assessing the validity of underlying assumptions of

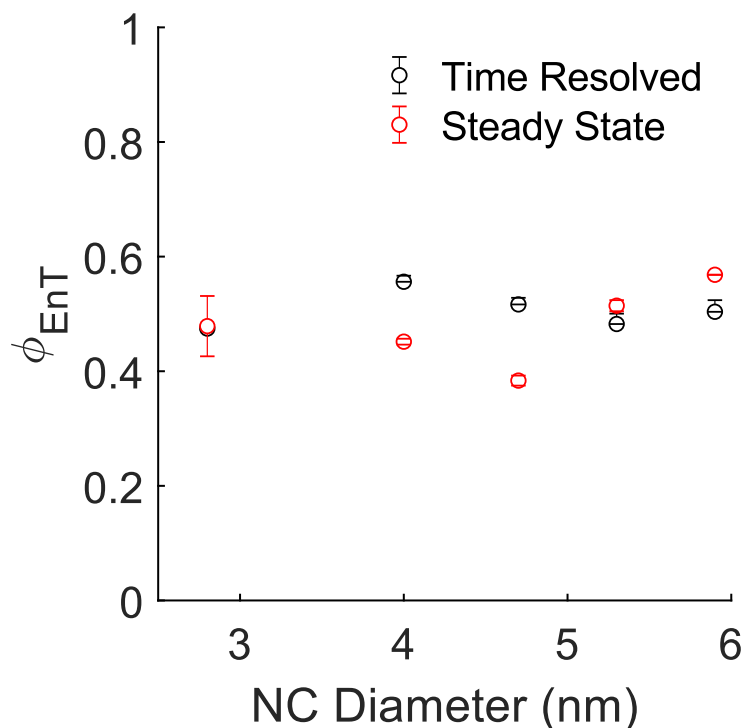


Figure 3.10: Comparison of ϕ_{EnT} values at $\lambda_s = 1$ for all NC sizes. The number of A555 molecules participating in energy transfer was determined from the SB model. The black data points are the result of main text Equation (2.6) while the red points are calculated from steady state data using $\phi = 1 - \frac{I_0}{I}$ where I and I_0 are the steady-state intensity of the donor in the presence and absence of the acceptor molecules, respectively.

the SB and RG models (e.g., $\kappa^2 = \frac{2}{3}$). In addition, ensemble-level energy transfer measurements cannot distinguish surface adsorbed molecules that participate in energy transfer from those that do not (e.g., purple shaded versus white ovals in Figure 3.9a). Distinguishing energy-transfer-active versus spectator molecules could help to understand whether all molecules contribute equally to defect PL quenching, which is an assumption in the SB model. Second, both models assume that donor dipoles are located at the NC center, which is likely not valid. Single molecule, super-resolution fluorescence microscopy experiments performed at the single NC-level could overcome both limitations. Single molecule energy transfer experiments could pinpoint the locations of emissive defect sites and, at the same time, distinguish energy-transfer-active from spectator molecules by selectively exciting the donor and acceptor species in the NC-dye conjugate, as Hadar et al. showed in single molecule experiments of CdSe/CdS nanorod donors in the presence of multiple

Atto 590 acceptors.⁵⁰ Selectively excitation of surface-bound versus bulk acceptor molecules is not possible in conventional ensemble-level experiments. Polarization-dependent single molecule energy transfer measurements could also reveal the orientation of the donor and acceptor dipoles, especially for nanoparticle donors with asymmetric shapes.

3.5 Conclusions

Defect mediated energy transfer between ZnO NC donors and Alexa Fluor[®] 555 acceptor molecules was studied using TRPL measurements. TRPL decay curves were analyzed using two different models, it was concluded that the RG model yielded physically meaningful donor-acceptor distance measurements that agreed with the geometry of the NC-dye system. Furthermore, the RG model predicted that emissive defect sites are, on average, 0.5 nm away from the donor molecules bound to 5 nm-diameter ZnO NCs. This study shows that ensemble-level energy transfer measurements have the potential to provide insight into the distribution of defects in semiconductor NCs. Understanding how the defect site distributions influence energy and charge flow between NCs and molecules could lead to the design of efficient light-harvesting NCs for photocatalysis and sensing applications.

Chapter 4

Molecular Reaction Imaging of Single-entity

Photoelectrodes⁵

4.1 Introduction

Understanding photo-induced charge transfer reactions between light absorbing semiconductors and molecular substrates is critical for solar energy conversion applications. The semiconductor/liquid electrolyte junction in a photoelectrochemical cell is a convenient interface to study the fundamental processes that determine the reaction quantum yield: charge generation, separation, transport, and interfacial charge transfer.^{81–83}

The principle processes at an illuminated n-type semiconductor/electrolyte interface are shown in Figure 4.1a. The first step involves charge carrier generation via light absorption that produces electrons and holes in the conduction and valence bands, respectively. The productive processes that contribute to photocurrent in the external circuit include majority carrier (electron) extraction at the back contact (step 2), minority carrier (hole) transport to the solid/liquid interface (step 4), and interfacial hole transfer with reduced species in the electrolyte (step 6). Unproductive charge recombination processes include electron-hole recombination in the bulk or in the space charge region (step 3), majority carrier diffusion to the interface (step 7) and subsequent reaction with oxidized species in the electrolyte (step 9). In addition to the conduction and valence band processes, electrons and holes could also flow into and out of surface states.⁸⁴ For example, surface adsorbed anions such as OH^- on a metal oxide surface could capture holes (step 5).⁸⁵ The oxidized surface state (i.e., OH^\bullet species) could participate in interfacial charge transfer with oxidized species in the

⁵This chapter was published previously as: Nilsson, Z.; Van Erdevyk, M.; Wang, L.; Sambur, J. B. Molecular Reaction Imaging of Single-Entity Photoelectrodes. ACS Energy Lett. 2020, 5 (5), 1474–1486. <https://doi.org/10.1021/acseenergylett.0c00284>.

electrolyte (step 10).⁸⁶ On the other hand, the oxidized surface intermediate could capture majority carriers (step 8), which is an unproductive charge recombination process.

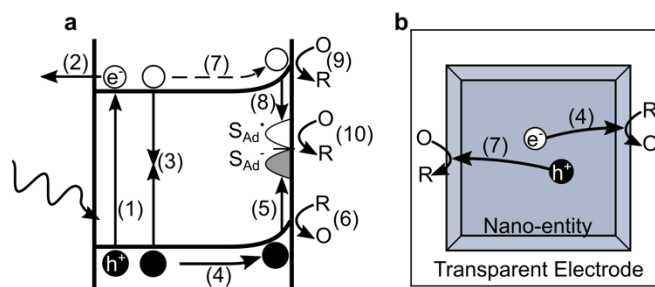


Figure 4.1: Principle processes in semiconductor photoelectrochemistry. **(a)** Energy level diagram and rate processes at an illuminated n-type bulk semiconductor/electrolyte interface (e.g., TiO₂). (1) carrier generation, (2) majority carrier collection, (3) electron-hole recombination in the bulk or in the space charge region, (4) minority carrier transport to the electrode surface, (5) minority carrier capture by surface adsorbed species (e.g., OH⁻), (6) minority carrier interfacial charge transfer via the valence band, (7) majority carrier transport to the electrode surface, (8) majority carrier capture by the oxidized form of the surface adsorbed species (e.g., OH[•]), (9) majority carrier interfacial charge transfer via the conduction band, and (10) charge transfer via surface states. **(b)** Top-down view of a n-type nano-entity photoelectrode (e.g., TiO₂ or BiVO₄particle) on a transparent electrode (e.g., ITO). Process (4) represents minority carrier transport from the particle interior to the surface. Process (7) represents majority carrier transport to the surface.

One fundamental problem that impedes progress in the field of semiconductor photoelectrochemistry is that we do not understand how materials heterogeneity influences the rates and efficiencies of the principle processes in Figure 4.1a. Semiconductors have bulk defects and impurities as well as irregular surface structural features that produce a distribution of active sites (e.g., surface facets, edge sites, kink sites).^{87,88} Bulk or near-surface defects or impurities can impact the efficiency of the individual steps in various ways. If ionized impurity atoms act as n-type dopants and donate electrons to the conduction band, then the number and position of the impurities will influence the charge distribution and electric potential gradient in the space charge region that contributes to charge separation at the solid/liquid interface.⁸⁹⁻⁹² Surface defects or heterogeneity could influence interfacial charge transfer rates and/or mechanisms of the fuel-forming reactions.⁹³⁻⁹⁵ This materials heterogeneity problem is exacerbated in nanomaterials^{96,97} that are promising for photoelectrochemical applications because the nanoscale dimensions limit charge

transport distances (steps (4) and (7) in Figure 4.1b).^{98–101} Because the synthesis of defect free nanomaterials is likely impractical, new experimental tools are needed in the field of semiconductor photoelectrochemistry to address this materials heterogeneity challenge.

This perspective article focuses on emerging molecular reaction imaging methods in the field of semiconductor photoelectrochemistry. We focus on single molecule-level and ensemble-level reaction imaging methods that have been applied to study single nano-entity photoelectrodes under working photoelectrochemical conditions. The single molecule methods spatially resolve interfacial reactivity with nanoscale spatial resolution (typically 20 nm). The nano-entities include metal oxide particles, nanorods, and two-dimensional layered materials such as MoS₂ and MoSe₂ nanoflakes. We review recent developments in single molecule fluorescence microscopy (SMFM) and bright field optical microscopy that enable direct investigations of underlying steps in photoelectrochemical reactions. This perspective article discusses how those imaging methods measure (1) reaction intermediate formation and consumption, (2) surface recombination events, and (3) charge transport distances. For each imaging approach, we discuss opportunities for future research and provide an outlook to couple optical microscopy techniques with electron or X-ray micro-spectroscopy characterization methods. We do not discuss single molecule imaging of single nano-entity chemical catalysis, electrocatalysis, or photocatalysis studies because those topics have been reviewed previously.^{102–107} In addition, we do not discuss powerful scanning probe-based approaches that have been used to spatially resolve thin film photoelectrodes.^{108,109}

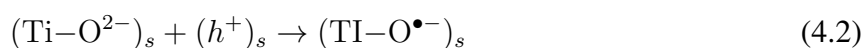
4.2 Imaging Photoelectrochemical Reactions via SMFM

4.2.1 Reaction intermediate imaging

Energy and environmentally-relevant chemical reactions such as the water oxidation reaction and CO₂ reduction reaction involve multiple electron transfer steps and reaction intermediates. Ensemble-level spectro-electrochemical measurements have been used to characterize the chemical identify and dynamics of the reaction intermediates,^{110–113} but it is challenging to spatially resolve the reaction intermediates on electrode surfaces, especially on nanostructured electrodes.

Here we describe recent advances in super-resolution SMFM of reaction intermediates on single nano-entity photoelectrodes.

In 2019, Sambur et al.¹¹⁴ used SMFM to spatially and temporally resolve the one-electron reaction intermediate in the water oxidation reaction on the surface of single TiO₂ nanorod photoanode. One-electron intermediates such as (Ti–OH•)_s or (Ti–O•)_s are produced at photo-excited TiO₂ surfaces in aqueous solution via the elementary reaction steps in Equations (4.1) and (4.2)^{113,115,116}



where $(h^+)_s$ is a surface hole and $(\text{OH}^\bullet)_s$ is a surface adsorbed hydroxyl radical group (i.e., $(\text{OH}^{\bullet-})_s$). Here we have assumed that the solution pH is more basic than the isoelectronic point of TiO₂ (5.5) and therefore OH⁻ covers the TiO₂ surface. For simplicity and clarity, Equation (4.2) was not considered in the following study because the experiments were performed in pH 8.3 electrolyte and the fully deprotonated surface condition is observed under strongly basic conditions (pH 13).¹¹⁷ Hence, the first interfacial hole transfer step proceeds via Equation (4.1) with a rate constant k_1 . The units of the intermediate species concentration are molecules/particle and the units of the rate constant k_1 are particle s^{-1} .

The Authors tracked the surface concentration of the one-electron intermediate $(\text{OH}^\bullet)_s$ using SMFM of a fluorogenic probe reaction. The probe reaction is the photoelectrochemical oxidation of non-fluorescent amplex red (AR) to its highly fluorescent product, resorufin (*P*, see Figure 4.2a). Previous studies established that the AR oxidation reaction proceeds via an indirect mechanism involving $(\text{OH}^\bullet)_s$ instead of a direct mechanism involving $(h^+)_s$.¹¹⁸ The centroid of each product molecule is determined with 20-30 nm spatial resolution using super-resolution localization methods.¹¹⁹⁻¹²²

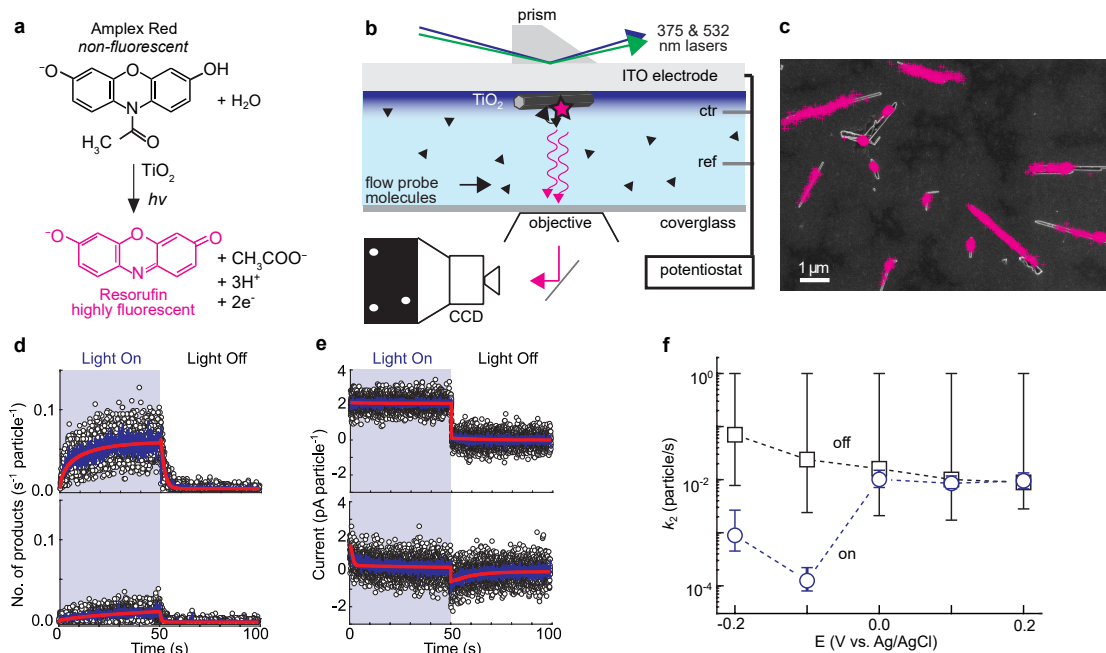


Figure 4.2: Reaction intermediate imaging via SMFM. (a) The oxidative N-deacetylation of non-fluorescent amplex red to highly fluorescent resorufin. (b) TIRF microscopy setup for SMFM. A 375 nm laser excites the TiO₂ nanoparticle photoanodes and a 532 nm laser excites the resorufin product molecules (pink star) that form on particle surfaces. (c) SEM image of TiO₂ nanorods on the ITO electrode. The pink dots represent individual product molecules. (d,e) Surface reaction intermediate and photoelectrochemical current dynamics versus the applied electrochemical potential. The black data points in (d) represent the number of product molecules generated on individual TiO₂ nanorods, averaged over 49 particles and 21 consecutive light on-off cycles at (top) 200 mV and (bottom) -200 mV versus the Ag/AgCl reference electrode. The black data points in (e) represent the current measured from ~1,000 TiO₂ particles. The blue lines in (d,e) represent a 5-point moving average of the data points and the thick solid red lines represent fits to a kinetic model. (f) Potential dependence of the rate constant for interfacial hole transfer to OH⁻ (k_1) under light on (blue circles) and light off (black squares) periods. Figure reproduced with permission from [114].

Figure 4.2b shows the experimental setup for single molecule reaction imaging via total internal reflection fluorescence (TIRF) microscopy. A dilute solution of TiO₂ nanorods was spin-cast on an indium tin oxide (ITO) electrode that served as the working electrode in a three-electrode electrochemical flow cell. In a typical experiment, a 375 nm laser excited approximately 1,000 TiO₂ nanorods in an on/off fashion to induce and cease (OH[•])_s production while a 532 nm laser continuously excited the fluorescent product molecules that formed on the nanorod surface. The product molecule fluorescence signal was collected through the microscope objective and imaged on an EM-CCD camera. In this excitation configuration, the photocurrent data represents the

ensemble-average behavior of 1,000 nanorods whereas the AR oxidation rate, which reports on the surface concentration of $(\text{OH}^\bullet)_s$, is quantified at the single nanorod-level with nanoscale spatial resolution.

Figure 4.2c shows the super-optical resolution imaging results from the reaction imaging experiment, where all product molecule positions (pink dots) are overlaid onto the SEM image of the TiO_2 nanorod-coated ITO electrode. Product molecule formation occurs uniformly across some TiO_2 nanoparticle surfaces, as evidenced by evenly distributed pink dots over the entire nanorod. On other TiO_2 nanorods, product molecules localize to nanoscale hot spots. The reactivity hot spots could be due to catalytically active surface structural defects¹²³ (oxygen vacancies^{87,124} or Ti_2O_3 units¹²⁵) or impurity atoms (e.g., Fe ¹²⁶). The hot spots are unlikely to arise from site-specific binding because controls showed that product molecules adsorb equivalently to all surface sites. The product molecule formation patterns likely vary among the nanorods because the concentration and spatial distribution of surface defects and/or impurities vary from particle to particle.

The Authors observed that the reaction intermediate dynamics followed different time scales in its temporal evolution from the photocurrent dynamics. Figure 4.2d shows representative single molecule reaction imaging results at two different applied potentials. The black data points represent the average number of P molecules versus time for 49 different nanorods during 21 chopped light illumination cycles. The blue line represents binned and averaged data to show the general trend. Upon illumination of the nanorods at $+0.2$ V vs Ag/AgCl , which was 0.8 V more positive than the flatband potential ($E_{fb} = -0.6$ V vs Ag/AgCl), the number of product molecules per individual nanorod increases slowly over a period of 20 s and apparently saturates at long times (Figure 4.2d, top). The product molecule formation dynamics report on the surface intermediate concentration. When the light is turned off, there is a slow decay in the product molecule formation rate. Conversely, there is an instantaneous rise and fall in the current (Figure 4.2e, top). At negative potentials (e.g., -200 mV or 0.4 V positive of E_{fb} in Figure 4.2d, bottom) the product formation and consumption dynamics show a similar trend but the total number of product molecules is significantly lower than the positive potential regime. The photocurrent response shows distinct

dynamic behaviors (Figure 4.2e, bottom) that do not appear in the single molecule reaction dynamics. First, there is an initial anodic current spike upon illumination of the nanorods followed by a transient decay while the light remains on. Second, the steady state photocurrent magnitude at long illumination times decreases with more negative applied potentials. Third, a cathodic transient appears when the light is turned off. Thus, the surface reaction intermediate dynamics follow different times scales in its temporal evolution than the overall water oxidation rate dynamics.

The Authors developed a kinetic model to simulate the single molecule and photocurrent data over a range of applied potentials and under dark and light illumination conditions. Fitting the data (solid red lines in Figure 4.2d,e) yielded the rate constant for interfacial hole transfer to $(\text{OH}^-)_s$ (k_1 in Equation (4.1)). Figure 4.2f shows that k_1 decreases as E approaches E_{fb} (-0.6 V) under illumination but is potential-independent in the dark. Durrant and co-workers also reported that the reactivity of surface holes is likely different under light and dark conditions.¹²⁷ At positive potentials (e.g., 0.1 and 0.2 V), the differences in k_1 with or without illumination are small. One possible explanation for k_1 decreasing with increasingly negative potentials under illumination is that electrons in filled surface states are photo-excited to the conduction band. The photogenerated holes in the surface states could react with $(\text{OH}^-)_s$. The Authors discussed alternative explanations for the potential dependence of k_1 under dark and light illumination conditions as well as rate constant for additional elementary steps in the water oxidation reaction. Regardless of the exact origin of the potential dependence of k_1 under dark and light conditions, single-molecule reaction imaging quantified the time-evolution of a critical reaction intermediate in water photoelectrolysis. The super-resolution reaction imaging experiment revealed higher water oxidation intermediate production rates at local hot spots within the same side facets of single nanorods.

4.2.2 Surface Recombination Imaging

One major requirement for an efficient photoelectrochemical reaction is to separate and transport charge carriers to their respective contacts before charge carrier recombination occurs.¹²⁸ For nanoscale materials with high surface area-to-volume ratios, a major charge recombination path-

way is surface recombination.¹²⁹ In this process, majority carriers (electrons for n-type semiconductors) reach and react with holes or surface reaction intermediates instead of being transported away from the interface and collected in the external circuit. Here we describe recent advances in molecular imaging of surface recombination processes at the single nano-entity level.

In 2016, Sambur et al. used charge carrier-selective imaging to spatially resolve hole- and electron-induced reactions at single TiO₂ nanorods.¹²⁶ For these n-type TiO₂ photoanodes, the electron-induced reactions represent majority carrier surface recombination reactions (Steps (7) and (9) in Figure 4.1a). The Authors used a similar electrochemical flow cell and TIRF microscopy setup as shown in Figure 4.2b, with two important distinctions. First, the 375 and 532 nm lasers continuously illuminated the sample to study photoelectrochemical activity under steady-state conditions. Second, the authors used two fluorogenic reactions to selectively probe electron- and hole-induced reactions. The probe reaction for holes was AR oxidation to the highly fluorescent product resorufin (*P*) via (OH[•])_s (as shown in figure 4.3a). The probe reaction for electrons was the irreversible reduction of weakly fluorescent resazurin (*Rz*) to the same product resorufin (Figure 4.3a). In a typical experiment, either 50 nM AR or Rz solution was flowed through the cell and a series of potential-dependent SMFM movies were recorded at 66 frames per second. Individual fluorescent molecule positions were localized in each frame with a spatial resolution of 30 nm. The authors localized thousands of product molecule positions to make super-optical resolution maps of hole and electron surface activity of single nanorods (figure 4.3b,c,e,f).

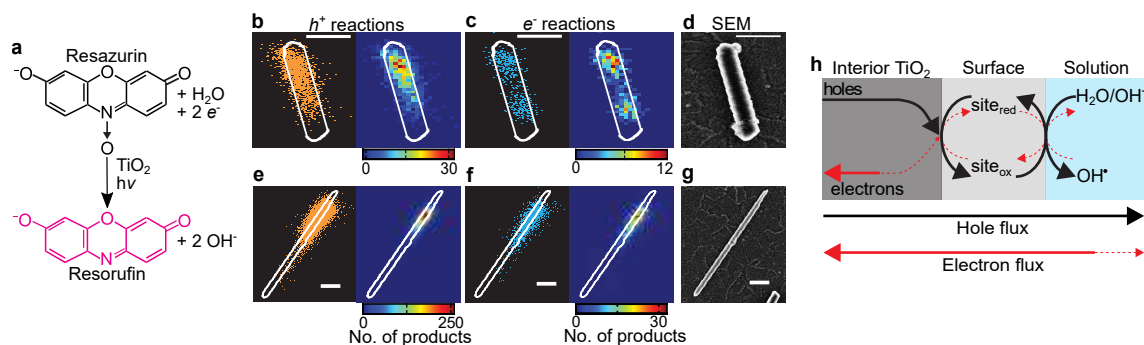


Figure 4.3: Surface recombination imaging via charge carrier-selective SMFM. **a)** the reductive N-deoxygenation of resazurin to resorufin probes photogenerated electrons. **(b)** Scatter plot (left) and two-dimensional histogram ($40 \times 40 \text{ nm}^2$ pixels; right) of all individual resorufin product molecules (orange dots) generated from hole-induced AR oxidation reactions at $E \geq -0.3 \text{ V}$ vs Ag/AgCl on a single TiO_2 nanorod. The solid white line represents the nanorod contour, determined using SEM (panel d). **(c)** Same as b), but for $E \leq -0.4 \text{ V}$ vs Ag/AgCl. The blue dots represent resorufin product molecules generated from electron-induced resazurin reduction reactions. **e-g)**, same as b-d) but for a nanorod with a single dominant hole and electron reaction hotspot. **h)** Schematic of “redox-cycling” of surface-active sites at anodic potentials (e.g., $E > 0.5 \text{ V}$ vs E_{fb}). All scale bars are 400 nm. Reprinted with permission from Springer Nature: Nature, [¹²⁶], © 2016.

Super-resolution imaging revealed that electrons and holes prefer to reach and react at the same surface sites on these TiO_2 nanorods. For example, Figure 4.3b-d shows correlated hole-induced and electron-induced activity at the top portion of a single nanorod. Figure 4.3e-g shows similar behavior for a second nanorod. Approximately 68% of the nanorods exhibited this localized activity. These intra-particle reactivity behaviors are hidden in ensemble-level methods. The authors hypothesized that the co-localized hole and electron hot-spots could be due to transition metal impurities or surface structural defects. For example, Fe impurities appeared in ex situ elemental analyses of the nanorod sample. Fe-doping has been shown to improve both the oxidation and reduction rates of TiO_2 nanoparticle photocatalysts,¹³⁰ which could account for the effects in Figure 4.3b,c,e,f. Interestingly, the authors detected electron-induced activity at significantly anodic potentials ($E > 0.5 \text{ V}$ vs. E_{fb}) where the average photocurrent per nanorod is 0.02 nA or 108 holes s^{-1} . SMFM can detect the small fraction of photogenerated electrons that participate in surface recombination reactions.

To rationalize the dual oxidative-reductive activity, the authors proposed the “redox cycling” scheme in Figure 4.3h. The arrival of holes and electrons to the surface sites is dictated by the applied potential according to the Gärtner-Butler^{131,132} and Reichman¹³³ models, respectively (the details of the models are provided in the Supplementary Information of ref.¹²⁶). Under anodic potentials (i.e., $E - E_{fb} > 0.5$ V), the hole flux to the surface is high (depicted by the large black arrow) and surface sites accept holes (i.e., the sites get oxidized to site_{ox}). When the oxidized surface sites transfer holes to surface adsorbed hydroxide or AR molecules, the surface sites get reduced (site_{red}). Most electrons are transported away from the interface and are collected in the external circuit (solid red arrow). According to the Reichman model,¹³³ it is also possible that photogenerated majority carriers (electrons) diffuse to the surface (red dashed arrow, analogous to Step (7) in Figure 4.1a), reducing site_{ox} to generate site_{red} . The reduced surface site can get oxidized via electron transfer to surface acceptors such as OH^\bullet , H_2O_2 , or Rz (Step (9) in Figure 4.1a). While nanoscale atomic-level characterization tools may be necessary to reveal the exact origin of the correlated surface activity, the authors showed that sites responsible for water oxidation at anodic potentials ($E > 0.5$ V vs E_{fb}) are the same sites responsible for surface recombination at cathodic potentials.

4.2.3 Charge Transport Imaging

The following charge transport imaging section focuses on recent developments in using continuous reaction imaging to study charge transport processes in single semiconductor nano-entities. In a single nanoparticle photoelectrode, the efficiency of minority charge carrier transport from the interior to the surface is one critical factor that determines the overall photocurrent efficiency (Step (7) in Figure 4.1b). Here we discuss a SMFM approach that measures charge transport distances without permanently altering the surface structure, as is typically done in alternative approaches that use irreversible metal deposition to probe charge transport to nanoparticle surface facets.¹³⁴ It should be noted that scanning probe microscopy measurements have also been used to image charge transport process in thin film photoelectrodes.^{135,136}

In 2011, Tachikawa et al. developed a single-molecule reaction imaging method to measure charge transport distances and crystal-face dependent photocatalytic activity in single TiO_2 particles.¹³⁷ The authors chose to study an electron-selective fluorogenic probe reaction: the photocatalytic reduction of non-fluorescent 3,4-dinitrophenyl-BODIPY to highly fluorescent product 4-hydroxyamino-3-nitrophenyl-BODIPY. Figure 4.4a shows the general experimental setup, where square sheet-like anatase TiO_2 crystals were deposited on insulating substrates and focused light excitation excited a specific region of the crystal. Majority charge carriers (electrons) move from the particle interior to a surface facet where they react with the non-fluorescent probe molecules (schematically illustrated in Figure 4.4b and Step (4) in Figure 4.1b). The distance between the light excitation spot and the product molecule position represents the photogenerated electron transport distance. Detailed imaging and kinetic analysis of the fluorescence product distributions showed that the reaction sites for the probe molecules were the $\{101\}$ crystal facets instead of the $\{001\}$ facets with a higher surface energy (Figure 4.4c-d). In 2019, Wang et al. extended the approach in Figure 4.4a-b to identify highly active edge/corner sites on TiO_2 particles using AR and Rz probes.¹³⁸

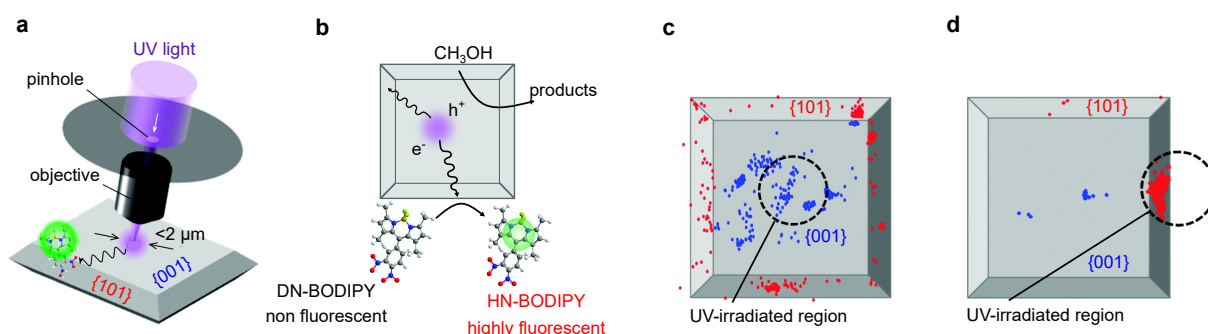


Figure 4.4: Charge carrier transport imaging via SMFM. **a)** Schematic of the experimental setup and imaging scheme. A focused light spot generates carriers in a localized region of a single anatase TiO_2 crystal. A photogenerated electron travels to a surface site and participates in a fluorogenic reaction that produces a highly fluorescent product (green circle). **b)** Schematic showing electron transport to a surface site, where it reacts with BN-BODIPY. Photogenerated holes oxidize methanol. **c)** Scatter plot of product molecule locations upon illuminating the $\{001\}$ facet. The product molecules detected on the $\{101\}$ and $\{001\}$ surfaces are indicated as red and blue dots, respectively. **d)** Same as c) but for illumination of the $\{101\}$ facet. Reprinted from reference [137].

The ability to resolve charge carrier transport distances via reaction imaging is limited by both the carrier generation spot size and the ability to localize reaction products. One strategy to localize carrier generation with tens of nanometer spatial is to use near-field optical excitation, as in near-field scanning optical microscopy (NSOM).¹³⁹ The technique requires that excitation light be focused through a probe tip that is positioned just above a nano-entity. NSOM techniques have been used to spatially resolve local photocurrent responses in organic solar cells¹⁴⁰ and investigate the effects of grain boundaries in polycrystalline solar cell materials.^{141,142} However, NSOM-based approaches have not been used to control carrier generation and spatially resolve transport and reactivity in nano-entity photoelectrodes.

4.3 Imaging Non-Fluorescent Photoelectrochemical Reactions

4.3.1 SMFM of non-fluorescent reactions

All the single molecule imaging experiments described above rely on fluorogenic reactions that produce fluorescent products. While fluorescence microscopy provides valuable information regarding underlying photoelectrochemical processes, most environmentally relevant photoelectrochemical processes do not produce fluorescent products or involve fluorescent intermediates. Thus, new single molecule imaging strategies are needed to directly image non-fluorogenic reactions such as hydrogen evolution or CO₂ reduction.

Mao et al. recently developed a competition-enabled imaging technique with super-resolution (COMPEITS) that interrogates non-fluorescent processes with nanometer spatial resolution.¹⁴³ The experimental approach is based on the competition between a non-fluorescent target reactant of interest and an auxiliary fluorogenic reactant for the same active sites on the same individual nanoparticles. While the approach can be applied to a wide range of systems, the authors applied COMPEITS to study photoelectrocatalysis on single BiVO₄ microcrystals. The target reaction of interest was hydroquinone oxidation and the auxiliary fluorogenic reaction was AR oxidation to resorufin (Figure 4.5a). Prior to imaging, the authors performed critical ensemble-level kinetic experiments that validated the two reactants compete for the same surface sites. SMFM mea-

measurements were performed in an epifluorescence illumination configuration using the experimental setup in Figure 4.2b. In this two-laser scheme, a blue laser excites the BiVO_4 particles and a green laser excites product molecules on the particle surface.

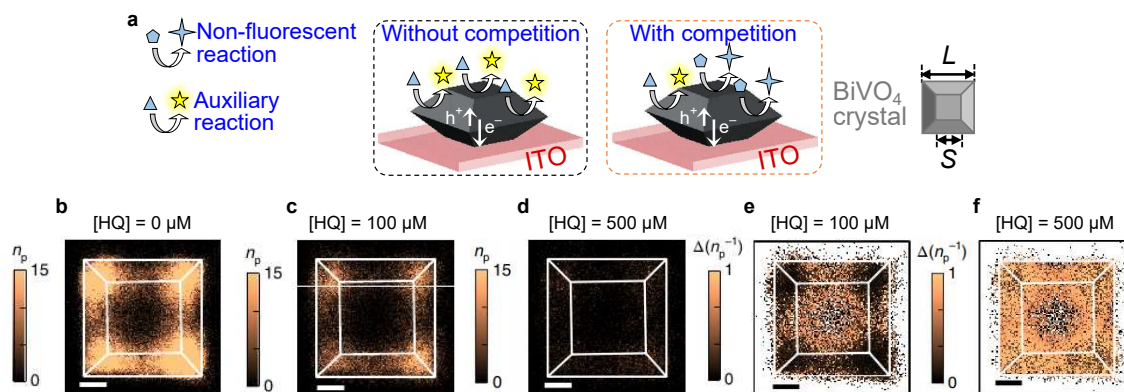


Figure 4.5: SMFM of non-fluorescent photoelectrochemical reactions. **a)** Experimental setup for COMPEITS imaging based on competition between two reactions. L and S parameters define the shape parameter ζ ($\zeta = S/L$). **b)** 2D histogram of AR oxidation events over 22.5 minutes for $[\text{AR}] = 50 \text{ nM}$ and $[\text{HQ}] = 0 \mu\text{M}$. The white lines indicate the particle contour from SEM imaging. **c, d)** The same 2D histograms but with 100 and 500 μM HQ and $[\text{AR}] = 50 \text{ nM}$. n_p in b-d) is the number of product molecules detected. **e, f)** COMPEITS images corresponding to 100 and 500 μM HQ respectively. COMPEITS images highlight the locations where HQ binds and reacts at the nanoparticle surface. Δn_p^{-1} is the inverse of the change in the number of detected product molecules following HQ addition. All scale bars are 500 nm. Reprinted with permission from Springer Nature: Nature Chemistry, [143], © 2019

The first step in COMPEITS is to establish the location of the auxiliary fluorogenic reactions in the absence of the target reaction (HQ; without competition in Figure 4a). The authors performed SMFM measurements at $[\text{AR}] = 40 \text{ nM}$ and $[\text{HQ}] = 0 \text{ nM}$. The resorufin product molecules were localized with nanometer precision and the number of AR oxidation products (n_p) were used to quantify the AR oxidation rate (ν_{AR}). Figure 4.5b shows a super-resolution activity map of all resorufin product molecules produced by a single BiVO_4 nanoparticle. Bright areas in the image indicate regions of high activity. The next step of COMPEITS is to repeat the fluorescence microscopy imaging experiment in the presence of increasing $[\text{HQ}]$ (with competition in Figure 4.5a). n_p decreases with increasing amounts of HQ due to the competition for surface sites (Figure 4.5c,d). The direct difference images (that is, images of Δn_p) show the expected trend:

Δn_p becomes larger with higher [HQ] (not shown in Figure 4.5). Since Δn_p images do not scale linearly with the HQ adsorption equilibrium constant (K_{HQ}), the authors generated inverse images of Δn_p (Δn_p^{-1}), or COMPEITS images (Figure 4.5e,f), that are proportional to K_{HQ} . The brighter, more saturated pixels in the COMPEITS image represent more HQ binding events. The COMPEITS images are quantitatively related to K_{HQ} and therefore directly reflect the local HQ binding affinity.

The authors observed dramatic differences in local binding affinity between the different crystal facets. The basal (top) surface was found to be the preferred binding facet for HQ. However, the K_{HQ} for both facets depended on the shape of the particle. K_{HQ} for both facets increased as the particles transition from flat plates to truncated bipyramids. The authors hypothesize that the shape dependence arises due to the edges between facets. The amount of edge differs as the crystals transition from truncated bipyramids to flat plates. These structure/property relationships could only be revealed with single-entity-level measurements.

COMPEITS is a powerful method to reveal structure/activity relationships that could be used to optimize photocatalyst morphology for non-fluorescent photoelectrochemical reactions. However, the approach has some limitations. COMPEITS does not completely eliminate the need for a fluorescent reporter molecule and its ability to monitor dynamic processes is limited by the relatively long time required to carry out a COMPEITS experiment (tens of minutes).

4.3.2 Bright Field Optical Microscopy

The Sambur group has developed a non-fluorescence-based optical microscopy approach to spatially resolve photoelectrochemical reactions on individual transition metal dichalcogenide (TMD) nanoflake photoelectrodes (e.g., MoS₂ and MoSe₂). The principle of this widefield optical microscopy approach is that photo-generated products on the electrode surface absorb or scatter incident light, which manifests as an optical density change in bright field transmission images.

This approach was benchmarked using MoS₂|I⁻, I₂|Pt photoelectrochemical cells because (1) transition metal dichalcogenide (TMD) iodide cells are efficient liquid junction solar cells¹⁴⁴⁻¹⁴⁶

with >10% monochromatic power conversion efficiency and (2) ensemble-level measurements have shown that I_2 products accumulate on TMD surfaces and limit the photocurrent.¹⁴⁷ However, the relationship between the nanoflake structural heterogeneity and the photocurrent loss is unclear.

In a typical experiment, 2D semiconductor nanoflakes are mechanically exfoliated from bulk crystals and transferred to an ITO electrode that is assembled into the three-electrode electrochemical flow cell as shown in Figure 4.2a. Figure 5a shows a representative bright field optical transmission image of a single MoS_2 nanoflake on the ITO electrode. The nanoflake exhibits smooth basal planes and step edges on the top surface as well as perimeter edges on all sides. Prior to bright field transmission imaging of photoelectrochemical reactions, we survey the photocurrent response from the basal planes and edge sites using single nanoflake photoelectrochemical microscopy.¹⁴⁸ To do so, we raster a focused 532 nm laser spot (690 nm diameter spot size) across the nanoflake to locally generate charge carriers while a potentiostat measures the photoanodic current due to iodide oxidation ($2I^- + 2h^+ \rightarrow I_2$). This scanning light spot technique produces a photocurrent map as a function of laser illumination position (Figure 4.6b). For the MoS_2 nanoflake in Figure 4.6a-b, illumination of basal planes produces a small and uniform photocurrent response. However, the photocurrent response from perimeter edges strongly depends on the illuminated position. Some illuminated perimeter edges produce the highest photocurrents whereas other spots produce negligible photocurrent (bottom left edge in Figure 4.6b). One major issue that prevents us from understanding the origin of the different photocurrent responses from basal planes and perimeter edges is that the photocurrent maps do not indicate where minority carriers (holes) react at the nanoflake surface. Instead, the photoelectrochemical microscopy technique measures the total current from the entire nanoflake upon illuminating local regions within the object.

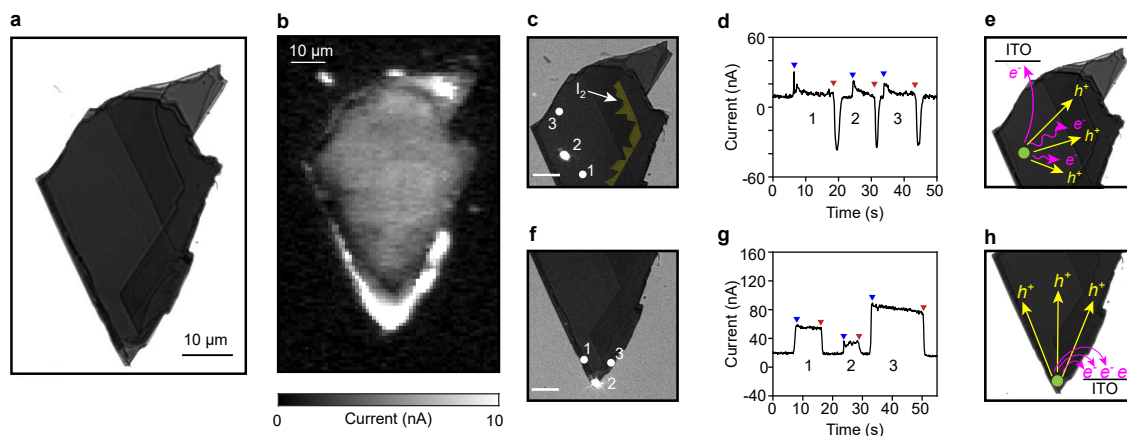


Figure 4.6: Charge transport imaging via bright field optical microscopy. **a)** Bright field optical transmission image of a MoS₂ nanoflake. **b)** Photocurrent map of the nanoflake in **a)**. A continuous wave 3 μ W 532 nm laser (690 nm spot diameter) excited the nanoflake in 1 μ m increments. The photocurrent was detected using a lock-in detection scheme as described in reference [148]. **c)** Cropped transmission image of the nanoflake in **a)**. The white circles labeled 1, 2, and 3 represent three excitation locations for chopped light photocurrent measurements. The false yellow color pixels indicate the surface iodine layer (indicated by white arrow). **d)** Current vs. time data from the three excitation locations in **c)**. The blue and red triangles indicate when the laser was turned on and off. **e)** Cartoon illustration of the minority carrier transport (black arrows) and iodine deposition process (dark red region at step edge) upon illuminating the basal plane in **c)**. **f-g)** Same as **c-d)**, but for the excitation spots indicated by white circles in **f)**. **h)** Cartoon illustration of the distribution of hole-induced iodide oxidation reactions across about half of the nanoflake (faint red shaded area) such that iodine deposition does not occur (see main text for details). The laser excitation power in **d,g)** was 20 μ W and a potentiostat measured the currents. Scale bars in **c,f)** are 10 μ m.

To image where photogenerated minority carriers react at the nanoflake surface, bright field transmission image movies were measured during photoelectrochemical measurements. The laser was positioned on either basal plane or perimeter edge locations using Figure 4.6a-b as a guide and simultaneously measured the photocurrent and transmission image stacks under chopped light illumination. When the laser illuminated the basal planes (spots 1, 2, 3 in Figure 4.6c), an instantaneous 30 nA photocurrent spike was observed, which decayed to a small 3 nA steady-state photocurrent (Figure 4.6d). At the same time, dark contrast pixels appeared at a step edge that was located 27 μ m away from the laser spot (indicated by false yellow colored pixels in Figure 4.6c for clarity). The dark contrast is due to an increase in optical density as a result of I₂ product accumulation at the step edge, as confirmed by in situ Raman micro-spectroscopy measurements¹⁴⁹ and literature.^{147,150} The products persist on the nanoflake surface during the entire illumination

period. The products disappear and a large cathodic spike appears upon interruption of the laser illumination (indicated by red triangle in Figure 4.6d).

The bright field transmission imaging technique revealed a correlation between charge carrier generation within basal planes, product accumulation at edge sites, and overall carrier collection efficiency (i.e. the photocurrent magnitude). I_2 products accumulate at TMD step edges because the local I_2 concentration at the electrode surface exceeds the solubility limit.^{147,151} The distance between the focused laser spot and the dark contrast pixels represents the minority carrier transport distance (Step 4 in Scheme 1b). According to electrochemical studies of iodide oxidation to iodine on Pt electrodes, the critical I_2 formation rate that would induce I_2 deposition on these MoS₂ nanoflakes is $10^8 I_2$ molecules $s^{-1} \mu m^{-2}$. For illumination spots 1, 2, and 3 in Figure 4.6b, this critical reaction rate could be achieved if 0.4% of photogenerated holes in the $0.37 \mu m^2$ illumination spots transport to, and react at equal rates along, the 44 μm -long step edge in Figure 4.6c. Since the average absorbed photon-to-current efficiency (APCE) at these locations was approximately 0.4%, this bright field imaging experiment revealed that approximately all photogenerated holes are transported to one particular step edge on the nanoflake (Figure 4.6e).

The origin of the high activity at the particular step edge in Figure 4.6c remains unclear. According to Chaparro et al., one possible explanation is that a highly efficient autocatalytic I^{3-} oxidation reaction takes place at edge sites ($Mo_{edge}^{VI} + 2I_3^-(ads) \rightarrow Mo_{edge}^{IV} + 3I_2$).¹⁵² The large I^{3-} anions preferentially chemisorb to Mo atoms at some surface active step edges, leading to an increased band-bending at the negatively charged surface and increased efficiency for interfacial hole transfer.¹⁵² This oxidation reaction competes with unproductive charge recombination processes^{153–155} (the anodic current decays under continuous illumination in Figure 4.6d). According to Peter et al., the photocurrent transient dynamics under chopped light illumination can be attributed to the following surface state recombination process.¹⁵⁶ Conduction band electrons can recombine with surface adsorbed $I_2(I_2(ads) + 2e^- \rightarrow 2I^-(aq))$, which accounts for the cathodic current decay after the illumination is interrupted.¹⁵² At steady-state, the rate of minority carrier flow into the surface states associated with adsorbed I^{3-} anions (Step (5) in Figure 4.1a) is larger than the rate

of majority carrier flow into the oxidized surface states associated with I_2 (Step (8) in Figure 4.1a), leading to a small 3 nA steady-state photocurrent in Figure 4.6d).

Previous ensemble-level¹⁴⁷ and photocurrent mapping studies of bulk n-type WSe_2 and $MoSe_2$ iodide cells that used 25-50 μm illumination spots^{152, 157} generally showed that direct illumination of smooth basal planes produced higher photocurrents than crystal regions with exposed edges. However, apparently defect-free crystal surfaces did not always produce high photocurrents.¹⁴⁶ The bright field transmission imaging results in Figure 4.6c-d revealed a hidden correlation between TMD surface morphology and carrier collection efficiency in iodide electrolytes that helps to explain why some smooth bulk TMD crystals exhibit poor solar energy conversion efficiencies.

Illuminating three perimeter edge regions at the bottom of the nanoflake (spots 1, 2, and 3 in Figure 4.6f) resulted in large and stable photocurrent responses (Figure 4.6g). No detectable optical density changes occurred in bright field transmission images even though the photocurrent magnitude was much higher than in Figure 4.6d. Moreover, we observed no cathodic current transient upon interruption of the illumination (Figure 4.6g). One explanation for this behavior is that the local iodine formation rate does not exceed the critical rate for iodine deposition. For the photocurrent magnitude in Figure 4.6g, the local iodine formation rate could remain below the critical rate if the minority carriers react at equal rates across a 700 μm^2 area of the nanoflake, or 56% of the total surface area (as illustrated in Figure 4.6h). This result also implies that minority carrier transport occurs over tens of microns, likely via a drift mechanism, because the minority carrier diffusion length in bulk TMDs is less than 5 μm .^{158, 159}

The bright field optical microscopy approach could be applied generally to (photo)electrochemical reactions that cause an absorption or refractive index change at the solid/liquid interface. For example, this technique could be used to study photo- or electro-deposition of metallic nanoparticle co-catalysts on single semiconductor nano-entity electrodes.¹⁶⁰ Metal nanoparticles absorb and scatter light as they grow or shrink at electrode surfaces. The size-dependent optical properties of nanoscale metal nanoparticles¹⁶¹ could be used to track the deposition kinetics at basal planes and

edge sites of 2D semiconductors. The deposition rates at the different surface structural features could inform on the transport and reactivity of electrons and holes. For example, Li et al. studied the spatial separation of electrons and holes on BiVO_4 nanoparticle catalysts using hole-induced and electron-induced deposition of PbO_2 and Pt, respectively.¹³⁴ In addition, bright field optical microscopy could be used to detect refractive index changes associated with bubble formation at electrode surfaces.¹⁶² For example, optical microscopy techniques such as surface plasmon resonance microscopy¹⁶³ and SMFM^{164,165} have been used to image nanobubble formation at single nanoparticle electrodes, which opens up the opportunity to study the fuel-forming hydrogen evolution reaction.

An interesting future direction for molecular reaction imaging via bright field microscopy is to study the relationship between charge transport anisotropy and surface morphology on the carrier collection efficiency of 2D nano-entity photoelectrodes. Space charge regions form in the direction parallel to the layers at step/perimeter edges as well as perpendicular to the layers at basal planes.^{154,166} Photogenerated carriers within the space charge region at step edges will preferentially drift toward the edge because the carrier mobility along the layers is much greater than perpendicular to the layers.¹⁶⁷⁻¹⁶⁹ This edge effect is expected to influence photogenerated carriers at high step edges because more carriers are produced in the space charge region at the step edge than at the top basal plane surface.¹⁷⁰⁻¹⁷² However, the fate of photogenerated minority carriers also depends on the edge site reactivity, or whether the edge acts as a recombination or “hot” site.¹⁷⁰ The optical charge transport and reactivity imaging methods discussed herein could play an important role in identifying and characterizing the structure and composition of different types of edges. Optical microscopy can be coupled in a one-to-one fashion with scanning Auger microscopy, atomic force microscopy, and scanning tunneling microscopy for high resolution composition and structural analyses.^{148,171} These findings could guide the development of efficient large area thin film nanoflake electrodes that are currently being pursued for photoelectrochemical energy conversion applications.¹⁷³

4.4 Summary and Outlook

Molecular reaction imaging approaches can be used to pin-point where photoelectrochemical reactions take place at nano-entity electrode surfaces. The redox chemistry of the probe reaction can be used to selectively study majority and minority carrier-induced reactions. The ability to spatially and temporally control light excitation enables direct investigations of the relationship between carrier generation and transport to active sites or recombination sites. The 20-30 nm spatial resolution of SMFM approaches is sufficient to resolve reaction intermediate dynamics within the same side facets of single nanoparticles, provided that the facet dimensions exceed about 100 nm.¹⁷⁴ A major advantage of the single particle-level approach for interrogating facet-dependent behavior is that particle-particle interfaces do not contribute to or complicate the interpretation of the surface reaction kinetics. The multitude of interfaces in nanoparticle film photoelectrodes complicates the quantitative interpretation of current-potential or current-time data for mechanistic information. Single molecule measurements also have the potential to uncover communication between active sites¹⁷⁵ as the surface reconstructs or reaction intermediates diffuse across the surface.

One opportunity to expand the reaction scope is to develop fluorogenic probe molecules¹⁷⁶ or fluorescence sensors¹⁷⁷ that target reaction intermediates or products in energy-relevant reactions, such as the H₂O₂ reaction intermediate in the water oxidation reaction¹⁷⁸ or intermediates in the CO₂ reduction reaction.¹⁷⁹ In addition, fluorescence detection of transition metal cations¹⁸⁰ could be used to probe photoelectrochemical corrosion of the semiconductor nano-entity. Aside from reactivity imaging, another opportunity is to develop molecular probes for surface characterization. Since surface defects can exhibit stronger molecule-surface interactions than the fully coordinated surface sites.¹⁸¹ It may be possible to design molecular probes with tailored functional groups to “label” surface structural defect or impurity sites.¹⁸² In this scenario, the surface labeling and imaging experiments may be performed before or after the single molecule reaction intermediate experiments. Correlated imaging experiments with multiple probes on the same nanoparticle have also been demonstrated.^{126, 183–185}

One disadvantage of SMFM is that not every reaction may be detected because product molecules could diffuse along or rapidly desorb from the electrode surface. Product diffusion among different surface sites could manifest as over-counting the total number of reactions as well as misrepresenting the spatial distribution of active sites. If products rapidly desorb from the electrode surface, then not all reactions are detected and counted accurately. Hence, the reported activities could underestimate the true activity of a single nano-entity. One strategy to overcome these detection issues is to perform SMFM of the fluorescent product molecules alone. In these control experiments, sub-nanomolar concentrations of product molecules are flowed through the cell and product adsorption and subsequent diffusion can be measured via single molecule tracking techniques. These data reveal the average residence time of single molecules and the extent to which product molecules diffuse along the surface.

While the optical microscopy approaches discussed herein uncover structure/property relationships that remain hidden in ensemble-level measurements, the methods do not reveal the atomic-level origins of high and low activity of nano-entity photoelectrodes. Strategies that link local composition and structure with photoelectrochemical properties have the potential to address the materials heterogeneity challenge. The next frontier in molecular reaction imaging is to correlate the high-throughput, low spatial-resolution reactivity information from optical methods with rich atomic-level structural information gleaned from state-of-the-art techniques such as atom probe tomography,^{186–188} electron^{189,190} and X-ray microscopy^{191,192} and spectroscopy.¹⁹³ Those high resolution characterization techniques provide atomic-level composition and structure of single nanoparticles. Hence, in our perspective, the major roadblock is not our ability to characterize atomic-level defects but rather our ability to correlate the presence and identify of defects and impurities with their functional properties (i.e., influence on activity or charge transport). Such advances demand that the optical microscopy experimental setup be compatible with electron or X-ray microscope instrument to enable sample characterization before and/or after optical imaging experiments. Super-resolution fluorescence microscopy experiments may be performed on TEM grids,¹⁹⁴ but such correlated experiments have not been performed under photoelectrochem-

ical conditions. If correlated single molecule reaction imaging and electron/X-ray microscopy experiments can be achieved, then it may be possible to characterize surface recombination sites or assess the catalytic activity of impurities,¹⁹⁵ atomically dispersed catalysts,¹⁹⁶ and nanoparticle co-catalysts.¹⁹⁷ A deeper understanding of how defects and impurities influence the photoelectrochemical response of nano-entities could lead to new interface and catalyst engineering strategies to control product selectivity and yield.¹⁹⁸

Chapter 5

Defect Mediated Energy Transfer Microscopy⁶

5.1 Intro

5.2 Experimental Methods

Single particle sample preparation and data collection are described in Section §2.4. The reconstructed trajectories that result from Section §2.4.3.3 are used for the remainder of the analysis.

5.2.1 Filtering

Because the single particle samples are heterogeneous (i.e. contains some particle aggregates, not all NCs have acceptors attached) each object (ROI) must be classified before further analysis can be done. Following are the steps taken to separate single particles and aggregates and to determine if a nanocrystal ROI also has an acceptor molecule present.

5.2.1.1 Separating single particles from clusters of particles

Because the ZnO nanocrystals are not capped with ligands during synthesis they tend to come together to form aggregates over time. These aggregates persist in the single particle sample after deposition of the NCs. Because single NCs are much smaller than the pixel size of the camera they should appear as point emitters in wide field fluorescence images while aggregates manifest as large objects with higher intensity. For simplicity, single particles are referred to as *singles* and aggregates are referred to as *clusters*. Figure 5.1a shows a fluorescence image of ZnO NCs under 355 nm excitation. The yellow arrows indicate two objects in each channel that which are much larger and brighter than the majority of the other objects in the image. These are clusters of particles. To separate singles and clusters the intensity of each ROI in the defect channel during 355 nm excitation was examined. Because single particles are roughly the same size and have a similar

⁶In preparation for submission

number of emissive defect sites they should have similar emission intensities. Clusters, on the other hand, will have an unknown number of emissive particles each producing photons, thus they will have higher intensity than singles and that intensity should be non-uniform between clusters. Figure 5.1b shows a histogram of all intensity values (frames) collected from all ROIs in the defect channel during 355 nm excitation. The large population at low intensity is created by single particle emission while the smaller populations at higher intensity are created by clusters. The histogram is then fit with a single component Gaussian function to establish the mean and standard deviation of the single particle population. A threshold is then set at three times the standard deviation above the mean. This threshold is then applied to each defect channel trajectory. Two examples are shown in Figure 5.1c and d. Figure 5.1c shows a trajectory from a single particle, the entire trajectory is below the threshold. Figure 5.1d shows a trajectory from a cluster of particles. The majority of this trajectory is above the threshold, causing this trajectory to be classified as a cluster. If more than 10% of the frames in the trajectory are above the threshold then the object is classified as a cluster. Any trajectory with at least 90% of its frames below the trajectory are classified as singles.

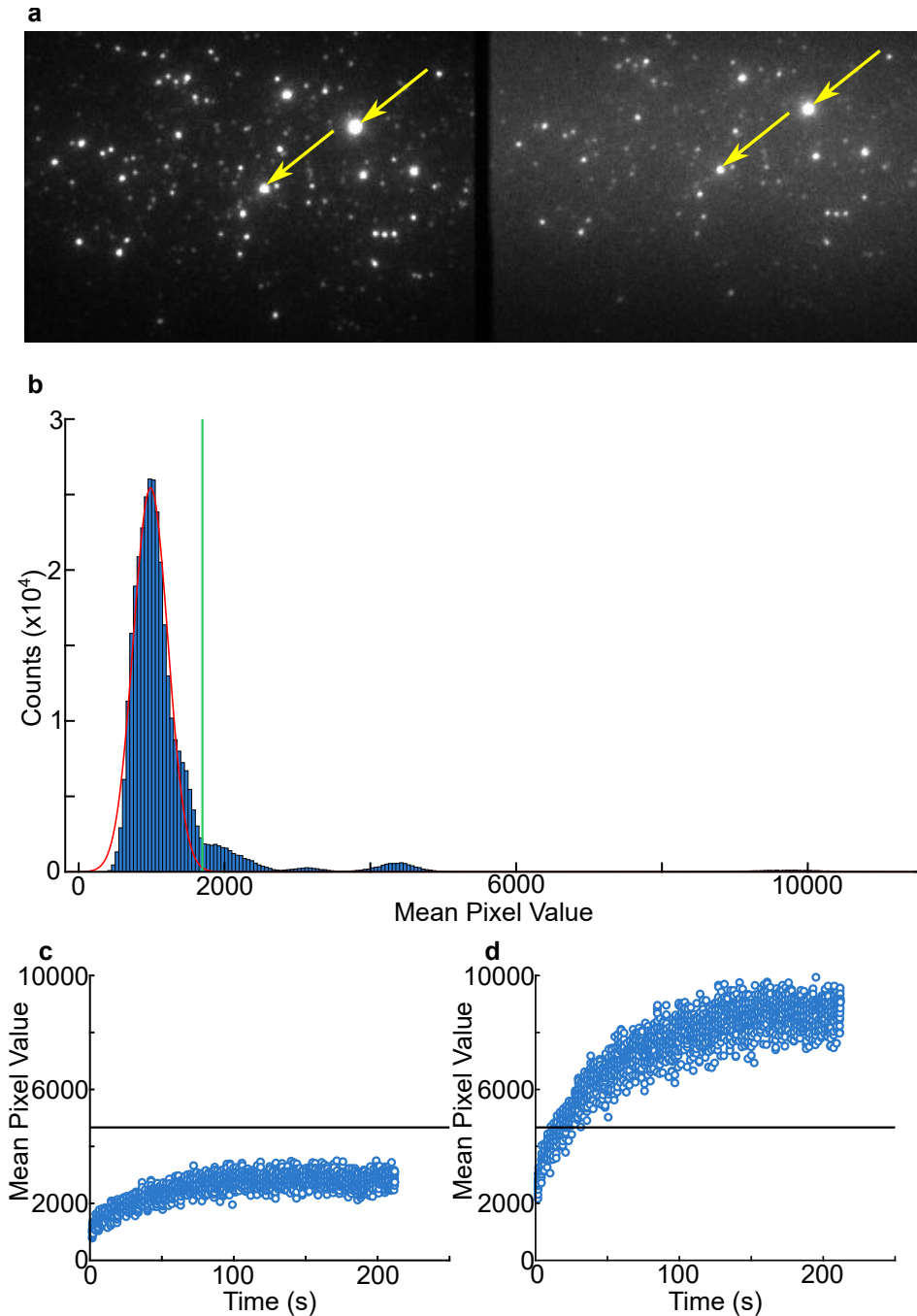


Figure 5.1: Separating singles and clusters. **a)** Wide field fluorescence image of ZnO nanocrystals. Image was created by averaging all the frames during the first 355 nm excitation pulse (36 frames). Yellow arrows point to objects that are considerably larger and brighter than the majority of other objects (clusters). **b)** Histogram of all intensity values (frames) for all ROIs in the defect channel during 355 nm excitation. The red curve is a Gaussian fit to the histogram bin values. The green line is a threshold set at three times the standard deviation above the mean of the Gaussian fit. **c)** Example trajectory from a single particle. The mean pixel value at each frame of the movie are shown as blue circles. The threshold set in b) is shown as a horizontal black line. **d)** The same as c) except for a cluster object.

5.2.1.2 Is A555 present inside the ROI?

Due to the random nature of the acceptor deposition, most nanocrystals do not have acceptor molecules nearby. This creates two populations of nanocrystals within the same sample, those that have acceptor molecules nearby and those that do not. Energy transfer requires that the donor and acceptor be relatively close together so the NC ROIs that have a A555 inside need to be separated from the ones that do not. To separate these populations, the presence of acceptor molecules is determined by examining the intensity trajectory taken from an NC ROI in the dye channel during 532 nm excitation. This excitation condition should only excite A555 molecules, and looking in the dye channel ensures that any emission from A555 molecules present in the NC ROIs is captured. Figure 5.2a depicts an example trajectories from an ROI which has at least one acceptor molecules present. Each point in the trajectory represents the average pixel value inside ROI during a single frame of a movie. The trajectory shows high intensity at early times due to the emission of acceptor molecules. After some time the intensity drops sharply due to the acceptor molecules photobleaching. Histograms of the trajectories are created to visualize the distribution of intensities within the trajectory (Figure 5.2b). These histograms are fit with Gaussian functions to establish the mean and standard deviation of the populations. A threshold is then set at four times the standard deviation above the mean of the lower (background) population. This is shown as a horizontal black line in Figure 5.2a,c. For trajectories and histograms that are not fit well by a single component Gaussian function ($R^2 < 0.7$) a two component Gaussian function is applied (Figure 5.2c,d). In this case the Gaussian function with the lower intensity center position is used to establish the threshold. This procedure is carried out for all ROIs that were created for nanocrystal objects, creating a threshold for each.

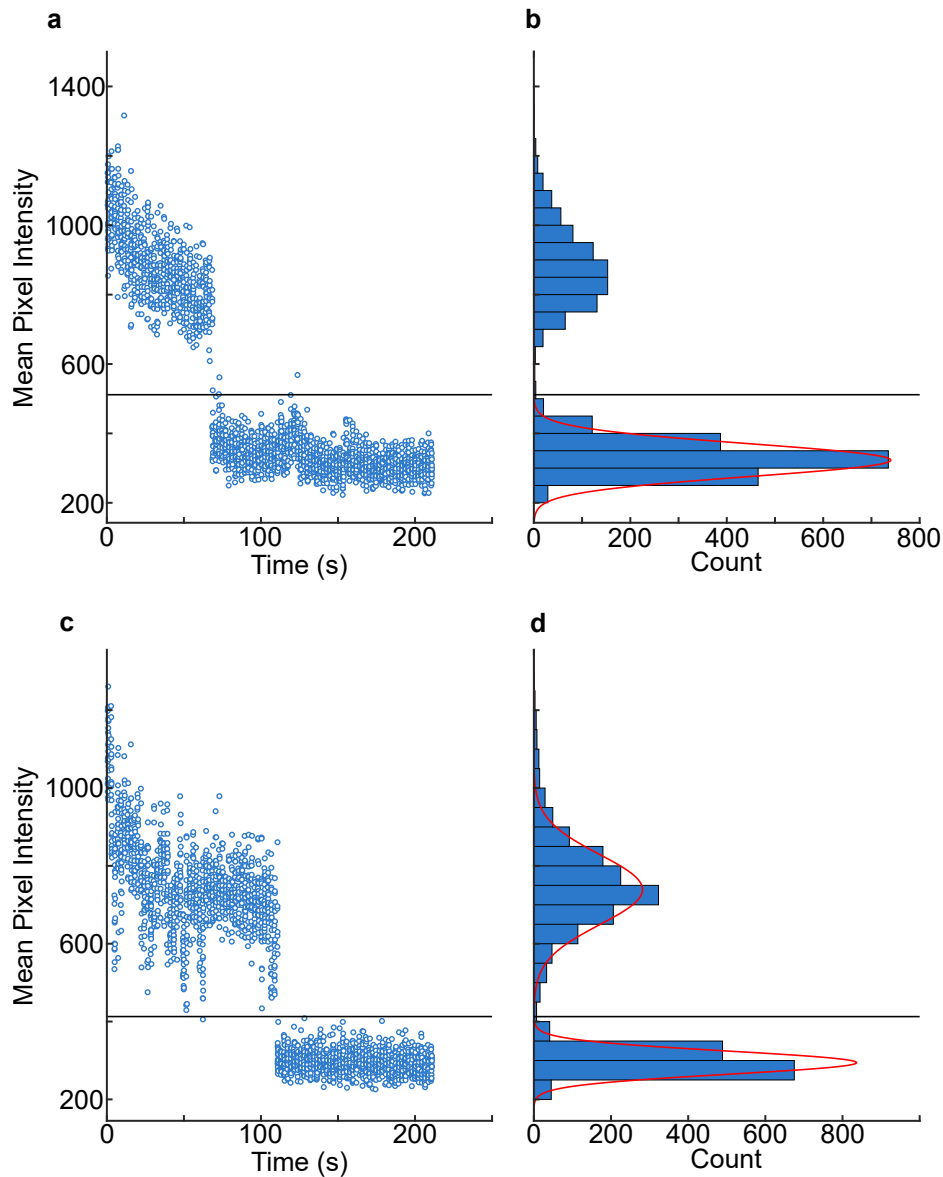


Figure 5.2: Is A555 present in the ROI? **a)** Intensity trajectory from a NC ROI in the dye channel. Each blue point is the average intensity of in the ROI during one frame of the movie. The horizontal black line is the threshold set using the histogram in **b)**. **b)** Histogram created from the points in **a)**. The histogram bins are fit with a Gaussian function (red line). The threshold is set at four times the standard deviation above the mean (black line). **c,d)** The same as **a,b)** but for a different ROI. The histogram of this trajectory was fit with a two component Gaussian function.

Using the thresholds established above, each ROI can be separated into one of three populations. The first is ROIs whose intensity trajectory never crosses the threshold. These ROIs represent nanocrystals that did not receive any acceptor molecules and can act as internal controls for ZnO

behavior. The second population are those ROIs which have at least one frame in their trajectory which is above the threshold. The final population has A555 emission present during the majority of the first 532 nm excitation pulse (i.e. greater than 60% of the frames during the first 532 nm excitation pulse are above the threshold). The separation of these population is done through a three step filtering process. This process is outlined graphically in Figure 5.3.

Because the first step does not consider when during the movie the intensity was above the threshold or for how long the intensity was above the threshold these ROIs are only considered candidate ROIs at this stage. The candidate ROIs may have acceptor molecules or may just have brief spikes in intensity caused by background signals. The second step considers only the first 532 nm excitation pulse because if an acceptor molecule is present in the ROI it has the highest chance of emitting photons during this period. The A555 molecules also do not blink so if a molecule is present present during the first 532 nm pulse it would most likely be emissive for at least the majority of the pulse before photobleaching. If the ROI merely has background noise causing random frames to have intensity above the threshold then it would be unlikely that the majority of the first 532 nm excitation period would be above the threshold.

ROIs that pass both of the above criteria are considered to have an acceptor molecule located in the same region. This does not necessarily mean that the molecule is bound to a nanocrystal, only that the two are relatively close together. Further analysis must be carried out to determine if the nanocrystal and acceptor molecules are interacting, see Section §5.3. The set of ROIs that pass both of these filters form a subset of the ROIs that will be examined further to determine if energy transfer from the NC defects to A555 molecules was observed during 355 nm excitation.

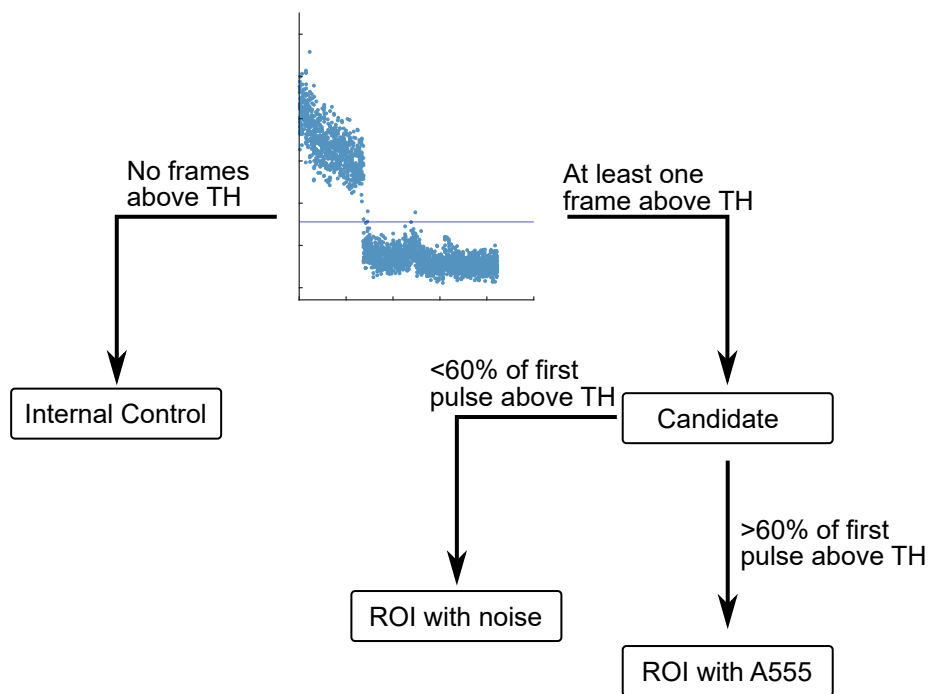


Figure 5.3: Flow chart outlining the filtering process used to determining if an A555 molecule is present in each ROI. The trajectory shown at the top is taken from Figure 5.2a and is used as an example.

5.3 Data Analysis

5.3.1 Background subtraction

Due to the high background caused by the quartz slide during ultra violet illumination the trajectories resulting from the process in Sections §2.4.3.3 need to be background subtracted before further analysis can happen. Using the background ROIs created in Section §2.4.3.2 a similar trajectory to the one shown in Section §2.4.3.3 can be produced for the background ROI. Figure 5.4a shows raw intensity trajectory from an NC ROI in the defect channel during 355 nm excitation as blue points. The corresponding background trajectory is shown as black points. Figure 5.4b shows the result of subtracting the black points in Figure 5.4a from the blue points.

The background subtracted NC trajectory shown in Figure 5.4b retains the slow rise over the first ~80 seconds of the movie from the raw trajectory. This indicates that rise feature is not wholly a result of the background quartz emission and that it must be caused by the ZnO.

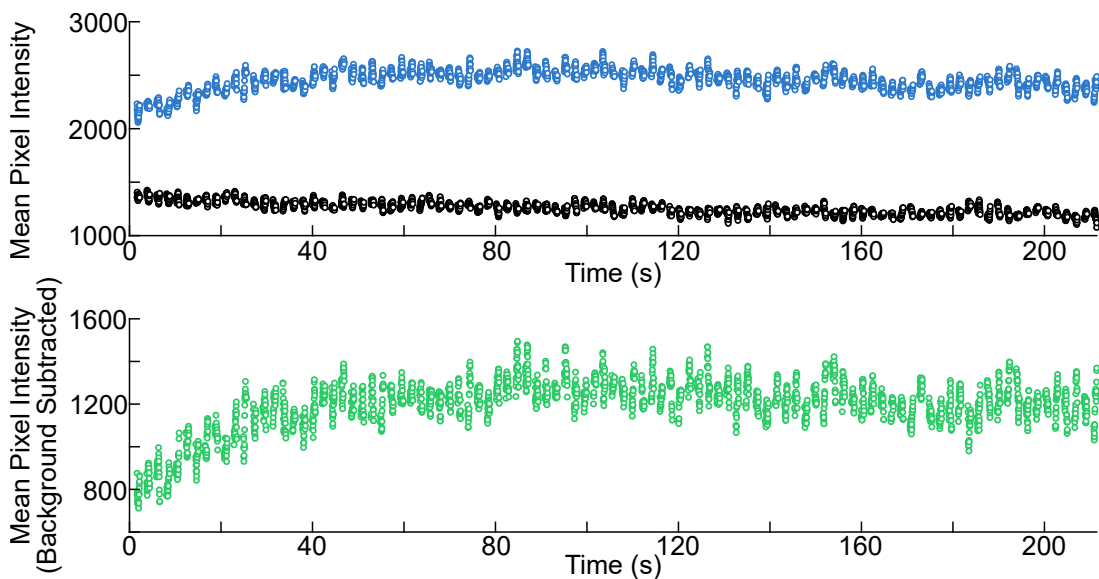


Figure 5.4: Background subtraction example. **a)** shows the raw intensity trajectory recorded from a NC ROI in the defect channel during 355 nm excitation (blue points) and the corresponding background trajectory recorded from the background ROI (black points). **b)** shows the result of subtracting the black points in **a)** from the blue points.

5.3.2 Trajectory Analysis

Following the procedures outlined in Sections §2.4.3.3 and 5.3.1 the trajectories are ready for initial inspection. Show in Figures 5.5, 5.6, and 5.7 are representative fluorescence images and trajectories from three single ZnO particles during an experiment with a mixture of NCs and A555 present on the slide. Figure 5.5a shows fluorescence images from the dye channel during 532 nm excitation. Here the green squares demarcate the corners of the ROI used to measure trajectories. Figure 5.5c shows a fluorescence image from dye channel acquired during 355 nm excitation. Again the green squares show the corners of the same ROI. The cyan squares show the corners of the background ROI. The trajectories in Figure 5.5b were recorded using the ROI in Figure 5.5a during 532 nm excitation. The trajectories were separated into the two detection channels, resulting in two trajectories. The black points in Figure 5.5b show the intensity inside the ROI in the dye channel and the blue points show the intensity inside the ROI in the defect channel. As expected the intensity in the defect channel (blue points) during 532 nm excitation reports only steady background signal because the 532 nm excitation only excites the A555 molecules and the

emission of A555 does not enter the defect channel. The dye channel (black) trajectory shows high intensity during the first 20 seconds of the movie, followed by a sharp intensity drop. This behavior is indicative of a dye molecule photobleaching, indicating that at least one A555 molecule was inside the ROI. This can be seen in the fluorescence image in a as a small bright object on the right side of the ROI. Because the image in a and the trajectory in b are created during 532 nm excitation this intensity can be attributed to A555 molecules and not ZnO defect emission as the NCs are not emissive under 532 nm excitation, as evidenced by the low intensity in the defect channel during this period (blue points in b, bottom right image of Figure 2.7). Applying the filtering steps outlined in Section §5.2.1.2 to the dye channel trajectory from Figure 5.5b classifies this ROI as an ROI that has A555 present, meaning that this ROI is a candidate for showing energy transfer behavior during 355 nm excitation.

The fluorescence image in Figure 5.5c shows a bright object inside the ROI during 355 nm excitation. This object is qualitatively in the same position as the bright object present in the ROI during 532 nm excitation (see Figure 5.5a), making this a promising candidate to exhibit energy transfer behavior. Interestingly, both the defect and dye channel trajectories in Figure 5.5d show a slow increase in intensity over the first 90 seconds of the movie followed by a period of steady intensity. There are no major intensity bursts or periods of increased intensity in the dye channel which would indicate some dye enhancement. There are also no periods of pronounced decreased intensity in the defect channel that would accompany quenching of the ZnO defect emission.

The slow intensity rise may be caused by the NC “burning off” molecules that are bound to the surface through photoredox processes. Because photoredox would provide a non-emissive pathway for excitons in the NC the intensity of the NC emission would be decreased until such a time that all the molecules capable of being oxidized by the NC are gone. ZnO NCs have been shown to be effective photocatalysts for the destruction of organic dyes.^{199–202}

If energy transfer were to occur within a NC ROI it would be expected that the dye channel trajectory during 355 nm excitation would show periods of increased intensity as the dye emission is enhanced by energy transfer. The intensity trajectory of the defect channel during the same times

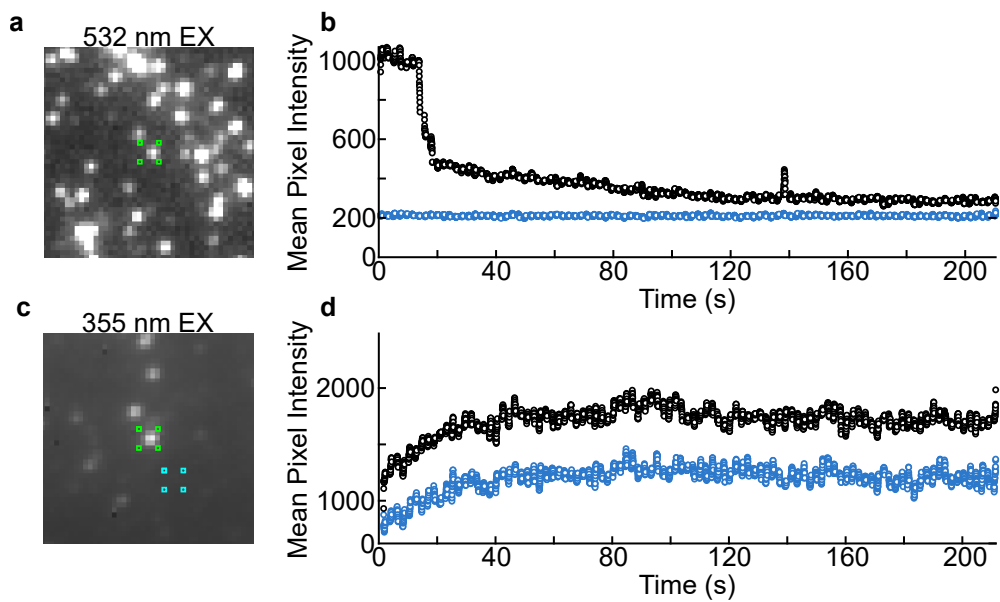


Figure 5.5: Reconstructed intensity trajectories taken from a NC ROI placed over a ZnO object that falls into the singles category and also passes both dye filtering steps from Section §5.2.1.2. **a)** Fluorescence image from the dye channel, acquired during 532 nm excitation, cropped to highlight the object of interest. The green squares in the image depict the corners of the ROI created for the object. **b)** Intensity trajectories acquired from the ROI in a) during 532 nm excitation. The red points show the intensity of the dye channel, the blue points show the intensity of the defect channel. **c)** Fluorescence image from the defect channel, acquired during 355 nm excitation, cropped to highlight the object of interest. The green squares in the image depict the corners of the ROI created for the object and the cyan squares show the corners of the background ROI used for background subtraction of the trajectories acquired during 355 nm excitation. **d)** Background subtracted intensity trajectories acquired from the green ROI in c) during 355 nm excitation. The red points show the intensity of the dye channel, the blue points show the intensity of the defect channel. A 15 point smooth has been applied to all trajectories to reduce noise.

would show periods of decreased intensity as the NC emission is quenched by energy transfer. These changes would be simultaneous and anti-correlated, similar to those seen in FRET literature.^{203–206} However, possibly due to the strong overlap of the donor and acceptor emissions within the dye channel, this behavior was not observed.

Seemingly overlapped NC-A555 pairs, like the one in Figure 5.5, are not the only types of objects that pass the filter described in Section §5.2.1.2. Because the ROI is relatively large compared to the size of the NCs it is very likely that A555 molecules will be present in the NC ROI but not actually be bound to or touching the NC. An example of this is shown in Figure 5.6. Figure 5.6a shows a fluorescence image acquired during 532 nm excitation, cropped to show a region of the dye channel. From this image it can be seen that there is an A555 molecule on the edge of the ROI.

The presence of this molecule is confirmed by the period of increased intensity near the beginning of the black trajectory shown in Figure 5.6b which shows characteristic photobleaching behavior at about 10 seconds. However, comparing the relative location of the A555 molecules within the ROI to the relative position of the ZnO NC shown in Figure 5.6c, it can be seen that the dye molecule is most likely not touching the NC. Because the A555 molecule is relatively far away from the NC it is unlikely that energy transfer could occur between the two objects. False positives like the one shown in Figure 5.6 are one downside to the filter methods outlined in section Section §5.2.1.2 and could be overcome by applying super resolution localization techniques.

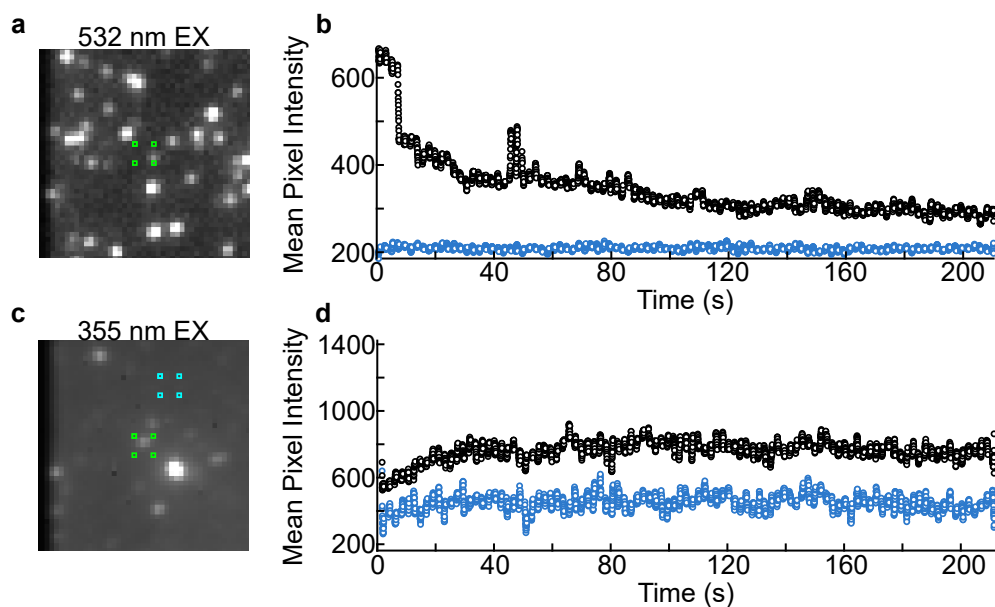


Figure 5.6: Reconstructed intensity trajectories taken from a NC ROI placed over a ZnO object that falls into the singles category and also passes both dye filtering steps from Section §5.2.1.2. **a)** Fluorescence image from the dye channel, acquired during 532 nm excitation, cropped to highlight the object of interest. The green squares in the image depict the corners of the ROI created for the object. **b)** Intensity trajectories acquired from the ROI in a) during 532 nm excitation. The red points show the intensity of the dye channel, the blue points show the intensity of the defect channel. **c)** Fluorescence image from the defect channel, acquired during 355 nm excitation, cropped to highlight the object of interest. The green squares in the image depict the corners of the ROI created for the object and the cyan squares show the corners of the background ROI. **d)** Intensity trajectories acquired from the ROI in c) during 355 nm excitation. The red points show the intensity of the dye channel, the blue points show the intensity of the defect channel. A 15 point smooth has been applied to all trajectories to reduce noise.

The same slowly increasing intensity is observed for both detection channels during 355 nm excitation for the NC shown in Figure 5.6d, similar to figure 5.5d. This indicates that the presence of the A555 molecule near the NC in figure 5.5d was not responsible for the shape of the trajectories because a similar shape is observed for the NC in Figure 5.6d which doesn't have an A555 molecule near by. This would point to other spectator molecules, either already present on the ZnO surfaces prior to deposition or molecules present in the immersol that deposit onto the ZnO during the experiment, being the cause of the slow intensity rise. ZnO NC defect emission is strongly dependent environment near the surface of the NC so it shouldn't be surprising that the NC emission is effected by something in the immersol oil or from another source.⁵⁷

And finally, the NC ROI used to create Figure 5.7 represents what will be referred to as an internal control NC. These are NCs that are present during experiments where A555 has been deposited onto the slide but the particular NC in question does not have *any* trace of A555 emission present, i.e., it does not pass the first step of the filter process in Section §5.2.1.2. These NCs act as internal controls because they have gone through all the same processing steps as the candidate NCs, they just do not have any A555 within the ROI. As shown in the florescence image in Figure 5.7a there is not emissive objects present inside the ROI during 532 nm excitation. The corresponding trajectories recorded during 532 nm excitation are shown in Figure 5.7b. Here the black points (dye channel) show a slow decrease in intensity over most of the movie. This could be due to out of focus background signals within the immersol. The defect channel (blue points) shows the expected steady background during 532 nm excitation.

The florescence image in Figure 5.7c shows an isolated NC inside the ROI. The corresponding dye channel trajectories recorded during 355 nm excitation are shown in Figure 5.7d. Once again the intensity of both channels shows a slow increase over the first 40 seconds of the movie. The fact that this NC also shows the slow intensity increase further confirms that the presence of the A555 molecule is not responsible for this behavior.

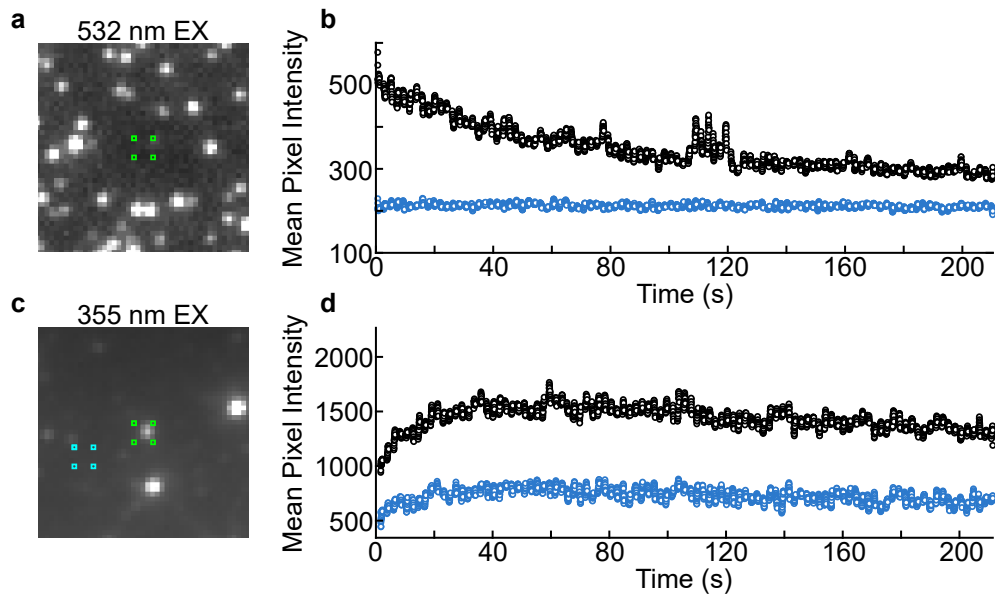


Figure 5.7: Reconstructed intensity trajectories taken from a NC ROI placed over a ZnO object that falls into the singles category but does not pass both dye filtering steps. **a)** Fluorescence image from the dye channel, acquired during 532 nm excitation, cropped to highlight the object of interest. The green squares in the image depict the corners of the ROI created for the object. **b)** Intensity trajectories acquired from the ROI in a) during 532 nm excitation. The red points show the intensity of the dye channel, the blue points show the intensity of the defect channel. **c)** Fluorescence image from the defect channel, acquired during 355 nm excitation, cropped to highlight the object of interest. The green squares in the image depict the corners of the ROI created for the object and the cyan squares show the corners of the background ROI. **d)** Intensity trajectories acquired from the ROI in c) during 355 nm excitation. The red points show the intensity of the dye channel, the blue points show the intensity of the defect channel. A 15 point smooth has been applied to all trajectories to reduce noise.

5.3.3 Ratio Analysis

Because the trajectory analysis was inconclusive at best, the ratio of the detection channels was calculated to better show any small changes in either the defect or dye channel. This ratio was calculated as $Ratio = \frac{I_{dye}}{I_{defect}}$. This was only done for the trajectories acquired during 355 nm excitation as it is during these periods of time that energy transfer could occur. Essentially, the black traces from Figures 5.5d, 5.6d, and 5.7d were divided by the corresponding blue traces. Because energy transfer should manifest as a decrease in the defect channel intensity along with a simultaneous increase in the dye channel intensity, the ratio should magnify any energy transfer events as increasing I_{dye} or decreasing I_{defect} both result in an increase in the ratio.

Figure 5.8a, b, and c show representative channel ratio trajectories calculated from the trajectories in Figures 5.5d, 5.6d, and 5.7d, respectively. Of particular interest is the ratio trajectory in Figure 5.8a because this ratio corresponds to the ROI shown in Figure 5.5 which has the best chance of showing energy transfer behavior due to the relative proximity of the NC and A555.

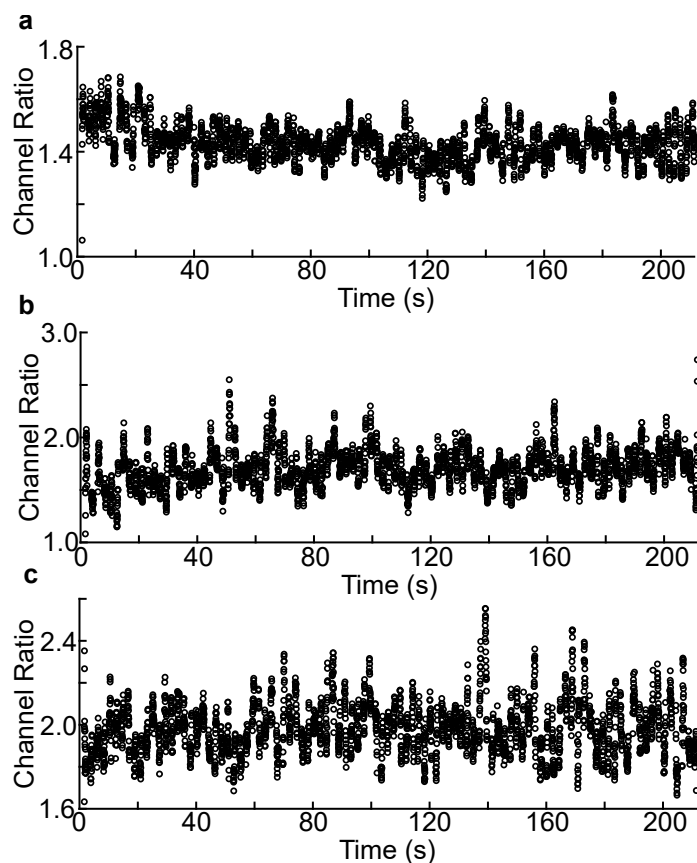


Figure 5.8: Representative channel ratios calculated from the trajectories in Figures 5.5, 5.6, and 5.7. Black points are the result of dividing the dye channel intensity by the defect channel intensity at every frame of the movie. A 15 point smooth has been applied to reduce noise.

Looking at Figure 5.8a the ratio appears to be, qualitatively, higher during the first ~30 seconds of the movie. This would seem to correspond with the same period of time when the A555 molecule was present inside the ROI (see Figure 5.5b). If this were true, it may indicate that energy transfer was occurring for this NC-A555 pair. No conclusions can be drawn from a single trajectory however. All NC-A555 pair ratios need to be examined to see if others show the same behavior.

So, to compare all the NC ROIs at once, the average of the ratio trajectories was calculated for the first three excitation pulses and the last three excitation pulses. The average during the first three pulses will report on the behavior within the ROI at early times (when A555 has the best chance of being present) and the average of the last three will show the behavior of the NC after the A555 molecule(s) have photobleached. These two average quantities were calculated for all ratio trajectories and the results are presented as histograms in Figure 5.9. Here the histograms have been separated by ROI classification. The top histogram shows the average ratio values at the beginning and the end of the trajectory for all objects that pass both steps of the filtering process from Section §5.2.1.2, including any false positives like the one shown in Figure 5.6. Compare this to the middle and lower histograms for internal control ROIs and all NC objects from the control movies, respectively. The histogram for NC-A555 pairs doesn't have any features to distinguish it from the NCs without A555. The top histogram in Figure 5.9 contains information from 94 NC-A555 pairs.

Unfortunately, the histograms Figure 5.9 do not show any more conclusive evidence of energy transfer than the ratios on their own or the raw trajectories. It would be expected that for trajectories which show evidence of energy transfer the channel ratio at the beginning of the movie would be higher than at the end of the movie due to the A555 molecule photobleaching during the movie. However, no obvious examples of this behavior are observed. The top histogram (NC-A555 pairs) in Figure 5.9 is qualitatively the same as the middle histogram (internal control ROIs). The bottom histogram of NC ROIs from the control movies shows that the ratio at the beginning and the end are both slightly higher than for the mixture movies. This is probably due to slight differences in the quartz slide used to build the sample. It seems that the system ZnO-A555 system is not ideal for single particle imaging. Changes to the data analysis methods may also be able to extract more information from the data presented in this chapter. Further discussion of some possible future directions for this project are presented in Chapter 6.

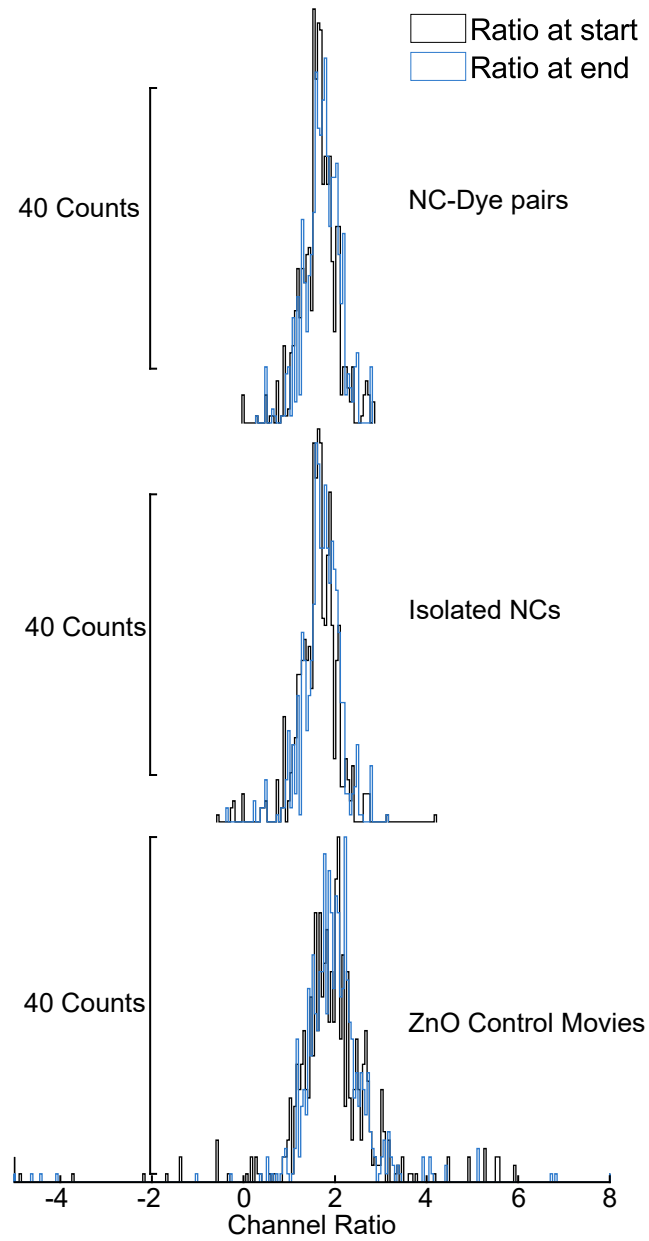


Figure 5.9: Histograms of average ratios. Top histogram contains the average ratios at the beginning (black) and end (blue) of the movie for 94 NC-A555 pairs. Middle and lower histogram contain the same information for internal control ROIs and all NC objects from the control movies, respectively.

Chapter 6

Summary/Outlook

6.1 Summary

Ensemble-level defect-mediated energy transfer was used to determine the relative position of emissive defect sites in ZnO NCs using two FRET based models. Both model predict that for the smallest NCs the energy transfer distance is larger than the NC diameter. This indicates that all defect positions can participate in energy transfer. Because all defect position can participate no conclusions can be drawn about the position of the emissive defects in the smallest NCs. For larger NCs, the calculated donor-acceptor distance was much smaller than the average NC diameter. Because the energy transfer distance was much smaller than the diameter of the NC (the RG model predicts <1 nm donor-acceptor distance for the largest NCs) it was concluded that at least the majority of emissive defects in the larger NCs participating in energy transfer must be at or near the surface. If the defects were buried at the center of the NC the predicted energy transfer distances from both models would require the dye molecules to be within the NC to participate. See Sections §3.3 and 3.4.

The same defect-mediated energy transfer system was then taken to the single-particle level to observe any heterogeneous population of particles. An imaging system was constructed that was capable of observing fluorescent emission from diffraction limited point sources (single NCs and dye molecules). Movies were acquired to observe the dynamics of the NC-dye system over time. Intensity trajectories of single objects were extracted from the movies to observe the behavior of individual objects. Inconclusive evidence of single-particle energy transfer was observed for NC-dye pairs that were determined to be very close together. See Section §5.3.

6.2 Outlook

Although the analysis procedure presented in Chapter 5 was inconclusive, a more detailed analysis may yet reveal some evidence of energy transfer. A first step could be to apply super resolution localization techniques to get a better handle on the relative locations of NCs and A555 molecules. Super resolution analysis also gives a better handle on the emission intensity of each object in the form of the Gaussian fit amplitude. From this analysis better filtering could be used which looks at the location of the NC and any acceptor molecules present in the same ROI and determines a distance between them. The filtering could then be based on the distance between donor and acceptor.

Slight modifications to the NC-A555 system presented here may yield better results. One of the most prominent failing of the ZnO NC system as described in this work is the tendency for the NCs to aggregate. It is unclear if what was classified as single particles by the filter process in Chapter 5 are actually single particles and not small clusters. Capping the NCs during synthesis could promote the colloidal stability of single NCs, which should translate to true single particles being deposited onto the slides for single particle experiments. Additionally, choosing a new acceptor molecule with an emission peak at longer wavelengths (700 + nm) would improve the imaging conditions and simplify the data analysis considerably. Currently, with A555, the emission peak of the acceptor directly overlaps with the emission of the ZnO NC defects. This forces the detection channels to both cover the broad defect emission, complicating the data analysis. An acceptor with emission beyond 700 nm would allow for the dye channel to have very little contribution from the NC defect emission. This would transform the single particle experiment into a more traditional FRET experiment where the dye channel is dark, except when energy transfer occurs.

Once the single particle experiment works for the small spherical particles discussed in this work application of this technique to larger microstructures is the ultimate goal of this project. Because the particles used in this study are so small relative to the localization precision, even of super resolution techniques (~30 nm), any location information would be of little use other than to

say if the defect sites are on the surface of the NCs or buried within the cores. With larger structures like rods, it would be possible to locate defect sites to a small area of the larger structure (assuming that the defect sites are not uniformly distributed). This location could then be correlated with reactivity using some of the fluorogenic probes discussed in Chapter 4 to inform on the effect of defect sites on electron and hole transfer processes.

Bibliography

- [1] Morasae Samadi, Mohammad Zirak, Amene Naseri, Malihe Kheirabadi, Mahdi Ebrahimi, and Alireza Z. Moshfegh. Design and tailoring of one-dimensional ZnO nanomaterials for photocatalytic degradation of organic dyes: a review. *Research on Chemical Intermediates*, January 2019.
- [2] Qiuping Zhang, Ming Xu, Biao You, Qin Zhang, Huan Yuan, and Kostya (Ken) Ostrikov. Oxygen Vacancy-Mediated ZnO Nanoparticle Photocatalyst for Degradation of Methylene Blue. *Applied Sciences*, 8(3):353, March 2018.
- [3] Yishu Jiang and Emily A. Weiss. Colloidal Quantum Dots as Photocatalysts for Triplet Excited State Reactions of Organic Molecules. *Journal of the American Chemical Society*, 142(36):15219–15229, 2020. PMID: 32810396.
- [4] Mohamad S. Kodaimati, Shichen Lian, George C. Schatz, and Emily A. Weiss. Energy transfer-enhanced photocatalytic reduction of protons within quantum dot light-harvesting-catalyst assemblies. *Proceedings of the National Academy of Sciences*, 115(33):8290–8295, 2018.
- [5] Yishu Jiang, Muwen Yang, Yue Wu, Rafael López-Arteaga, Cameron R. Rogers, and Emily A. Weiss. Chemo- and stereoselective intermolecular $[2\hat{A} + 2]$ photocycloaddition of conjugated dienes using colloidal nanocrystal photocatalysts. *Chem Catalysis*, 2021.
- [6] Zhengyi Zhang, Cameron R. Rogers, and Emily A. Weiss. Energy Transfer from CdS QDs to a Photogenerated Pd Complex Enhances the Rate and Selectivity of a Pd-Photocatalyzed Heck Reaction. *Journal of the American Chemical Society*, 142(1):495–501, January 2020.
- [7] Arunasish Layek, Paul C. Stanish, Vadim Chirmanov, and Pavle V. Radovanovic. Hybrid ZnO-Based Nanoconjugate for Efficient and Sustainable White Light Generation. *Chemistry of Materials*, 27(3):1021–1030, February 2015.

- [8] Vinod Kumar, H. C. Swart, Mukut Gohain, Vijay Kumar, S. Som, B. C. B. Bezuindenhoudt, and O. M. Ntwaeaborwa. Influence of ultrasonication times on the tunable colour emission of ZnO nanophosphors for lighting applications. *Ultrasonics Sonochemistry*, 21(4):1549–1556, July 2014.
- [9] Sonik Bhatia and Neha Verma. Photocatalytic activity of ZnO nanoparticles with optimization of defects. *Materials Research Bulletin*, 95:468–476, 2017.
- [10] K. Sudarshan, S.K. Sharma, Ruma Gupta, Santosh K. Gupta, F.N. Sayed, and P.K. Pujari. Role of surface defects in catalytic properties of CeO₂ nanoparticles towards oxygen reduction reaction. *Materials Chemistry and Physics*, 200:99–106, 2017.
- [11] Johannes Fichtner, Sebastian Watzele, Batyr Garlyyev, Regina M. Kluge, Felix Haimerl, Hany A. El-Sayed, Wei-Jin Li, Frédéric M. Maillard, Laetitia Dubau, Raphaël Chattot, Jan Michalicka, Jan M. Macak, Wu Wang, Di Wang, Thomas Gigl, Christoph Hugenschmidt, and Aliaksandr S. Bandarenka. Tailoring the Oxygen Reduction Activity of Pt Nanoparticles through Surface Defects: A Simple Top-Down Approach. *ACS Catalysis*, 10(5):3131–3142, 2020.
- [12] Jagriti Gupta, K. C. Barick, and D. Bahadur. Defect mediated photocatalytic activity in shape-controlled ZnO nanostructures. *Journal of Alloys and Compounds*, 509(23):6725–6730, June 2011.
- [13] Houman Yaghoubi, Zhi Li, Yao Chen, Huong T. Ngo, Venkat R. Bhethanabotla, Babu Joseph, Shengqian Ma, Rudy Schlaf, and Arash Takshi. Toward a Visible Light-Driven Photocatalyst: The Effect of Midgap-States-Induced Energy Gap of Undoped TiO₂ Nanoparticles. *ACS Catalysis*, 5(1):327–335, 2015.
- [14] Cedrik Meier, Stephan Lüttjohann, Vasyly G. Kravets, Hermann Nienhaus, Axel Lorke, Pascal Ifecho, Hartmut Wiggers, Christof Schulz, Marcus K. Kennedy, and F. Einar Kruis. Vi-

- brational and defect states in SnO_x nanoparticles. *Journal of Applied Physics*, 99(11):113108, 2006.
- [15] Arunasish Layek, Biswajit Manna, and Arindam Chowdhury. Carrier recombination dynamics through defect states of ZnO nanocrystals: From nanoparticles to nanorods. *Chemical Physics Letters*, 539-540:133–138, 2012.
- [16] Gang Xiong, U. Pal, and J. Garcia Serrano. Correlations among size, defects, and photoluminescence in ZnO nanoparticles. *Journal of Applied Physics*, 101(2):024317, 2007.
- [17] Candy C. Mercado, Fritz J. Knorr, Jeanne L. McHale, Shirin M. Usmani, Andrew S. Ichimura, and Laxmikant V. Saraf. Location of Hole and Electron Traps on Nanocrystalline Anatase TiO_2 . *The Journal of Physical Chemistry C*, 116(19):10796–10804, 2012.
- [18] Yi Jia, Kun Jiang, Haotian Wang, and Xiangdong Yao. The Role of Defect Sites in Nanomaterials for Electrocatalytic Energy Conversion. *Chem*, 5(6):1371–1397, 2019.
- [19] Th. Förster. 10th Spiers Memorial Lecture. Transfer mechanisms of electronic excitation. *Discussions of the Faraday Society*, 27(0):7–17, January 1959.
- [20] Th. Förster. Energiewanderung und Fluoreszenz. *Naturwissenschaften*, 33(6):166–175, June 1946.
- [21] Theodor Förster. Energy migration and fluorescence. *Journal of Biomedical Optics*, 17(1):011002, February 2012. Publisher: International Society for Optics and Photonics.
- [22] L. Stryer. Fluorescence Energy Transfer as a Spectroscopic Ruler. *Annual Review of Biochemistry*, 47(1):819–846, June 1978.
- [23] Cristobal G. dos Remedios and Pierre D. J. Moens. Fluorescence Resonance Energy Transfer Spectroscopy Is a Reliable Ruler for Measuring Structural Changes in Proteins: Dispelling the Problem of the Unknown Orientation Factor. *Journal of Structural Biology*, 115(2):175–185, September 1995.

- [24] L. Stryer and R. P. Haugland. Energy transfer: a spectroscopic ruler. *Proceedings of the National Academy of Sciences of the United States of America*, 58(2):719–726, August 1967.
- [25] Robert M. Clegg. Chapter 1 Förster resonance energy transfer – FRET what is it, why do it, and how it’s done. 33:1–57, January 2009.
- [26] Douglas K. Struck, Dick Hoekstra, and Richard E. Pagano. Use of resonance energy transfer to monitor membrane fusion. *Biochemistry*, 20(14):4093–4099, July 1981.
- [27] Kenneth Beardsley, Terence Tao, and Charles R. Cantor. Conformation of the anticodon loop of phenylalanine transfer ribonucleic acid. Effect of environment on the fluorescence of the Y base. *Biochemistry*, 9(18):3524–3532, September 1970.
- [28] Christoph Gohlke, Alastair I. H. Murchie, David M. Lilley, and Robert M. Clegg. Kinking of DNA and RNA helices by bulged nucleotides observed by fluorescence resonance energy transfer. *Proceeding of the National Academy of Sciences*, 1994.
- [29] Joseph R. Lakowicz, Ignacy Gryczynski, Wieslaw Wicz, Gabor Laczko, Franklyn C. Prendergast, and Michael L. Johnson. Conformational distributions of melittin in water / methanol mixtures from frequency-domain measurements of nonradiative energy transfer. *Biophysical Chemistry*, 36(2):99–115, July 1990.
- [30] Gary A. Beane, Anthony J. Morfa, Alison M. Funston, and Paul Mulvaney. Defect-Mediated Energy Transfer between ZnO Nanocrystals and a Conjugated Dye. *The Journal of Physical Chemistry C*, 116(5):3305–3310, February 2012.
- [31] Günther Cario. über Entstehung wahrer Lichtabsorption und scheinbare Koppelung von Quantensprünge. *Zeitschrift für Physik*, 10(1):185–199, 1922.
- [32] G. Cario and J. Franck. über Zerlegung von Wasserstoffmolekülen durch angeregte Quecksilberatome. *Zeitschrift für Physik*, 11(1):161–166, 1922.

- [33] Alexander Govorov, Pedro Ludwig Hernández Martínez, and Hilmi Volkan Demir. Short History of Energy Transfer Theory Before Förster, At The Time of Förster, and After Förster. In Alexander Govorov, Pedro Ludwig Hernández Martínez, and Hilmi Volkan Demir, editors, *Understanding and Modeling Förster-type Resonance Energy Transfer (FRET): Introduction to FRET, Vol. 1*, SpringerBriefs in Applied Sciences and Technology, pages 1–8. Springer, Singapore, 2016.
- [34] Alexander Govorov, Pedro Ludwig Hernández Martínez, and Hilmi Volkan Demir. Energy Transfer Review. In Alexander Govorov, Pedro Ludwig Hernández Martínez, and Hilmi Volkan Demir, editors, *Understanding and Modeling Förster-type Resonance Energy Transfer (FRET): Introduction to FRET, Vol. 1*, SpringerBriefs in Applied Sciences and Technology, pages 9–17. Springer, Singapore, 2016.
- [35] H. Hertz. Die Kräfte electrischer Schwingungen, behandelt nach der Maxwell’schen Theorie. *Annalen der Physik*, 272(1):1–22, 1889.
- [36] Th Förster. Zwischenmolekulare Energiewanderung und Fluoreszenz. *Annalen der Physik*, 437(1-2):55–75, 1948.
- [37] Suparna Sadhu and Amitava Patra. Donor–Acceptor Systems: Energy Transfer from CdS Quantum Dots/Rods to Nile Red Dye. *ChemPhysChem*, 9(14):2052–2058, 2008.
- [38] Burak Guzelturk, Pedro Ludwig Hernandez Martinez, Dewei Zhao, Xiao Wei Sun, and Hilmi Volkan Demir. Singlet and Triplet Exciton Harvesting in the Thin Films of Colloidal Quantum Dots Interfacing Phosphorescent Small Organic Molecules. *The Journal of Physical Chemistry C*, 118(45):25964–25969, November 2014.
- [39] Sixto Giménez, Andrey L. Rogach, Andrey A. Lutich, Dieter Gross, Andreas Poeschl, Andrei S. Susha, Ivan Mora-Seró, Teresa Lana-Villarreal, and Juan Bisquert. Energy transfer versus charge separation in hybrid systems of semiconductor quantum dots and Ru-

- dyes as potential co-sensitizers of TiO₂-based solar cells. *Journal of Applied Physics*, 110(1):014314, 2011.
- [40] Harri Härmä, Tero Soukka, Alexey Shavel, Nikolai Gaponik, and Horst Weller. Luminescent energy transfer between cadmium telluride nanoparticle and lanthanide(III) chelate in competitive bioaffinity assays of biotin and estradiol. *Analytica Chimica Acta*, 604(2):177–183, December 2007.
- [41] Daniel Geißler, Stina Linden, Konstanze Liermann, K. David Wegner, Loïc J. Charbonnière, and Niko Hildebrandt. Lanthanides and Quantum Dots as Förster Resonance Energy Transfer Agents for Diagnostics and Cellular Imaging. *Inorganic Chemistry*, 53(4):1824–1838, February 2014.
- [42] Emily J. McLaurin, Andrew B. Greytak, Mounqi G. Bawendi, and Daniel G. Nocera. Two-Photon Absorbing Nanocrystal Sensors for Ratiometric Detection of Oxygen. *Journal of the American Chemical Society*, 131(36):12994–13001, September 2009.
- [43] Jonathan Britton, Edith Antunes, and Tebello Nyokong. Fluorescence quenching and energy transfer in conjugates of quantum dots with zinc and indium tetraamino phthalocyanines. *Journal of Photochemistry and Photobiology A: Chemistry*, 210(1):1–7, February 2010.
- [44] Thilo Stöferle, Ullrich Scherf, and Rainer F. Mahrt. Energy Transfer in Hybrid Organic/Inorganic Nanocomposites. *Nano Letters*, 9(1):453–456, January 2009.
- [45] Paramita Saha Chowdhury, Pratik Sen, and Amitava Patra. Optical properties of CdS nanoparticles and the energy transfer from CdS nanoparticles to Rhodamine 6G. *Chemical Physics Letters*, 413(4):311–314, September 2005.
- [46] Suparna Sadhu, Masanori Tachiya, and Amitava Patra. A Stochastic Model for Energy Transfer from CdS Quantum Dots/Rods (Donors) to Nile Red Dye (Acceptors). *The Journal of Physical Chemistry C*, 113(45):19488–19492, November 2009.

- [47] M. Tachiya. Kinetics of quenching of luminescent probes in micellar systems. ii. *The Journal of Chemical Physics*, 76(1):340–348, 1982.
- [48] Carles Curutchet, Alberto Franceschetti, Alex Zunger, and Gregory D. Scholes. Examining Förster Energy Transfer for Semiconductor Nanocrystalline Quantum Dot Donors and Acceptors. *The Journal of Physical Chemistry C*, 112(35):13336–13341, September 2008.
- [49] Roi Baer and Eran Rabani. Theory of resonance energy transfer involving nanocrystals: The role of high multipoles. *The Journal of Chemical Physics*, 128(18):184710, 2008.
- [50] Ido Hadar, Shira Halivni, Na’ama Even-Dar, Adam Faust, and Uri Banin. Dimensionality Effects on Fluorescence Resonance Energy Transfer between Single Semiconductor Nanocrystals and Multiple Dye Acceptors. *The Journal of Physical Chemistry C*, 119(7):3849–3856, February 2015.
- [51] Shira Halivni, Amit Sitt, Ido Hadar, and Uri Banin. Effect of Nanoparticle Dimensionality on Fluorescence Resonance Energy Transfer in Nanoparticle-Dye Conjugated Systems. *ACS Nano*, 6(3):2758–2765, March 2012.
- [52] Amit Sitt, Na’ama Even-Dar, Shira Halivni, Adam Faust, Lior Yedidya, and Uri Banin. Analysis of Shape and Dimensionality Effects on Fluorescence Resonance Energy Transfer from Nanocrystals to Multiple Acceptors. *The Journal of Physical Chemistry C*, 117(43):22186–22197, October 2013.
- [53] Anderson Janotti and Chris G. Van de Walle. Native point defects in ZnO. *Physical Review B*, 76(16):165202, October 2007.
- [54] J. L. Lyons, J. B. Varley, D. Steiauf, A. Janotti, and C. G. Van de Walle. First-principles characterization of native-defect-related optical transitions in ZnO. *Journal of Applied Physics*, 122(3):035704, July 2017.

- [55] A. van Dijken, E. A. Meulenkaamp, D. Vanmaekelbergh, and A. Meijerink. Identification of the transition responsible for the visible emission in ZnO using quantum size effects. *Journal of Luminescence*, 90(3):123–128, August 2000.
- [56] Addy van Dijken, Eric A. Meulenkaamp, Daniël Vanmaekelbergh, and Andries Meijerink. The Kinetics of the Radiative and Nonradiative Processes in Nanocrystalline ZnO Particles upon Photoexcitation. *The Journal of Physical Chemistry B*, 104(8):1715–1723, March 2000.
- [57] Addy van Dijken, Eric A. Meulenkaamp, Daniël Vanmaekelbergh, and Andries Meijerink. Influence of Adsorbed Oxygen on the Emission Properties of Nanocrystalline ZnO Particles. *The Journal of Physical Chemistry B*, 104(18):4355–4360, May 2000.
- [58] Anderson Janotti and Chris G. Van de Walle. Oxygen vacancies in zno. *Applied Physics Letters*, 87(12):122102, 2005.
- [59] L. S. Vlasenko and G. D. Watkins. Optical detection of electron paramagnetic resonance in room-temperature electron-irradiated ZnO. *Physical Review B*, 71(12):125210, March 2005.
- [60] Annabel Wood, Michael Giersig, Michael Hilgendorff, Antonio Vilas-Campos, Luis M. Liz-Marzán, and Paul Mulvaney. Size Effects in ZnO: The Cluster to Quantum Dot Transition. *Australian Journal of Chemistry*, 56(10):1051–1057, 2003.
- [61] Joseph R. Lakowicz. *Principles of Fluorescence Spectroscopy*. Springer, Boston, MA, 3 edition, 2006.
- [62] Jan Valenta. Determination of absolute quantum yields of luminescing nanomaterials over a broad spectral range: from the integrating sphere theory to the correct methodology. *Nanoscience Methods*, 3(1):11–27, January 2014.

- [63] W. William Yu, Lianhua Qu, Wenzhuo Guo, and Xiaogang Peng. Experimental Determination of the Extinction Coefficient of CdTe, CdSe, and CdS Nanocrystals. *Chemistry of Materials*, 15(14):2854–2860, July 2003.
- [64] Jörg Enderlein and Rainer Erdmann. Fast fitting of multi-exponential decay curves. *Optics Communications*, 134(1):371–378, 1997.
- [65] Thomas Pons, Igor L. Medintz, Xiang Wang, Douglas S. English, and Hedi Mattoussi. Solution-Phase Single Quantum Dot Fluorescence Resonance Energy Transfer. *Journal of the American Chemical Society*, 128(47):15324–15331, November 2006.
- [66] Preston T. Snee, Christina M. Tyrakowski, Leah E. Page, Adela Isovici, and Ali M. Jawaaid. Quantifying Quantum Dots through Förster Resonant Energy Transfer. *The Journal of Physical Chemistry C*, 115(40):19578–19582, October 2011.
- [67] Aaron R. Clapp, Igor L. Medintz, J. Matthew Mauro, Brent R. Fisher, Mounqi G. Bawendi, and Hedi Mattoussi. Fluorescence Resonance Energy Transfer Between Quantum Dot Donors and Dye-Labeled Protein Acceptors. *Journal of the American Chemical Society*, 126(1):301–310, January 2004.
- [68] Cathy Y. Wong, Carles Curutchet, Sergei Tretiak, and Gregory D. Scholes. Ideal dipole approximation fails to predict electronic coupling and energy transfer between semiconducting single-wall carbon nanotubes. *The Journal of Chemical Physics*, 130(8):081104, 2009.
- [69] Joshua Schrier and Lin-Wang Wang. Shape Dependence of Resonant Energy Transfer between Semiconductor Nanocrystals. *The Journal of Physical Chemistry C*, 112(30):11158–11161, July 2008.
- [70] D. L. Andrews, C. Curutchet, and G. D. Scholes. Resonance energy transfer: Beyond the limits. *Laser & Photonics Reviews*, 5(1):114–123, 2011.

- [71] David Beljonne, Carles Curutchet, Gregory D. Scholes, and Robert J. Silbey. Beyond Förster Resonance Energy Transfer in Biological and Nanoscale Systems. *The Journal of Physical Chemistry B*, 113(19):6583–6599, May 2009.
- [72] Eric A. Meulenkaamp. Synthesis and Growth of ZnO Nanoparticles. *The Journal of Physical Chemistry B*, 102(29):5566–5572, July 1998.
- [73] Bharati Panigrahy, Mohammed Aslam, Devi Shanker Misra, Manoranjan Ghosh, and Dharendra Bahadur. Defect-related emissions and magnetization properties of zno nanorods. *Advanced Functional Materials*, 20(7):1161–1165, 2010.
- [74] P. A. Rodnyi and I. V. Khodyuk. Optical and luminescence properties of zinc oxide (Review). *Optics and Spectroscopy*, 111(5):776–785, November 2011.
- [75] A. B. Djurisić, Y. H. Leung, K. H. Tam, Y. F. Hsu, L. Ding, W. K. Ge, Y. C. Zhong, K. S. Wong, W. K. Chan, H. L. Tam, K. W. Cheah, W. M. Kwok, and D. L. Phillips. Defect emissions in ZnO nanostructures. *Nanotechnology*, 18(9):095702, January 2007.
- [76] Anthony J. Morfa, Brant C. Gibson, Matthias Karg, Timothy J. Karle, Andrew D. Greentree, Paul Mulvaney, and Snjezana Tomljenovic-Hanic. Single-photon emission and quantum characterization of zinc oxide defects. *Nano Letters*, 12(2):949–954, 2012. PMID: 22248087.
- [77] Ü. Özgür, Ya. I. Alivov, C. Liu, A. Teke, M. A. Reshchikov, S. Dogan, V. Avrutin, S.-J. Cho, and H. Morkoc. A comprehensive review of ZnO materials and devices. *Journal of Applied Physics*, 98(4):041301, 2005.
- [78] J. L. Lyons, A. Alkauskas, A. Janotti, and C. G. Van de Walle. Deep donor state of the copper acceptor as a source of green luminescence in zno. *Applied Physics Letters*, 111(4):042101, 2017.
- [79] C. X. Xu, X. W. Sun, X. H. Zhang, L. Ke, and S. J. Chua. Photoluminescent properties of copper-doped zinc oxide nanowires. *Nanotechnology*, 15(7):856–861, June 2004.

- [80] Y. S. Wang, P. John Thomas, and P. O'Brien. Optical properties of zno nanocrystals doped with cd, mg, mn, and fe ions. *The Journal of Physical Chemistry B*, 110(43):21412–21415, 2006. PMID: 17064087.
- [81] H. Gerischer. Charge transfer processes at semiconductor-electrolyte interfaces in connection with problems of catalysis. *Surface Science*, 18(1):97–122, November 1969.
- [82] A J Nozik. Photoelectrochemistry: Applications to Solar Energy Conversion. *Annual Review of Physical Chemistry*, 29(1):189–222, 1978.
- [83] Ming X. Tan, Paul E Laibinis, Sonbinh T. Nguyen, Janet M. Kesselman, Colby E. Stanton, and Nathan S. Lewis. *Principles and Applications of Semiconductor Photoelectrochemistry*, chapter 2, pages 21–144. John Wiley & Sons, Ltd, 1994.
- [84] K. Rajeshwar. Charge Transfer in Photoelectrochemical Devices via Interface States: Unified Model and Comparison with Experimental Data. *Journal of The Electrochemical Society*, 129(5):1003–1008, may 1982.
- [85] L. M. Abrantes and L. M. Peter. Transient photocurrents at passive iron electrodes. *Journal of Electroanalytical Chemistry and Interfacial Electrochemistry*, 150(1):593–601, July 1983.
- [86] P. Salvador. Kinetic approach to the photocurrent transients in water photoelectrolysis at n-titanium dioxide electrodes. 1. Analysis of the ratio of the instantaneous to steady-state photocurrent. *The Journal of Physical Chemistry*, 89(18):3863–3869, August 1985.
- [87] R. Schaub, P. Thostrup, N. Lopez, E. Lægsgaard, I. Stensgaard, J. K. Nørskov, and F. Besenbacher. Oxygen Vacancies as Active Sites for Water Dissociation on Rutile TiO₂. *Physical Review Letters*, 87(26):266104, December 2001.
- [88] Hans J. Queisser and Eugene E. Haller. Defects in Semiconductors: Some Fatal, Some Vital. *Science*, 281(5379):945–950, 1998.

- [89] Li Li, Paul A. Salvador, and Gregory S. Rohrer. Photocatalysts with internal electric fields. *Nanoscale*, 6(1):24–42, December 2013.
- [90] Juan Xu, Yiran Teng, and Fei Teng. Effect of Surface Defect States on Valence Band and Charge Separation and Transfer Efficiency. *Scientific Reports*, 6(1):32457, September 2016.
- [91] R. Memming and G. Schwandt. Potential and Charge Distribution at Semiconductor-electrolyte Interfaces. *Angewandte Chemie International Edition in English*, 6(10):851–861, 1967.
- [92] Peter Wuerfel and Uli Wuerfel. *Physics of Solar Cells. From Basic Principles to Advanced Concepts*. Wiley-VCH, Weinheim, Germany, 3 edition, 2016.
- [93] Tracy L. Thompson and John T. Yates. TiO₂-based Photocatalysis: Surface Defects, Oxygen and Charge Transfer. *Topics in Catalysis*, 35(3):197–210, July 2005.
- [94] J. Nowotny, C. C. Sorrell, L. R. Sheppard, and T Bak. Solar-hydrogen: Environmentally safe fuel for the future. *International Journal of Hydrogen Energy*, 30(5):521–544, April 2005.
- [95] J M D Coey, Kwanruthai Wongsaprom, J Alaria, and M Venkatesan. Charge-transfer ferromagnetism in oxide nanoparticles. *Journal of Physics D: Applied Physics*, 41(13):134012, jun 2008.
- [96] Fan Zhang. Grand challenges for nanoscience and nanotechnology in energy and health. *Frontiers in Chemistry*, 5:80, 2017.
- [97] Clemens Burda, Xiaobo Chen, Radha Narayanan, and Mostafa A. El-Sayed. Chemistry and Properties of Nanocrystals of Different Shapes. *Chemical Reviews*, 105(4):1025–1102, 2005. PMID: 15826010.
- [98] Arthur J. Nozik. Nanoscience and nanostructures for photovoltaics and solar fuels. *Nano Letters*, 10(8):2735–2741, 2010. PMID: 20597472.

- [99] Hao Ming Chen, Chih Kai Chen, Ru-Shi Liu, Lei Zhang, JiuJun Zhang, and David P. Wilkinson. Nano-architecture and material designs for water splitting photoelectrodes. *Chem. Soc. Rev.*, 41:5654–5671, 2012.
- [100] Xianluo Hu, Guisheng Li, and Jimmy C. Yu. Design, fabrication, and modification of nanostructured semiconductor materials for environmental and energy applications. *Langmuir*, 26(5):3031–3039, 2010. PMID: 19736984.
- [101] Peidong Yang, Ruoxue Yan, and Melissa Fardy. Semiconductor Nanowire: What’s Next? *Nano Letters*, 10(5):1529–1536, 2010. PMID: 20394412.
- [102] Yuwei Zhang, J. Matthew Lucas, Ping Song, Brandon Beberwyck, Qiang Fu, Weilin Xu, and A. Paul Alivisatos. Superresolution fluorescence mapping of single-nanoparticle catalysts reveals spatiotemporal variations in surface reactivity. *Proceedings of the National Academy of Sciences*, 112(29):8959–8964, 2015.
- [103] Takashi Tachikawa and Tetsuro Majima. Single-molecule, single-particle fluorescence imaging of TiO₂-based photocatalytic reactions. *Chem. Soc. Rev.*, 39:4802–4819, 2010.
- [104] Wei Wang. Imaging the chemical activity of single nanoparticles with optical microscopy. *Chem. Soc. Rev.*, 47:2485–2508, 2018.
- [105] Thorben Cordes and Suzanne A. Blum. Opportunities and challenges in single-molecule and single-particle fluorescence microscopy for mechanistic studies of chemical reactions. *Nature Chemistry*, 5(12):993–999, December 2013.
- [106] Rui Hao, Zhuoyu Peng, and Bo Zhang. Single-molecule fluorescence microscopy for probing the electrochemical interface. *ACS Omega*, 5(1):89–97, 2020.
- [107] Arunasish Layek, Jordi Van Loon, Maarten B. J. Roelffaers, and Alexey V. Kubarev. Correlated super-resolution fluorescence and electron microscopy reveals the catalytically active nanorods within individual H-ZSM-22 zeolite particles. *Catal. Sci. Technol.*, 9:4645–4650, 2019.

- [108] Daniel V. Esposito, Jason B. Baxter, Jimmy John, Nathan S. Lewis, Thomas P. Moffat, Tadashi Ogitsu, Glen D. O’Neil, Tuan Anh Pham, A. Alec Talin, Jesus M. Velazquez, and Brandon C. Wood. Methods of photoelectrode characterization with high spatial and temporal resolution. *Energy Environ. Sci.*, 8:2863–2885, 2015.
- [109] Paul Bazylewski, Sabastine Ezugwu, and Giovanni Fanchini. A Review of Three-Dimensional Scanning Near-Field Optical Microscopy (3D-SNOM) and Its Applications in Nanoscale Light Management. *Applied Sciences*, 7(10), 2017.
- [110] Alexander J. Cowan, Junwang Tang, Wenhua Leng, James R. Durrant, and David R. Klug. Water Splitting by Nanocrystalline TiO₂ in a Complete Photoelectrochemical Cell Exhibits Efficiencies Limited by Charge Recombination. *The Journal of Physical Chemistry C*, 114(9):4208–4214, 2010.
- [111] Omid Zandi and Thomas W. Hamann. Determination of photoelectrochemical water oxidation intermediates on haematite electrode surfaces using operando infrared spectroscopy. *Nature Chemistry*, 8(8):778–783, August 2016.
- [112] Camilo A. Mesa, Laia Francás, Ke R. Yang, Pablo Garrido-Barros, Ernest Pastor, Yimeng Ma, Andreas Kafizas, Timothy E. Rosser, Matthew T. Mayer, Erwin Reisner, Michael Grätzel, Victor S. Batista, and James R. Durrant. Multihole water oxidation catalysis on haematite photoanodes revealed by operando spectroelectrochemistry and DFT. *Nature Chemistry*, 12(1):82–89, January 2020.
- [113] David M. Herlihy, Matthias M. Waegele, Xihan Chen, C. D. Pemmaraju, David Prendergast, and Tanja Cuk. Detecting the oxyl radical of photocatalytic water oxidation at an n-SrTiO₃/aqueous interface through its subsurface vibration. *Nature Chemistry*, 8(6):549–555, June 2016.
- [114] Justin B. Sambur, Douglas P. Shepherd, Mahdi Hesari, Michael Van Erdewyk, Eric Choudhary, and Peng Chen. Correlated Single-Molecule Reaction Imaging and Photocurrent Mea-

- measurements Reveal Underlying Rate Processes in Photoelectrochemical Water Splitting. *Journal of The Electrochemical Society*, 166(5):H3286–H3293, 2019.
- [115] Yoshio Nosaka and Atsuko Y. Nosaka. Generation and detection of reactive oxygen species in photocatalysis. *Chemical Reviews*, 117(17):11302–11336, 2017. PMID: 28777548.
- [116] Andrew Mills, Christopher O'Rourke, and Keith Moore. Powder semiconductor photocatalysis in aqueous solution: An overview of kinetics-based reaction mechanisms. *Journal of Photochemistry and Photobiology A: Chemistry*, 310:66–105, 2015.
- [117] Ryuhei Nakamura and Yoshihiro Nakato. Molecular mechanism of water oxidation reaction at photo-irradiated TiO_2 and related metal oxide surfaces. *Solid State Phenomena*, 162:1–27, 7 2010.
- [118] Justin B. Sambur and Peng Chen. Distinguishing Direct and Indirect Photoelectrocatalytic Oxidation Mechanisms Using Quantitative Single-Molecule Reaction Imaging and Photocurrent Measurements. *The Journal of Physical Chemistry C*, 120(37):20668–20676, 2016.
- [119] Wenhui Wang, Junnan Gu, Ting He, Yangbin Shen, Shaobo Xi, Lei Tian, Feifei Li, Haoyuan Li, Liuming Yan, and Xiaochun Zhou. Optical super-resolution microscopy and its applications in nano-catalysis. *Nano Research*, 8(2):441–455, February 2015.
- [120] Yuying Gao, Wei Nie, Xiuli Wang, Fengtao Fan, and Can Li. Advanced space- and time-resolved techniques for photocatalyst studies. *Chem. Commun.*, 56:1007–1021, 2020.
- [121] Tao Chen, Bin Dong, Kuangcai Chen, Fei Zhao, Xiaodong Cheng, Changbei Ma, Seungah Lee, Peng Zhang, Seong Ho Kang, Ji Won Ha, Weilin Xu, and Ning Fang. Optical Super-Resolution Imaging of Surface Reactions. *Chemical Reviews*, 117(11):7510–7537, 2017. PMID: 28306243.

- [122] Michael J. Rust, Mark Bates, and Xiaowei Zhuang. Sub-diffraction-limit imaging by stochastic optical reconstruction microscopy (STORM). *Nature Methods*, 3(10):793–796, October 2006.
- [123] Gordon E. Brown, Victor E. Henrich, William H. Casey, David L. Clark, Carrick Eggleston, Andrew Felmy, D. Wayne Goodman, Michael Grätzel, Gary Maciel, Maureen I. McCarthy, Kenneth H. Nealson, Dimitri A. Sverjensky, Michael F. Toney, and John M. Zachara. Metal Oxide Surfaces and Their Interactions with Aqueous Solutions and Microbial Organisms. *Chemical Reviews*, 99(1):77–174, 1999. PMID: 11848981.
- [124] Ming Kong, Yuanzhi Li, Xiong Chen, Tingting Tian, Pengfei Fang, Feng Zheng, and Xiujian Zhao. Tuning the relative concentration ratio of bulk defects to surface defects in TiO_2 nanocrystals leads to high photocatalytic efficiency. *Journal of the American Chemical Society*, 133(41):16414–16417, 2011. PMID: 21923140.
- [125] YoonKeun Chae, JinWon Park, Shinsuke Mori, and Masaaki Suzuki. Correlation between Ti_2O_3 and oxygen absorption property of partially reduced TiO_2 TiO_{2-x} . *Journal of Industrial and Engineering Chemistry*, 18(5):1572–1576, 2012.
- [126] Justin B. Sambur, Tai-Yen Chen, Eric Choudhary, Guanqun Chen, Erin J. Nissen, Elayne M. Thomas, Ningmu Zou, and Peng Chen. Sub-particle reaction and photocurrent mapping to optimize catalyst-modified photoanodes. *Nature*, 530(7588):77–80, February 2016.
- [127] Andreas Kafizas, Yimeng Ma, Ernest Pastor, Stephanie R. Pendlebury, Camilo Mesa, Laia Francás, Florian Le Formal, Nuruzzaman Noor, Min Ling, Carlos Sotelo-Vazquez, Claire J. Carmalt, Ivan P. Parkin, and James R. Durrant. Water Oxidation Kinetics of Accumulated Holes on the Surface of a TiO_2 Photoanode: A Rate Law Analysis. *ACS Catalysis*, 7(7):4896–4903, 2017.
- [128] Michael Grätzel. Photoelectrochemical cells. *Nature*, 414(6861):338–344, November 2001.

- [129] G. Hodes, I. D. J. Howell, and L. M. Peter. Nanocrystalline Photoelectrochemical Cells: a New Concept in Photovoltaic Cells. *Journal of The Electrochemical Society*, 139(11):3136–3140, nov 1992.
- [130] Wonyong Choi, Andreas Termin, and Michael R. Hoffmann. The Role of Metal Ion Dopants in Quantum-Sized TiO₂: Correlation Between Photoreactivity and Charge Carrier Recombination Dynamics. *The Journal of Physical Chemistry*, 98(51):13669–13679, 1994.
- [131] Wolfgang W. Gärtner. Depletion-layer Photoeffects in Semiconductors. *Phys. Rev.*, 116:84–87, Oct 1959.
- [132] M. A. Butler. Photoelectrolysis and physical properties of the semiconducting electrode WO₂. *Journal of Applied Physics*, 48(5):1914–1920, 1977.
- [133] Joseph Reichman. Collection efficiency of low-mobility solar cells. *Applied Physics Letters*, 38(4):251–253, 1981.
- [134] Rengui Li, Fuxiang Zhang, Donge Wang, Jingxiu Yang, Mingrun Li, Jian Zhu, Xin Zhou, Hongxian Han, and Can Li. Spatial separation of photogenerated electrons and holes among {010} and {110} crystal facets of BiVO₄. *Nature Communications*, 4(1):1432, February 2013.
- [135] S.F. Alvarado, L. Rossi, P. Müller, and W. Rieß. Charge-carrier injection into cupc thin films: a scanning tunneling microscopy study. *Synthetic Metals*, 122(1):73–77, 2001. Proceedings of the E-MRS 2000 Spring Meeting, Symposium I.
- [136] Alberto Salleo, R. Joseph Kline, Dean M. DeLongchamp, and Michael L. Chabinyc. Microstructural Characterization and Charge Transport in Thin Films of Conjugated Polymers. *Advanced Materials*, 22(34):3812–3838, 2010.
- [137] Takashi Tachikawa, Soichiro Yamashita, and Tetsuro Majima. Evidence for crystal-face-dependent tio₂ photocatalysis from single-molecule imaging and kinetic analysis. *Journal of the American Chemical Society*, 133(18):7197–7204, 2011. PMID: 21495637.

- [138] Wei-Kang Wang, Jie-Jie Chen, Zai-Zhu Lou, Sooyeon Kim, Mamoru Fujitsuka, Han-Qing Yu, and Tetsuro Majima. Single-molecule and -particle probing crystal edge/corner as highly efficient photocatalytic sites on a single TiO₂ particle. *Proceedings of the National Academy of Sciences*, 116(38):18827–18833, 2019.
- [139] D. W. Pohl, W. Denk, and M. Lanz. Optical stethoscopy: Image recording with resolution $\lambda/20$. *Applied Physics Letters*, 44(7):651–653, 1984.
- [140] Christopher R. McNeill, Holger Frohne, John L. Holdsworth, John E. Furst, Bruce V. King, and Paul C. Dastoor. Direct photocurrent mapping of organic solar cells using a near-field scanning optical microscope. *Nano Letters*, 4(2):219–223, 2004.
- [141] Marina S. Leite, Maxim Abashin, Henri J. Lezec, Anthony G. Gianfrancesco, A. Alec Talin, and Nikolai B. Zhitenev. Mapping the Local Photoelectronic Properties of Polycrystalline Solar Cells Through High Resolution Laser-Beam-Induced Current Microscopy. *IEEE Journal of Photovoltaics*, 4(1):311–316, 2014.
- [142] Marina S. Leite, Maxim Abashin, Henri J. Lezec, Anthony Gianfrancesco, A. Alec Talin, and Nikolai B. Zhitenev. Nanoscale Imaging of Photocurrent and Efficiency in CdTe Solar Cells. *ACS Nano*, 8(11):11883–11890, 2014. PMID: 25317926.
- [143] Xianwen Mao, Chunming Liu, Mahdi Hesari, Ningmu Zou, and Peng Chen. Super-resolution imaging of non-fluorescent reactions via competition. *Nature Chemistry*, 11(8):687–694, August 2019.
- [144] G. Prasad and O. N. Srivastava. The high-efficiency (17.1%) WSe₂ photo-electrochemical solar cell. *Journal of Physics D: Applied Physics*, 21(6):1028–1030, June 1988.
- [145] R. Tenne and A. Wold. Passivation of recombination centers in n-WSe₂ yields high efficiency (>14%) photoelectrochemical cell. *Applied Physics Letters*, 47(7):707–709, 1985.

- [146] G. Kline, K. Kam, D. Canfield, and B.A. Parkinson. Efficient and stable photoelectrochemical cells constructed with WSe₂ and MoSe₂ photoanodes. *Solar Energy Materials*, 4(3):301–308, 1981.
- [147] H. Tributsch, T. Sakata, and T. Kawai. Photoinduced layer phenomenon caused by iodine formation in MoSe₂: electrolyte (iodide) junctions. *Electrochimica Acta*, 26(1):21–31, 1981.
- [148] Michael A. Todt, Allan E. Isenberg, Sanjini U. Nanayakkara, Elisa M. Miller, and Justin B. Sambur. Single-Nanoflake Photo-Electrochemistry Reveals Champion and Spectator Flakes in Exfoliated MoSe₂ Films. *The Journal of Physical Chemistry C*, 122(12):6539–6545, 2018.
- [149] Allan E. Isenberg, Michael A. Todt, Li Wang, and Justin B. Sambur. Role of Photogenerated Iodine on the Energy-Conversion Properties of MoSe₂ Nanoflake Liquid Junction Photovoltaics. *ACS Applied Materials & Interfaces*, 10(33):27780–27786, 2018. PMID: 30019887.
- [150] Gary Kline, Kam Keung Kam, Ruth Ziegler, and B.A. Parkinson. Further studies of the photoelectrochemical properties of the group VI transition metal dichalcogenides. *Solar Energy Materials*, 6(3):337–350, 1982.
- [151] S. Swathirajan and Stanley Bruckenstein. Ring-disk electrode studies of the open-circuit dissolution of iodine films formed during the anodic oxidation of iodide on platinum. *Journal of Electroanalytical Chemistry and Interfacial Electrochemistry*, 125(1):63–71, 1981.
- [152] A. M. Chaparro, P. Salvador, and L. M. Peter. The Role of Surface Defects in the Photooxidation of Iodide at n-MoSe₂: Evidence for a Local "Autocatalytic" Effect. *The Journal of Physical Chemistry*, 99(17):6677–6683, 1995.

- [153] T. E. Furtak, D. C. Canfield, and B. A. Parkinson. Scanning light-spot analysis of the carrier collection in liquid-junction solar energy converters. *Journal of Applied Physics*, 51(11):6018–6021, 1980.
- [154] H. J. Lewerenz, A. Heller, and F. J. DiSalvo. Relationship between surface morphology and solar conversion efficiency of tungsten diselenide photoanodes. *Journal of the American Chemical Society*, 102(6):1877–1880, 1980.
- [155] W. Kautek, H. Gerischer, and H. Tributsch. The role of surface orientation in the photoelectrochemical behavior of layer type d-band semiconductors. *Berichte der Bunsengesellschaft für physikalische Chemie*, 83(10):1000–1008, 1979.
- [156] L.M. Peter, J. Li, and R. Peat. Surface recombination at semiconductor electrodes: Part i. transient and steady-state photocurrents. *Journal of Electroanalytical Chemistry and Interfacial Electrochemistry*, 165(1):29–40, 1984.
- [157] Bruce A. Parkinson, Thomas E. Furtak, Duane Canfield, Kam-Keung Kam, and Gerald Kline. Evaluation and reduction of efficiency losses at tungsten diselenide photoanodes. *Faraday Discuss. Chem. Soc.*, 70:233–245, 1980.
- [158] A. Jakubowicz, D. Mahalu, M. Wolf, A. Wold, and R. Tenne. WSe₂: Optical and electrical properties as related to surface passivation of recombination centers. *Phys. Rev. B*, 40:2992–3000, Aug 1989.
- [159] Yipeng Zhao and Gang Ouyang. Thickness-dependent photoelectric properties of MoS₂/Si heterostructure solar cells. *Scientific Reports*, 9(1):17381, 2019.
- [160] Yikai Chen, Ke Sun, Heather Audesirk, Chengxiang Xiang, and Nathan S. Lewis. A quantitative analysis of the efficiency of solar-driven water-splitting device designs based on tandem photoabsorbers patterned with islands of metallic electrocatalysts. *Energy Environ. Sci.*, 8:1736–1747, 2015.

- [161] Min Hu, Carolina Novo, Alison Funston, Haining Wang, Hristina Staleva, Shengli Zou, Paul Mulvaney, Younan Xia, and Gregory V. Hartland. Dark-field microscopy studies of single metal nanoparticles: understanding the factors that influence the linewidth of the localized surface plasmon resonance. *J. Mater. Chem.*, 18:1949–1960, 2008.
- [162] Stefan Karpitschka, Erik Dietrich, James R. T. Seddon, Harold J. W. Zandvliet, Detlef Lohse, and Hans Riegler. Nonintrusive optical visualization of surface nanobubbles. *Phys. Rev. Lett.*, 109:066102, Aug 2012.
- [163] Yimin Fang, Zhimin Li, Yingyan Jiang, Xian Wang, Hong-Yuan Chen, Nongjian Tao, and Wei Wang. Intermittent photocatalytic activity of single cds nanoparticles. *Proceedings of the National Academy of Sciences*, 114(40):10566–10571, 2017.
- [164] Hua Su, Yimin Fang, Fangyuan Chen, and Wei Wang. Monitoring the dynamic photocatalytic activity of single CdS nanoparticles by lighting up H₂ nanobubbles with fluorescent dyes. *Chem. Sci.*, 9:1448–1453, 2018.
- [165] Rui Hao, Yunshan Fan, Marco D. Howard, Joshua C. Vaughan, and Bo Zhang. Imaging nanobubble nucleation and hydrogen spillover during electrocatalytic water splitting. *Proceedings of the National Academy of Sciences*, 115(23):5878–5883, 2018.
- [166] K. K. Kam and B. A. Parkinson. Detailed photocurrent spectroscopy of the semiconducting group vib transition metal dichalcogenides. *The Journal of Physical Chemistry*, 86(4):463–467, 1982.
- [167] J.A. Wilson and A.D. Yoffe. The transition metal dichalcogenides discussion and interpretation of the observed optical, electrical and structural properties. *Advances in Physics*, 18(73):193–335, 1969.
- [168] L. C. Upadhyayula, J. J. Loferski, A. Wold, W. Giriat, and R. Kershaw. Semiconducting Properties of Single Crystals of n- and p-Type Tungsten Diselenide (WSe₂). *Journal of Applied Physics*, 39(10):4736–4740, 1968.

- [169] E. Bucher. *Photovoltaic Properties of Solid State Junctions of Layered Semiconductors*, pages 1–81. Springer Netherlands, Dordrecht, 1992.
- [170] Jesus M. Velazquez, Jimmy John, Daniel V. Esposito, Adam Pieterick, Ragip Pala, Guofeng Sun, Xinghao Zhou, Zhuangqun Huang, Shane Ardo, Manuel P. Soriaga, Bruce S. Brun- schwig, and Nathan S. Lewis. A scanning probe investigation of the role of surface motifs in the behavior of p-wse₂ photocathodes. *Energy Environ. Sci.*, 9:164–175, 2016.
- [171] M. Velický, Mark A. Bissett, Colin R. Woods, Peter S. Toth, Thanasis Georgiou, Ian A. Kinloch, Kostya S. Novoselov, and Robert A. W. Dryfe. Photoelectrochemistry of Pristine Mono- and Few-Layer MoS₂. *Nano Letters*, 16(3):2023–2032, 2016. PMID: 26840510.
- [172] Joshua W. Hill and Caleb M. Hill. Directly Mapping Photoelectrochemical Behavior within Individual Transition Metal Dichalcogenide Nanosheets. *Nano Letters*, 19(8):5710–5716, 2019. PMID: 31287956.
- [173] Rebekah A. Wells, Hannah Johnson, Charles R. Lhermitte, Sachin Kinge, and Kevin Sivula. Roll-to-Roll Deposition of Semiconducting 2D Nanoflake Films of Transition Metal Dichalcogenides for Optoelectronic Applications. *ACS Applied Nano Materials*, 2(12):7705–7712, 2019.
- [174] Nisha May Andoy, Xiaochun Zhou, Eric Choudhary, Hao Shen, Guokun Liu, and Peng Chen. Single-Molecule Catalysis Mapping Quantifies Site-Specific Activity and Uncovers Radial Activity Gradient on Single 2D Nanocrystals. *Journal of the American Chemical Society*, 135(5):1845–1852, 2013. PMID: 23320465.
- [175] Ningmu Zou, Xiaochun Zhou, Guanqun Chen, Nisha May Andoy, Won Jung, Guokun Liu, and Peng Chen. Cooperative communication within and between single nanocatalysts. *Nature Chemistry*, 10(6):607–614, June 2018.

- [176] Carl P. LeBel, Harry Ischiropoulos, and Stephen C. Bondy. Evaluation of the probe 2',7'-dichlorofluorescein as an indicator of reactive oxygen species formation and oxidative stress. *Chemical Research in Toxicology*, 5(2):227–231, 1992. PMID: 1322737.
- [177] Jing Yuan, Yao Cen, Xiang-Juan Kong, Shuang Wu, Chen-Liwei Liu, Ru-Qin Yu, and Xia Chu. MnO₂-Nanosheet-Modified Upconversion Nanosystem for Sensitive Turn-On Fluorescence Detection of H₂O₂ and Glucose in Blood. *ACS Applied Materials & Interfaces*, 7(19):10548–10555, 2015. PMID: 25919577.
- [178] P. Salvador and F. Decker. The generation of hydrogen peroxide during water photoelectrolysis at n-titanium dioxide. *The Journal of Physical Chemistry*, 88(25):6116–6120, 1984.
- [179] Sheng Chu, Pengfei Ou, Pegah Ghamari, Srinivas Vanka, Baowen Zhou, Ishiang Shih, Jun Song, and Zetian Mi. Photoelectrochemical CO₂ Reduction into Syngas with the Metal/Oxide Interface. *Journal of the American Chemical Society*, 140(25):7869–7877, 2018. PMID: 29905471.
- [180] Maher A. Alodan and William H. Smyrl. Detection of localized corrosion of aluminum alloys using fluorescence microscopy. *Journal of The Electrochemical Society*, 145(5):1571–1577, may 1998.
- [181] Jan Haubrich, Efthimios Kaxiras, and Cynthia M. Friend. The Role of Surface and Sub-surface Point Defects for Chemical Model Studies on TiO₂: A First-Principles Theoretical Study of Formaldehyde Bonding on Rutile TiO₂(110). *Chemistry - A European Journal*, 17(16):4496–4506, 2011.
- [182] Rob Ameloot, Frederik Vermoortele, Johan Hofkens, Frans C. De Schryver, Dirk E. De Vos, and Maarten B. J. Roeloffs. Three-dimensional visualization of defects formed during the synthesis of metal-organic frameworks: A fluorescence microscopy study. *Angewandte Chemie International Edition*, 52(1):401–405, 2013.

- [183] Kyu Sung Han, Guokun Liu, Xiaochun Zhou, Rita E. Medina, and Peng Chen. How Does a Single Pt Nanocatalyst Behave in Two Different Reactions? A Single-Molecule Study. *Nano Letters*, 12(3):1253–1259, 2012. PMID: 22276804.
- [184] Gareth T. Whiting, Nikolaos Nikolopoulos, Ioannis Nikolopoulos, Abhishek Dutta Chowdhury, and Bert M. Weckhuysen. Visualizing pore architecture and molecular transport boundaries in catalyst bodies with fluorescent nanoprobes. *Nature Chemistry*, 11(1):23–31, 2019.
- [185] Meikun Shen, Tianben Ding, Steven T. Hartman, Fudong Wang, Christina Krucylak, Zheyu Wang, Che Tan, Bo Yin, Rohan Mishra, Matthew D. Lew, and Bryce Sadtler. Nanoscale Colocalization of Fluorogenic Probes Reveals the Role of Oxygen Vacancies in the Photocatalytic Activity of Tungsten Oxide Nanowires. *ACS Catalysis*, 10(3):2088–2099, 2020.
- [186] P.A.J. Bagot, T. Visart de Bocarmé, A. Cerezo, and G.D.W. Smith. 3D atom probe study of gas adsorption and reaction on alloy catalyst surfaces I: Instrumentation. *Surface Science*, 600(15):3028–3035, 2006.
- [187] Natalia Gilis, Luc Jacobs, Cédric Barroo, and Thierry Visart de Bocarmé. Surface Segregation in Au-Ag Alloys Investigated by Atom Probe Tomography. *Topics in Catalysis*, 61(14):1437–1448, 2018.
- [188] Jun Takahashi, Kazuto Kawakami, Yukiko Kobayashi, and Toshimi Tarui. The first direct observation of hydrogen trapping sites in TiC precipitation-hardening steel through atom probe tomography. *Scripta Materialia*, 63(3):261–264, 2010.
- [189] David C. Bell, Max Mankin, Robert W. Day, and Natasha Erdman. Successful Application of Low Voltage Electron Microscopy to Practical Materials Problems. *Ultramicroscopy*, 145:56–65, 2014. Low-Voltage Electron Microscopy.

- [190] Sharon Mitchell, Nina-Luisa Michels, Karsten Kunze, and Javier Pérez-Ramírez. Visualization of hierarchically structured zeolite bodies from macro to nano length scales. *Nature Chemistry*, 4(10):825–831, 2012.
- [191] C. Blanco-Roldán, C. Quirós, A. Sorrentino, A. Hierro-Rodríguez, L. M. Álvarez-Prado, R. Valcárcel, M. Duch, N. Torras, J. Esteve, J. I. Martín, M. Vélez, J. M. Alameda, E. Pereiro, and S. Ferrer. Nanoscale imaging of buried topological defects with quantitative X-ray magnetic microscopy. *Nature Communications*, 6(1):8196, 2015.
- [192] F. Devred, G. Reinhart, G.N. Iles, B. van der Klugt, N.J. Adkins, J.W. Bakker, and B.E. Nieuwenhuys. Synchrotron X-ray microtomography of Raney-type nickel catalysts prepared by gas atomisation: Effect of microstructure on catalytic performance. *Catalysis Today*, 163(1):13–19, 2011. Special issue on Industrial Catalysis.
- [193] Jennifer L. Stein, William M. Holden, Amrit Venkatesh, M. Elizabeth Mundy, Aaron J. Rossini, Gerald T. Seidler, and Brandi M. Cossairt. Probing Surface Defects of InP Quantum Dots Using Phosphorus $K\alpha$ and $K\beta$ X-ray Emission Spectroscopy. *Chemistry of Materials*, 30(18):6377–6388, 2018.
- [194] Pablo Castro-Hartmann, Gerard Heck, Jose M. Eltit, Paul Fawcett, and Montserrat Samsó. The ArrayGrid: A methodology for applying multiple samples to a single TEM specimen grid. *Ultramicroscopy*, 135:105–112, 2013.
- [195] Christoph Hofer, Viera Skákalová, Tobias G orlich, Mukesh Tripathi, Andreas Mittelberger, Clemens Mangler, Mohammad Reza Ahmadpour Monazam, Toma Susi, Jani Kotakoski, and Jannik C. Meyer. Direct imaging of light-element impurities in graphene reveal triple-coordinated oxygen. *Nature Communications*, 10(1):4570, 2019.
- [196] Yanyan Zhao, Ke R. Yang, Zechao Wang, Xingxu Yan, Sufeng Cao, Yifan Ye, Qi Dong, Xizi Zhang, James E. Thorne, Lei Jin, Kelly L. Materna, Antonios Trimpalis, Hongye Bai,

- Sirine C. Fakra, Xiaoyan Zhong, Peng Wang, Xiaoqing Pan, Jinghua Guo, Maria Flytzani-Stephanopoulos, Gary W. Brudvig, Victor S. Batista, and Dunwei Wang. Stable iridium dinuclear heterogeneous catalysts supported on metal-oxide substrate for solar water oxidation. *Proceedings of the National Academy of Sciences*, 115(12):2902–2907, 2018.
- [197] Jian Zhu, Shan Pang, Thomas Dittrich, Yuying Gao, Wei Nie, Junyan Cui, Ruotian Chen, Hongyu An, Fengtao Fan, and Can Li. Visualizing the Nano Cocatalyst Aligned Electric Fields on Single Photocatalyst Particles. *Nano Letters*, 17(11):6735–6741, 2017. PMID: 28967261.
- [198] Jieqiong Shan, Yao Zheng, Bingyang Shi, Kenneth Davey, and Shi-Zhang Qiao. Regulating electrocatalysts via surface and interface engineering for acidic water electrooxidation. *ACS Energy Letters*, 4(11):2719–2730, 2019.
- [199] Young Joon Jang, Cynthia Simer, and Taein Ohm. Comparison of zinc oxide nanoparticles and its nano-crystalline particles on the photocatalytic degradation of methylene blue. *Materials Research Bulletin*, 41(1):67–77, 2006.
- [200] Is Fatimah, Shaobin Wang, and Dessy Wulandari. ZnO/montmorillonite for photocatalytic and photochemical degradation of methylene blue. *Applied Clay Science*, 53(4):553–560, 2011.
- [201] Jian-Hui Sun, Shu-Ying Dong, Jing-Lan Feng, Xiao-Jing Yin, and Xiao-Chuan Zhao. Enhanced sunlight photocatalytic performance of Sn-doped ZnO for Methylene Blue degradation. *Journal of Molecular Catalysis A: Chemical*, 335(1):145–150, 2011.
- [202] W.S. Chiu, P.S. Khiew, M. Cloke, D. Isa, T.K. Tan, S. Radiman, R. Abd-Shukor, M.A. Abd. Hamid, N.M. Huang, H.N. Lim, and C.H. Chia. Photocatalytic study of two-dimensional ZnO nanopellets in the decomposition of methylene blue. *Chemical Engineering Journal*, 158(2):345–352, 2010.

- [203] Sungchul Hohng and Taekjip Ha. Single-Molecule Quantum-Dot Fluorescence Resonance Energy Transfer. *ChemPhysChem*, 6(5):956–960, 2005.
- [204] Zheng Hua, Qinfeng Xu, Xiangnan Huang, Chunfeng Zhang, Xiaoyong Wang, and Min Xiao. Energy Transfer from a Single Semiconductor Nanocrystal to Dye Molecules. *ACS Nano*, 8(7):7060–7066, 2014. PMID: 24901293.
- [205] Taekjip Ha and Philip Tinnefeld. Photophysics of Fluorescent Probes for Single-Molecule Biophysics and Super-Resolution Imaging. *Annual Review of Physical Chemistry*, 63(1):595–617, 2012. PMID: 22404588.
- [206] Eitan Lerner, Thorben Cordes, Antonino Ingargiola, Yazan Alhadid, SangYoon Chung, Xavier Michalet, and Shimon Weiss. Toward dynamic structural biology: Two decades of single-molecule Förster resonance energy transfer. *Science*, 359(6373), 2018.

Appendix A

Complete TRPL of ZnO NCs

Figure A.1 shows TRPL decay curves for all ZnO NCs sizes and A555 concentrations. TRPL decay curves for ZnO NCs alone were fit with Equation (2.1) from the main text. Decay curves for mixtures of NCs and A555 were fit with Equation (2.2). Additionally, each NC sample was exposed to high bulk dye concentrations (e.g., >100:1 [A555]:[NC]) to observe energy transfer behavior when every possible surface binding site was occupied (purple data points in the Figure A.1).

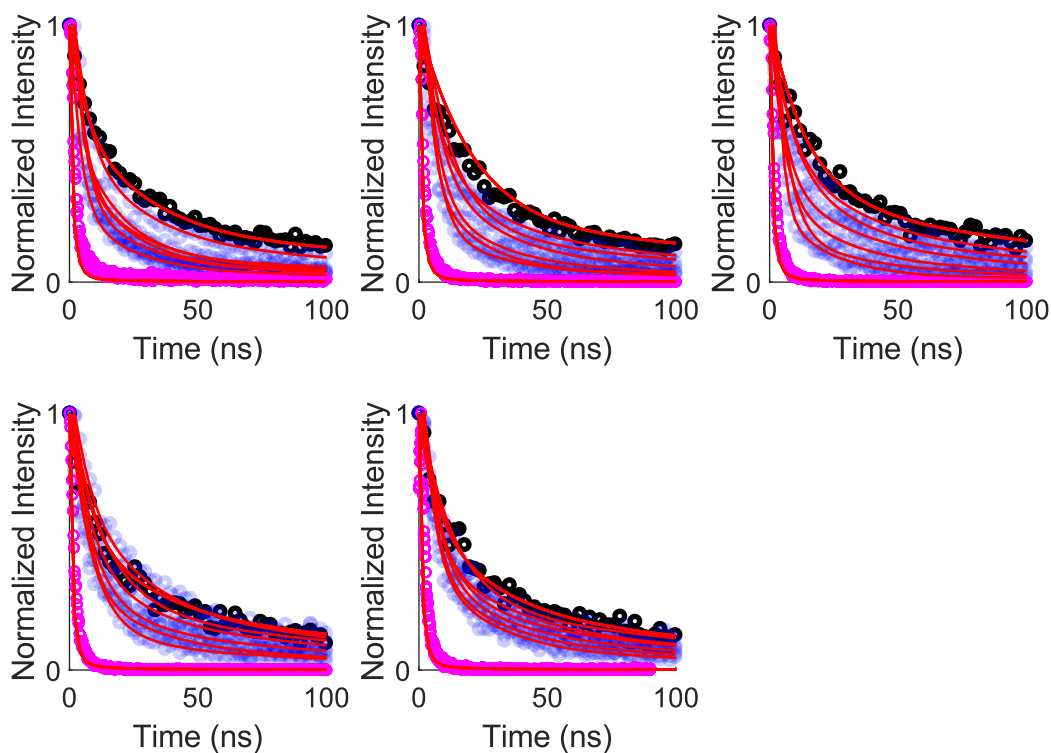


Figure A.1: TRPL decay curves for all ZnO NC sizes and all [A555]. Black data points are the NCs alone, blue points are the mixtures of NCs and A555, magenta points are the decay when the NCs are saturated with A555. Red lines are fits to EQs (1) and (2). a) 2.8 nm diameter NCs b) 4.0 nm c) 4.7 nm d) 5.3 nm e) 5.9 nm.

Appendix B

Division of Work

B.1 Chapter 2

Experiments described in Chapter 2 were designed by Zach Nilsson and Justin Sambur. Ensemble experiments were carried out by Zach Nilsson with assistance from Lacey Beck. Single particle experiments were carried out by Dani Lustig with guidance from Zach Nilsson.

B.2 Chapter 3

Ensemble data analysis was done by Zach Nilsson. Original manuscript was written by Zach Nilsson and Justin Sambur.

B.3 Chapter 4

Original perspective manuscript was written by Zach Nilsson, Michael Van Erdewyk, and Justin Sambur.

B.4 Chapter 5

Single particle data analysis was done by Zach Nilsson. Manuscript is being prepared by Zach Nilsson, Dani Lustig, and Justin Sambur.

LIST OF ABBREVIATIONS

- A555 – Alexa Fluor® 555
- AR – Amplex Red
- EnT – Energy Transfer
- FRET – Förster Resonance Energy Transfer
- ICP-OES – Inductively-Coupled Plasma - Optical Emission Spectroscopy
- ITO – Indium Tin Oxide
- IRF – Instrument Response Function
- NC – Nanocrystal
- OAc – Acetate
- PL – Photoluminescence
- QY – Photoluminescence Quantum Yield
- RG Model – Restricted Geometry model
- ROI – Region Of Interest
- Rz – Resorufin
- SB Model – Stochastic Binding Model
- SMFM – Single Molecule Fluorescence Microscopy
- TEM – Transmission Electron Microscope
- TMAOH – Tetramethyl Ammonium Hydroxide

- TRPL – Time-resolved Photoluminescence